

Universität  
Rostock



Traditio et Innovatio



With the support of the  
Erasmus+ Programme  
of the European Union

# Numerical simulation of ship grounding by taking into consideration external hydrodynamic forces.

submitted on August 01, 2020

by

**UMUNNAKWE Chisom Bernard**

37 Rue du Champ de Manoeuvre

44470 Carquefou

chisombernard@gmail.com

Student ID No.: 219 200 011

## **Supervisor:**

Pr. Hervé Le Sourne

ICAM Nantes

## **First Reviewer:**

Professor Maciej Taczala  
West Pomeranian University

AL. Piastów 41

71-065 Szczecin

Poland

## **Second Reviewer:**

Professor Patrick Kaeding  
University of Rostock

Albert-Einstein-Strasse 2

18059 Rostock

Germany



MASTER THESIS

[This page is intentionally left blank]

---

## DECLARATION OF AUTHORSHIP

I, **UMUNNAKWE Chisom Bernard** declare that this thesis and the work presented in it are my own and have been generated by me as the result of my own original research.

Where I have consulted the published work of others, this is always clearly attributed.

Where I have quoted from the work of others, the source is always given. With the exception of such quotations, this thesis is entirely my own work.

I have acknowledged all main sources of help.

Where the thesis is based on work done by myself jointly with others, I have made clear exactly what was done by others and what I have contributed myself.

This thesis contains no material that has been submitted previously, in whole or in part, for the award of any other academic degree or diploma.

I cede copyright of the thesis in favour of the University of Rostock.

Date: 01/08/2020

Signature: 

[This page is intentionally left blank]

---

## Abstract

The upsurge in marine accidents even with the existence of technological advancements in watch-keeping and navigation have led many researchers, ship owners, shipyards, and maritime organisations out of curiosity to ponder how to minimise the risks posed by these unforeseen events. Nevertheless, despite the recent implementation of double bottom in ship hull structures, the loss of hull integrity still constitute a great threat to the global ship structure during marine accidents. It is an incontrovertible fact that one of the causes for jeopardising ship safety is accidental loading (impact) states such as collision and grounding which places the ship under possible total loss through hold flooding. These events could also lead to loss of lives and environmental pollution in the case of tankers.

In course of this thesis, dynamic impact study was carried out to investigate the sensitivity of strain rate, behaviour laws, failure criteria and nature of impacting body on the structural response and fracture initiation of a stiffened hull panel. It was demonstrated in the considered scenario, that the strain rate was of crucial significance in capturing the dynamic nature of the impact. The influence of failure criteria to the energy absorption capability of the structural member was further illustrated. This impact analysis as a participation to an ISSC benchmark study, showed that the LS-DYNA explicit FE code was capable of predicting structural response of the grillage subject to dynamic state of stress. However, results obtained are not conclusive until the experimental validation is carried out by December, 2020.

Furthermore, after some careful examination on existing literature on ship grounding, it was observed that most researchers assume the ship position as fixed and let the obstruction geometry to impact the ship model. Additionally, focus had been only either on pure raking or pure stranding events and the consideration of the surrounding water had been of negligence. In fact, the grounding chapter of this thesis aimed to illustrate that in the event of ship grounding, the damage extent is highly influenced by the external hydrodynamic forces, velocity of the ship, point of impact and location of the ship centre of gravity.

In continuation, the existence of multiple breaches during ship grounding events due to the consideration of external hydrodynamic forces and the combination of pure raking and pure stranding has been demonstrated. This is in contrast with the continuous breach which is obtained by pure raking alone. This multiple breaches results have shown that it is possible for several compartments of a ship to be damaged during grounding events and this will be of vital significance in quantitative risk analysis. The LS-DYNA explicit nonlinear finite element code was used in conjunction with the MCOL subroutine to account for the surrounding water effect. The results obtained from these analyses will serve as a basis for the validation of an analytical grounding solver based on plastic limit analysis, which is under development in the framework of a H2020 research program named FLARE (**FL**ooding **A**ccident **RE**sponse).

---

# Contents

<b>Abstract</b> . . . . .	<b>iii</b>
<b>List of Figures</b> . . . . .	<b>vii</b>
<b>List of Tables</b> . . . . .	<b>x</b>
<b>1 INTRODUCTION</b> . . . . .	<b>1</b>
1.1 Background and Motivation . . . . .	1
1.2 Objectives and Aims . . . . .	3
1.3 Structure of the Report . . . . .	4
<b>2 SETTING UP AN LS-DYNA MODEL TO SIMULATE AN IMPACT:</b>	
<b>A case Study of the ISSC V.1 Committee Benchmark</b> . . . . .	<b>5</b>
2.1 Background . . . . .	5
2.1.1 Accidental Limit States . . . . .	5
2.1.2 Benchmark Study . . . . .	5
2.1.3 Problem Statement . . . . .	6
2.1.4 Objectives of Benchmark Study . . . . .	6
2.2 Literature Reviews on Failure Models . . . . .	7
2.2.1 Strain based failure criteria . . . . .	8
2.2.2 Triaxial stress state based failure criteria . . . . .	9
2.2.3 Failure criteria based on forming limit diagram (FLD) . . . . .	10
2.2.4 Failure criteria with strain rate influence . . . . .	10
2.3 Material Characterisation . . . . .	12
2.3.1 Provided Experimental Parameters . . . . .	12
2.3.2 Material Model Parameters . . . . .	14
2.3.3 Failure Criteria . . . . .	15
2.4 FEM Modelling and Simulations . . . . .	15
2.4.1 Model Extent . . . . .	15
2.4.2 Finite Element Model Description . . . . .	18
2.5 Smooth indenter results: sensitivity to failure criteria . . . . .	21
2.5.1 MAT24: Piecewise Linear Plasticity sensitivity to failure criteria by neglecting strain rate effect . . . . .	21
2.5.2 MAT24: Piecewise Linear Plasticity sensitivity to failure criteria by considering strain rate effect . . . . .	22
2.5.3 MAT18: Power Law Plasticity sensitivity to failure criteria by ne- glecting strain rate effect . . . . .	23
2.5.4 MAT18: Power Law Plasticity sensitivity to failure criteria by con- sidering strain rate effect . . . . .	24

---

---

2.6	Rough indenter results: sensitivity to failure criteria . . . . .	25
2.6.1	MAT24: Piecewise Linear Plasticity sensitivity to failure criteria by neglecting strain rate effect . . . . .	25
2.6.2	MAT24: Piecewise Linear Plasticity sensitivity to failure criteria by considering strain rate effect . . . . .	27
2.6.3	MAT18: Power Law Plasticity sensitivity to failure criteria by neglecting strain rate effect . . . . .	30
2.6.4	MAT18: Power Law Plasticity sensitivity to failure criteria by considering strain rate effect . . . . .	32
2.7	Further sensitivity analyses on rough indenter results . . . . .	34
2.7.1	Strain Rate Effect . . . . .	34
2.7.2	Different Behaviour Laws . . . . .	36
2.8	Discussion and Conclusion of Benchmark study . . . . .	37
<b>3</b>	<b>SHIP GROUNDING . . . . .</b>	<b>39</b>
3.1	Literature Review on Ship Grounding . . . . .	39
3.1.1	Theoretical Approaches on Ship Grounding . . . . .	40
3.1.2	Numerical Approaches on Ship Grounding . . . . .	41
3.2	Finite Element Model Set-Up . . . . .	42
3.2.1	Material model . . . . .	42
3.2.2	Material failure . . . . .	42
3.2.3	Model extent . . . . .	43
3.2.4	Finite element model description . . . . .	44
3.3	External Dynamics Due to Hydrodynamic Forces . . . . .	47
3.3.1	Explicit Finite Element Analysis . . . . .	47
3.3.2	MCOL Description – Combining Ls-DYNA and MCOL . . . . .	48
3.4	Pure Raking Grounding Simulations . . . . .	52
3.4.1	Case 1: Raking with $V_x = 2\text{m/s}$ . . . . .	53
3.4.2	Case 2: Raking with $V_x = 4\text{m/s}$ . . . . .	56
3.5	Pure Stranding Simulations . . . . .	59
3.5.1	Case 1: full stranding on plate with $V_z = -3.0\text{ m/s}$ . . . . .	60
3.5.2	Case 2: medium stranding on plate with $V_z = -1.5\text{ m/s}$ . . . . .	62
3.5.3	Case 3: stranding on girder with $V_z = -2.0\text{ m/s}$ . . . . .	65
3.5.4	Case 4: stranding on floor-girder intersection with $V_z = -1.5\text{ m/s}$ . . . . .	67
3.6	Simulations Combining Raking and Stranding – Multiple Breaches Analyses . . . . .	70
3.6.1	Case 1: Ship_1 multiple breaches simulation . . . . .	71
3.6.2	Case 2: Floodstand multiple breaches simulation . . . . .	74
3.6.3	Damage comparisons . . . . .	77
3.7	Parametric Sensitivity Analyses . . . . .	78

---

---

3.7.1	Damage sensitivity analysis to pitch movements . . . . .	78
3.7.2	Damage sensitivity to roll movements . . . . .	81
<b>4</b>	<b>CONCLUSION . . . . .</b>	<b>83</b>
<b>5</b>	<b>FURTHER WORK(S) . . . . .</b>	<b>84</b>
<b>6</b>	<b>ACKNOWLEDGEMENTS . . . . .</b>	<b>85</b>
	<b>References . . . . .</b>	<b>87</b>
<b>A</b>	<b>Floodstand with <math>V_x= 4\text{m/s}</math>, <math>V_z= -1.0 \text{ m/s}</math> . . . . .</b>	<b>91</b>

---

## List of Figures

1	Distribution of casualty events with a ship (From: EMSA, 2018). . . . .	1
2	Costa Concordia grounding event (From: Copernicus Marine Service, 2013)	2
3	Newly Upgraded Large Double-pendulum Apparatus (From: Quinton, 2020)	7
4	Description of the characteristic element length . . . . .	9
5	Algorithm for determining the dynamic failure strain. (From: Paik et al, 2017) . . . . .	12
6	Stress-strain curves obtained from experiment. . . . .	12
7	Flow curve to be used in order to account for strain rate. . . . .	14
8	Illustration of assumptions for reproducing idealised model . . . . .	16
9	Idealised model for FEA . . . . .	17
10	Smooth Indenter: a). Actual indenter b). Idealised model . . . . .	17
11	Modelled Rough Indenter . . . . .	18
12	Simulation Set Up . . . . .	19
13	Sensitivity of the EPS, RTCL and Paik failure criteria to the mesh size. . .	20
14	Force and Energy Plots for MAT 24 with different failure criteria . . . . .	21
15	Grillage deflection and location of overstrained elements . . . . .	21
16	Force and Energy Plots for MAT 24 using different failure criteria . . . . .	22
17	Grillage deflection and location of overstrained elements for power law . . .	23
18	Force and Internal Energy Plots for Power Law using different failure criteria	23
19	Force and Internal Energy Plots for Power Law using different failure criteria	24
20	Energy balance for the rough indenter using Peshmann & Kulzep failure criteria . . . . .	25
21	Force and Energy Plots for Piecewise Plasticity using different failure criteria	26
22	Grillage deflection and location of highly strained elements/fracture: a) Peshmann, b) Paik et al, c) RTCL . . . . .	26
23	Force Plots for Piecewise Linear Plasticity using different failure criteria . .	27
24	Grillage deflection and stages of fracture for RTCL damage criteria . . . .	28
25	Grillage deflection and location of highly strained element/fracture for Cowper-Symond strain rate effect: a) Peshmann, b) Paik et al, c) RTCL . .	28
26	Energy plots for Piecewise plasticity for different failure criteria . . . . .	29
27	Force Plots for Power law plasticity for different failure criteria . . . . .	30
28	Grillage location of fracture for power law without strain rate effect: a) Peshmann, b) Paik et al, c) RTCL . . . . .	30
29	Energy plots for Power law plasticity for different failure criteria . . . . .	31
30	Energy balance for RTCL failure criteria with rough indenter . . . . .	31
31	Force Plots for Power law plasticity for different failure criteria . . . . .	32

32	Grillage location of highly strained elements/fracture for power law with strain rate effect: a) Peshmann, b) Paik et al, c) RTCL . . . . .	32
33	Energy plots for Power law plasticity for different failure criteria . . . . .	33
34	Force plots for different different failure criteria showing strain rate sensitivity	34
35	Energy plots for different different failure criteria showing strain rate sensitivity	35
36	Internal Energy plots for MAT24: Piecewise Plasticity and MAT18: Power Law . . . . .	36
37	Internal Energy plots for MAT24: Piecewise Plasticity and MAT18: Power Law . . . . .	36
38	Different seabed topologies: (a) rock, (b) reef (c) shoal (From: Alsos, 2007).	39
39	Idealised geometry of the double bottom for grounding analysis . . . . .	43
40	Seabed rock geometry . . . . .	44
41	Meshed double bottom . . . . .	46
42	Example of structural crashworthiness with or without self-contact phenomenon in terms of deformed shape. From . . . . .	46
43	Comparison of LS-DYNA/MCOL simulation with real ship. (From: Le Sourne et al., 2003) . . . . .	49
44	Body-fixed and earth-fixed frames of references. From . . . . .	50
45	Coupling card for LS-DYNA/MCOL simulation . . . . .	50
46	PART_INERTIA card for MCOL rigid body . . . . .	51
47	Set-up for pure raking simulations . . . . .	52
48	Time evolution of energies and force plots for Raking (2 m/s) grounding simulation . . . . .	53
49	Failure modes of the double bottom structure for raking (2m/s) grounding simulation . . . . .	54
50	Internal Energy and force plots versus x-displacement for Raking (2 m/s) grounding simulation . . . . .	55
51	Time evolution of energies and force plots for Raking (4 m/s) grounding simulation . . . . .	56
52	Failure modes of the double bottom structure for raking (4m/s) grounding simulation . . . . .	57
53	Internal Energy and force versus displacement plots for Raking (4 m/s) grounding simulation . . . . .	57
54	Set-up for pure stranding simulation with impact points . . . . .	59
55	Energy and force plots vs. time for full stranding (-3 m/s) grounding simulation . . . . .	60
56	Deformation/Failure modes of structural members during full stranding . .	61
57	Internal Energy and force plots versus z displacement for full stranding (-3 m/s) grounding simulation . . . . .	62

---

58	Energy and force plots versus time for medium stranding (-1.5 m/s) grounding simulation . . . . .	63
59	Deformation/Failure modes of structural members during medium stranding	64
60	Internal Energy and force plots versus z-displacement for medium stranding grounding simulation . . . . .	64
61	Energy and force plots vs. time for stranding on girder ( $V_z = -2$ m/s) simulation . . . . .	65
62	Deformation/Failure modes of structural members during stranding on girder	66
63	Internal Energy and force plots versus z-displacement for stranding on girder simulation . . . . .	66
64	Energy and force plots versus time for stranding on girder ( $V_z = -1.5$ m/s) simulation . . . . .	67
65	Deformation/Failure modes of structural members during intersection stranding . . . . .	68
66	Internal Energy and force plots versus z-displacement for stranding on intersection simulation . . . . .	69
67	Set-up for multiple breaches simulation with impact points . . . . .	70
68	Energy and force plots versus time for Ship_1 breaching simulation . . . . .	71
69	Deformation/failure modes for Ship_1 multiple breaches simulation . . . . .	72
70	Internal Energy and force plots vs. x-displacement for Ship_1 breaching simulation . . . . .	73
71	Energy and force plots versus time for Floodstand breaching simulation . . . . .	74
72	Deformation/failure modes for Floodstand multiple breaches simulation . . . . .	75
73	Internal Energy and force plots for Floodstand breaching simulation . . . . .	76
74	Comparison of pitch angles vs. time for fore-ship and mid-ship grounding . . . . .	79
75	Internal Energy and force plots for sensitivity of pitch consideration to damage	79
76	Failure of structural members during multiple breaching - roll sensitivity . . . . .	81
77	Comparison of roll angles vs. time for “centred-impact” and “offset-impact” grounding . . . . .	82

---

---

## List of Tables

1	Material Properties . . . . .	12
2	Carriage Parameters . . . . .	13
3	Indenter Dimensions . . . . .	13
4	Actual Stiffened Hull Panel (Grillage) Dimensions . . . . .	13
5	Idealised Stiffened Hull Panel (Grillage) Dimensions . . . . .	16
6	Failure criteria data for simulations: mesh size = 10mm . . . . .	20
7	Material model properties . . . . .	42
8	Material effective plastic strain values for ship structural members . . . . .	43
9	Dimensions of double bottom structural members . . . . .	44
10	Ships to be considered for LS-DYNA/MCOL grounding simulations . . . . .	51
11	Pure raking comparison . . . . .	58
12	Pure raking Internal energy comparison . . . . .	58
13	Pure stranding comparison . . . . .	69
14	Pure stranding Internal energy comparison . . . . .	69
15	Damage Comparison between pure raking and multiple breaches simulation	77
16	Damage comparison between fore-ship and mid-ship grounding: multiple breaches simulation . . . . .	80
17	Damage Comparison between “centred impact” and “offset impact” multiple breaches simulation for Ship_1 . . . . .	82

---

[This page is intentionally left blank]

# 1. INTRODUCTION

## 1.1. Background and Motivation

Over the years, there has been an increase in the demand for ship safety, ranging from the safety of people to environmental protection. Statutory rules and regulations have been put in place to quantify, minimise the risk, and therefore increase safety. It is without doubt that one of the causes for endangering ship safety is accidental loading states: collision and grounding. These accidents create scenarios for ship loss by: motion impact shell failure leading to water ingress/cargo spill, hold flooding, transverse/longitudinal bulkhead failure, progressive flooding of adjacent holds, which possibly causes loss of reserve buoyancy and finally loss of vessel.

The casualty of these accidental scenarios may vary depending on the point of impact, sea state, hull form, speed of impact, type of ship, shape of striking body, and to mention but a few. From figure 1, it is obvious that grounding/stranding contribute majorly to casualty events of ships. Also it has been found that fatalities mainly occurred during a flooding/foundering (35.2%), and (53.3%) of the injuries took place during navigational events (contact, collision and grounding/stranding) (EMSA, 2018).

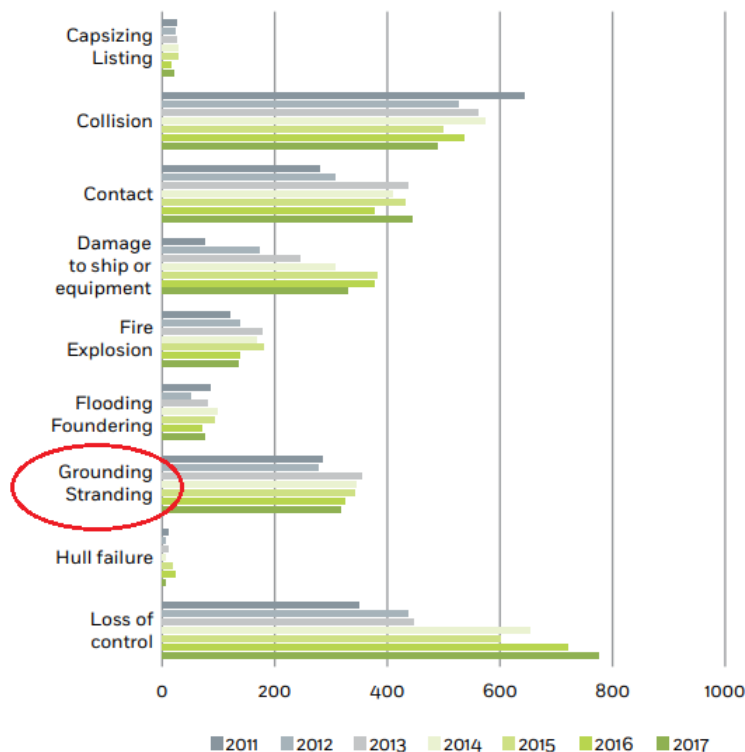


**Figure 1:** Distribution of casualty events with a ship (From: EMSA, 2018).

In 13 January 2012, *Costa Concordia* an Italian cruise ship ran aground and overturned after striking a rock formation which tore open along three compartments on the aft-part

of the ship resulting to flooding, death of 32 persons, 17 injured persons, and ship loss.



(a) Before the Incident



(b) After the Incident

**Figure 2:** Costa Concordia grounding event (From: Copernicus Marine Service, 2013)

This shows that despite the numerous efforts in order to minimise the chances of such incidents, and the increase in technological advancement in the areas of navigation and watch-keeping, there still exist growths in these dreaded events. From figure 1 we can see that grounding events contribute consistently to serious marine accidents.

Moreover, despite the recent implementation of double bottom in ship hull structures, the loss of hull integrity is still something that continue to occur in the events of grounding. From a statistical data from Allianz (2019) which indicated that ship grounding is at the second place on the top ten causes of ship loss, the idea of making ships crashworthy to tolerate impact loads, to have an increased capability to absorb kinetic energy before breaching have stirred up a wide research interest lately (Alan et al, 2009).

Many researches and experiments in the areas of evaluating the crashworthiness of ships have been in place. Over the past decades, numerical analyses have been in use as alternative for structural analyses, but this topic has been very challenging in terms of high computational, processing and memory costs due to the increase in ship size and structural complexity. Also, results from numerical analyses require experimental validations.

Motivated by this context, the project **FLARE** (**FL**ooding **A**ccident **RE**sponse) which involves the cooperation between passenger ship owners, shipyards, classification societies and research institute partners, aims to calculate collision and grounding structural damage as part of quantitative risk analysis to account for the chances of evacuation of passengers before total ship loss in case of such events.

This Master Thesis was performed under the supervision of Professor Hervé Le Sourne (ICAM) in the framework of the project FLARE and the academic final dissertation of the ERASMUS MUNDUS program EMSHIP (9<sup>th</sup> Cohort M120). During this project, the academic research was carried out at the ICAM Nantes campus.

## 1.2. Objectives and Aims

The main objectives for this thesis are as follows:

- To clearly understand the impact response of a metallic structure up to plastic deformation and rupture by setting up an LS-DYNA model. This first work will be conducted through the participation to a benchmark study organised by the International Ship and Offshore Structures Congress (ISSC) - Accidental Limit States Committee. The study investigates the structural response and fracture analysis of a stiffened hull panel (called grillage) which is subject to a dynamic impact by two different kinds of indenters : smooth and non-smooth. The aim is to develop an idealised model of the grillage and use the nonlinear FEM code: LS-DYNA to investigate the structural impact.
- To perform ship grounding simulations by taking into account external hydrodynamic forces. These numerical simulation results will serve as a validating tool for the FLARE analytical solver, which is based on plastic limit analysis. Although FEA has been in use for grounding analyses, most literature assumed the ship model to be fixed in a position and allowed the rock to crush the double bottom. In reality the ship is free to move during and even after impact and her movement is mainly governed by external hydrodynamic forces.

Also, the consideration of the surrounding water is normally neglected by most researchers, but the surrounding water can be very important in grounding analyses in terms of added mass, buoyancy effect, and to mention but a few which also contribute to the loss of kinetic energy. This is the reason why MCOL subroutine has been developed and integrated into LS-DYNA in order to take into consideration external hydrodynamic effects. Multiple breaches analyses will also be investigated by taking into consideration both surge and heave velocities of the ship.

Generally, FEA requires vast amount of work and time to set up a model due to the expertise needed to use such kinds of FE software, and high computational and storage cost associated to the fine FE meshes required.

Hence, because of these limitations of the FE software, the FLARE super-element solver will be a complementary tool used at the pre-design stage to perform risk analyses in order to define the most damaging scenarios before carrying out FEA. Therefore, the aim of the present work is to develop numerical models of a passenger ship bottom, and use the LS-DYNA explicit nonlinear FE code coupled with MCOL, thus providing the basis for result validation of the FLARE software. The analytical solver will then be improved in order to better model the ship bottom failure, with a focus on breach size calculation. Validation of the implemented analytical solutions will be done by comparison with FE simulations.

---

### 1.3. Structure of the Report

This report is divided as follows;

- **Chapter 2** shows how a LS-DYNA model was setup to model impact and extended to an ISSC benchmark study. Taking into account material characterisation, and sensitivity analyses to different parameters like failure criteria, strain rate effect, and behaviour laws.
  - **Chapter 3** dives into ship grounding by describing the model characteristics, external dynamics, parametric sensitivity analyses and several grounding scenarios.
  - **Chapter 4** gives a conclusion of the work, and recommendations for further developments are presented.
  - **Chapter 5** gives future works and perspectives.
-

## 2. SETTING UP AN LS-DYNA MODEL TO SIMULATE AN IMPACT: A case Study of the ISSC V.1 Committee Benchmark

### 2.1. Background

According to ISSC (2018), The International Ship and Offshore Structures Congress (ISSC) is a forum for the exchange of information by experts undertaking and applying marine structural research.

The specific objectives of the ISSC are:

- to review research in progress and to facilitate the evaluation
- to disseminate the results from recent investigations
- to identify areas requiring future research, and
- to suggest improvements in design, production and operations procedures

Also, the structures of interest to ISSC include ships, offshore structures and other marine structures used for transportation, exploration, and exploitation of resources in and under the oceans (ISSC, 2018).

There are several specialist committees in the ISSC: Accidental Limit States, Experimental Methods, Material and Fabrication Technology, Offshore Renewable Energy, Special Craft, Arctic Technology, Structural Longevity and Sub-sea Technology. All these committees carry out research works in their various fields in order to exchange latest information and to meet the specific aims and objectives of the ISSC. In the scope of this work, focus is on the Accidental Limit State.

#### 2.1.1. Accidental Limit States

The mandate of this committee is for accidental limit states (ALS) of ships and offshore structures and their structural components under accidental conditions. Also, the types of accidents considered are collision, grounding, dropped objects, explosion, and fire (ISSC, 2003).

#### 2.1.2. Benchmark Study

This benchmark study examines the structural response and fracture analysis of a stiffened hull panel called the grillage which is subject to an energy-limited medium-speed impact with two types of rigid indenters: smooth, and non-smooth.

The smooth indenter is a thick spherical cap of a sphere, while the non-smooth rigid indenter consists of a spherical cap transition into a tetrahedron like shape and solid shine.

---

The spherical cap induces the bi-axial tension, while the solid chine induces a combine state of tension and shear. Laboratory experiments of these indentations will serve as the basis for the benchmark study.

### 2.1.3. Problem Statement

Several recent studies have compared the results of fully numerical FEA simulations of stiffened plate hull structures with similar laboratory experiments. In most of these experiments, the stiffened hull structure was loaded up to fracture by a smooth spherical indenter using a hydraulic actuator. This tends to induce a state of stress of primarily quasi-static bi-axial tension (Quinton, 2020).

Irrespective of these successes with simulations and experiments, there exists some limitations with this approach:

- Fracture / failure strain has been known to be dependent on the state of stress at fracture.
- Ship hull impacts may not always be quasi-static
- In reality, the impacting body will not always be a smooth sphere, but instead may have other shapes, thereby inducing localised stress states, which is a considerable factor in fracture creation.
- Also, even with a smooth spherical indenter, any form of sliding or tearing of the indenter will induce a dynamic state of stress.

### 2.1.4. Objectives of Benchmark Study

The major objectives of this study are listed below:

- To understand the physical phenomenon behind the impact resistance of a ship structure.
- To check whether numerical technologies are capable of appropriately predicting hull damage and fracture due to time-varying states of stress; or whether the development of new technologies are required.

In order to accomplish these objective, two controlled stiffened hull laboratory impact experiments using a large “limited-energy” double-pendulum impact apparatus will be carried out: Impact of a stiffened panel with a rigid spherical indenter, and with a rigid non-smooth indenter.

The experiments will be carried out at Memorial University of Newfoundland using a newly upgraded large double-pendulum apparatus. The purpose of this new design was to install an extremely stiff pendulum carriage, which provides the fixed boundary condition for the stiffened hull panel. The figure 3 shows the double pendulum set up.

---

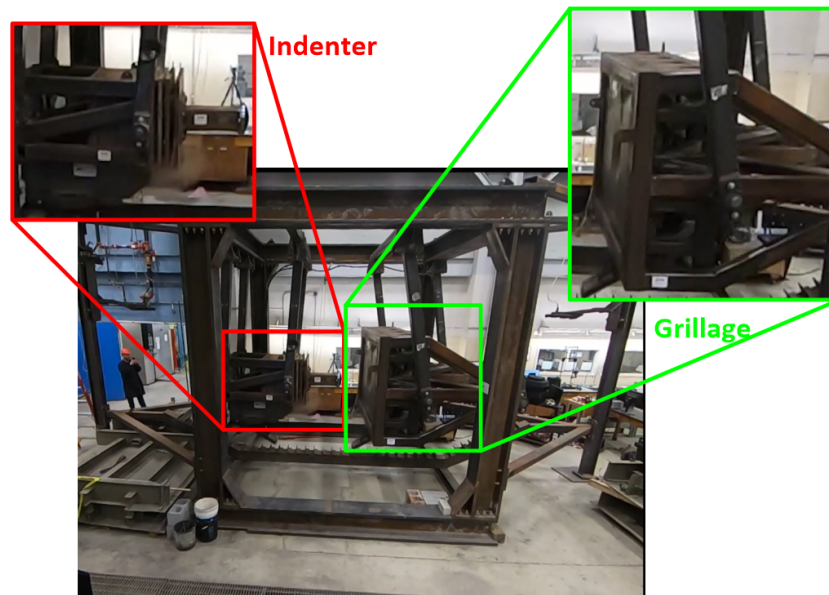


**Figure 3:** Newly Upgraded Large Double-pendulum Apparatus (From: Quinton, 2020)

Two different sets of numerical simulations will be executed: smooth indenter and non-smooth indenter. A direct benchmarking will be done by comparing numerical simulation results with the laboratory results. This will enable the committee to determine if the existing numerical technologies are sufficient to predict the structural responses and fracture of stiffened hull panels subject to time-varying states of stress (dynamic state).

## 2.2. Literature Reviews on Failure Models

In the studies of ship crashworthiness, the major questions that arise are: how to model fracture, and to which threshold value of failure strain should be used in the model set up. It is without doubt that for a successful and rational numerical simulation, the numerical model should be adequately set up to capture correctly the fracture.

In LS-DYNA, rupture is modelled by removing over-strained elements once the effective plastic strain calculated at all integration points exceeds a given threshold value. This threshold value must be inputted manually in the material card in order to account for failure. The definition of a unique failure strain makes the solution very sensitive to the mesh because of the so-called stress localisation.

The accurate modelling of fracture is an essential part in impact studies, and it is still an ongoing study. According to Ehlers (2008): One major problem with finite element method is the sensitivity to mesh sizes close to fracture on zones with large strain gradients. Shell elements are especially sensitive to this effect due to plane stress formulation.

As mesh density, element shape and mesh size show significance in the modelling of fracture. Several authors have formulated failure models and they all have their uses and applications.

---

Calle et al, (2015) divided the failure criteria into the following:

- Strain based failure criteria
- Triaxial stress state based failure criteria
- Failure criteria based on forming limit diagram
- Failure criteria with strain rate influence

### 2.2.1. Strain based failure criteria

This criteria uses the effective plastic strain value. The critical effective plastic strain is the criterion used to predict the onset on fracture. The rupture strain of the material is normally obtained from uniaxial tensile tests. But, the measurement of the rupture strain depends on the gauge length of the specimen. For instance if the specimen is large, lower values for the fracture strain are expected, the reverse is the case for shorter test specimens which are due to the local elongation of the specimen near failure.

**Barba**, (1880) tried to prove this non-uniform strain distribution in specimens by creating the Barba's law as described in equation 1

$$e_f = e_u + c \frac{\sqrt{WT}}{L} \quad (1)$$

The equation states that the failure strains obtained from uniaxial tests can be expressed as a function of the gauge length in an asymptotic relation (equation 1). Where  $e_f$  is the engineering strain at rupture,  $e_u$  is the uniform engineering strain,  $c$  is the Barba constant,  $L$  is the gauge length (or the equivalent element size in a finite element modelling),  $W$  and  $T$  are the width and the thickness of the tensile test specimen respectively. The first term in equation 1 represents the uniform strain along the specimen length and the second component represents the localised strain due to necking.

**Peschmann and Kulzep**, (2000) similar to Barba's law divided the plastic strain into uniform and localised strains according to:

$$\varepsilon_f = \varepsilon_g + \varepsilon_m (x_e/T) (T/l_e) \quad (2)$$

where  $\varepsilon_f$  is the breaking strain,  $T$  and  $l_e$  are the plate thickness and the finite element length respectively,  $\varepsilon_g$  is the uniform strain of the specimen,  $\varepsilon_m$  is the strain in the highly deformed necking region, and  $x_e$  is the length of the necking.

**Ehlers et al** (2008) proposed the failure strain formulation as:

$$\varepsilon_f = \varepsilon_g + \alpha (T/l_e) \quad (3)$$

where  $\alpha = \varepsilon_m (x_e/T)$  and the parameters  $\varepsilon_g$  and  $\alpha$  are obtained from experiments. The use of  $l_e/T$  ratios greater than 5 for shell elements is recommended for numerical analyses.

---

**Germanischer Lloyd AG** initially proposed the through thickness strain criterion which is based on the experimental measurement in actual ship structures (Vredevelt and Feenstra, 2001). It is expressed as:

$$\varepsilon_f = \varepsilon_g + \varepsilon_m (T/l_e) \quad (4)$$

This formulation is similar to the one of Peschmann and Kulzep. Based on experimental observation, Peschmann and Lehmann proposed that when considering shell elements for ship building steels,  $\varepsilon_g = 0.056$  and  $\varepsilon_m = 0.54$ . Therefore, the failure strain becomes:

$$\varepsilon_f = 0.056 + 0.54 \frac{t}{l_e} \quad (5)$$

where  $t$  is the plate thickness, and  $l_e$  is the characteristics element length which is the element diagonal length as shown in figure 4. Where  $x_1$  and  $x_2$  are the mesh element dimensions. For a squared element, the characteristic element length becomes  $l_e = x\sqrt{2}$ .

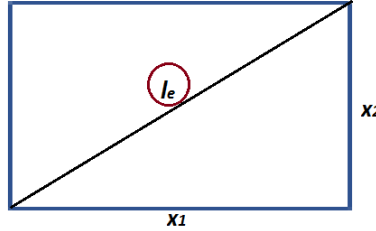


**Figure 4:** Description of the characteristic element length

### 2.2.2. Triaxial stress state based failure criteria

This failure criteria points out that the equivalent strain based failure approach is not always accurate because of the stress state of the specimen during the uniaxial tensile tests. For instance, the biaxiality of the loading or pure shear of the loading. Several researchers have suggested that the failure of a material also depends on the triaxial state of stress.

**Lehmann and Yu** (1998) suggested a failure criterion which takes into account the triaxiality of the stress state based on the continuum damage mechanics.

$$I_R = \varepsilon_v \left[ \frac{2}{3}(1 + \nu) + 3(1 - 2\nu) \left( \frac{\sigma_m}{\bar{\sigma}} \right)^2 \right]^{(2n+1)} \quad (6)$$

The  $I_R$  is the critical damage parameter (rupture index) which governs material damage evolution until the rupture (Servis and Samuelides, 2006). This index is evaluated at each element of the numerical model until failure occurs ( $I_R \geq \epsilon_f$ ), where  $\epsilon_f$  is the rupture strain obtained from uniaxial tensile test.  $\nu$  is the Poisson coefficient to include the influence of multiaxial state of stress and strain on the effective strain  $\epsilon_v$ ,  $n$  is the strain hardening exponent,  $\sigma_m$  is the mean stress, and  $\bar{\sigma}$  is the equivalent stress.

---

**Törnqvist** (2003) combined two failure models: the Rice - Tracey and the Cockcroft-Latham Criteria. Törnqvist developed the RTCL criterion in order to take into account the triaxialities of stress state. The criterion is expressed as:

$$D = \int_0^{\bar{\epsilon}^f} f \left( \frac{\sigma_m}{\bar{\sigma}} \right)_{RTCL} d\bar{\epsilon} \quad (7)$$

where  $D$  is the integral function of damage,  $\sigma_m$  is the mean stress,  $\bar{\sigma}$  is the equivalent stress and  $d\bar{\epsilon}$  is the effective plastic strain increment. The solution of the integral function of damage is furthermore given as:

$$D_{cr} = n + (\varepsilon_n - n) T/l_e \quad (8)$$

where  $n$  is the power law exponent,  $\varepsilon_n$  is the fracture strain obtained from uniaxial tensile test,  $T$  is the thickness of the plate,  $l_e$  is the characteristic element length.

### 2.2.3. Failure criteria based on forming limit diagram (FLD)

These failure criteria are widely used to predict the onset of local necking by plotting the plastic instability points of plate materials (principle strains) considering proportional strain paths.

**Alsos** (2008) developed the stress based FLD criterion also known as the BWH criterion by combining the shear stress criterion of Bressan and Williams (1993) with the local necking criterion of Hill (1952).

**Abubakar and Dow** (2013) predicted the maximum deformation the material can withstand prior to necking after predicting the maximum deformation just before the onset of necking by adopting the FLD. This FLD failure criterion has been successfully compared with experimental results using the RTCL and the BWH failure criteria which take into consideration stress states.

### 2.2.4. Failure criteria with strain rate influence

Some formulations have been proposed in order to take into account the strain rate effects on the strain hardening of materials. **Cowper and Symonds** (1957) takes into consideration the strain rate sensitivity of a material in FE modelling. In order to determine the dynamic yield strength with the known static yield strength, Jones (2012), proposed:

$$\sigma_{Yd} = \left[ 1 + \left( \frac{\dot{\epsilon}}{C} \right)^{1/q} \right] \sigma_Y \quad (9)$$

where  $\sigma_Y$  is the static yield strength,  $\sigma_{Yd}$  is the dynamic yield strength,  $C$  and  $q$  are the Cowper-Symonds coefficients, and  $\dot{\epsilon}$  is the strain rate which is implicitly defined in the NLFEA depending on the impact speed, among other factors.

---

According to Paik et al (2017), the inverse of the Cowper-Symonds equation as a function of the strain rate can be used to define the dynamic fracture strain given as follows:

$$\varepsilon_{fd} = \left[ 1 + \left( \frac{\dot{\varepsilon}}{C} \right)^{1/q} \right]^{-1} \varepsilon_f \quad (10)$$

where  $\varepsilon_f$  is the static fracture strain, and  $\varepsilon_{fd}$  is the dynamic fracture strain. Paik et al proposed an analytical method for calculating the strain rate when the collision speed is known. For impact speed  $V$  in  $m/s$ , the expression is given as:

$$\dot{\varepsilon} = 2.97V - 0.686 \quad (11)$$

**Paik et al** (2017) suggested the following algorithm for obtaining the dynamic failure strain as shown in figure 5.

From figure 5, the static rupture strain  $\varepsilon_f$  is obtained from tensile test result, Hughes and Paik (2013) proposed an expression for the critical fracture strain  $\varepsilon_{fc}$  as:

$$\varepsilon_{fc} = \gamma_1 \gamma_2 \varepsilon_f \quad (12)$$

$\gamma_1$  is a factor which accounts for finite element size, and it is obtained from:

$$\gamma_1 = d_1 \left( \frac{t}{s} \right)^{d_2} \quad (13)$$

$t$  is the plate thickness,  $s$  is the element size,  $d_1$  and  $d_2$  are coefficients and can be taken as 4.1 and 0.58 respectively for carbon steels.  $\gamma_2$  is a correction factor associated with localised bending due to folding and can be taken within the range of 0.3-0.4. If  $\gamma_1$  is smaller than 1.0,  $\gamma_1$  is taken as 1.0.  $C$  and  $q$  are the Cowper-Symonds parameters to account for strain rate effects and they are normally taken as 40.4 and 5 for mild steel, and 3200 and 5 for high tensile steel respectively (Paik et al, 2017).

This method has been successfully validated by Liu et al (2016) by a comparison with experimental data. It was found out that the criterion is suited for both very large sized and small sized structures.

---

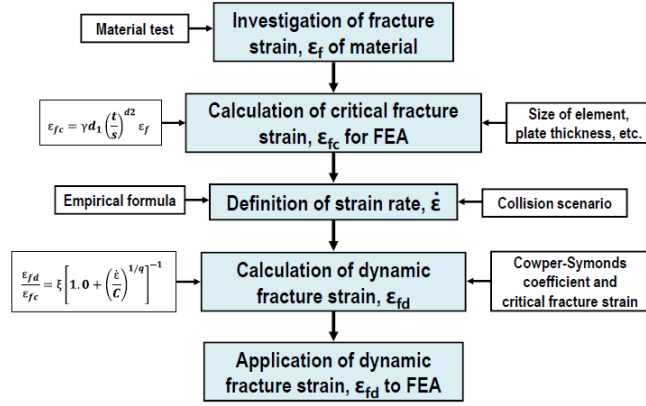


**Figure 5:** Algorithm for determining the dynamic failure strain. (From: Paik et al, 2017)

## 2.3. Material Characterisation

### 2.3.1. Provided Experimental Parameters

For the stiffened hull panel, the material used was steel grade CSA G40.21 44W with standard requirements of: minimum yield strength of 300 MPa, Tensile strength of 450 to 585 MPa, and minimum elongation of 20 to 23%.

Tensile test results shown in figure 6 for this grade of steel depicting stress-strain curves using the dog-bone specimen yielded material properties to be used for numerical simulation as shown in table 1.

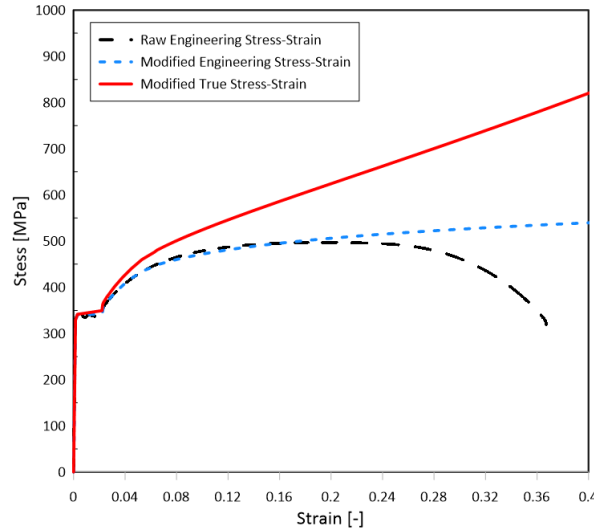


**Figure 6:** Stress-strain curves obtained from experiment.

**Table 1:** Material Properties

Material	$\sigma_Y$ (MPa)	$\sigma_t$ (MPa)	$K$ (MPa)	$n$ (-)	$\varepsilon_f$ (-)	$E$ (GPa)
CSA G40.21 44W	328	497	586	0.085	0.367	221

From table 1,  $\sigma_Y$  is the yield stress from observation,  $\sigma_t$  is the ultimate stress or tensile strength of the material,  $K$  is the strain hardening constant,  $n$  is the strain hardening exponent obtained by curve fitting,  $\varepsilon_f$  is the failure strain of the material during the test, and  $E$  is the Young's modulus of elasticity.

The carriage parameters for easy modelling of impact were also provided. Figure 3 above gives a representation of the carriage setup. The table 2 below gives the parameters for one carriage. Where  $M$  is the total mass of the carriage,  $V$  is the impact speed,  $KE_{max}$  is the total kinetic energy.

**Table 2:** Carriage Parameters

M (kg)	V (m/s)	$KE_{max}$ (J)
4500	4.429	44145

Furthermore, the dimensions for the smooth indenter were also made available for easy modelling (table 3 and figure 10). It is worth knowing that the indenters are made of hardened steel and may be considered to not have undergone plastic deformation during the impact.

**Table 3:** Indenter Dimensions

$r_c$ (m)	$r_h$ (m)	$D_{cyl}$ (m)	$h_{cyl}$ (m)
0.254	0.0508	0.3048	0.0254

Where  $r_c$  is the spherical cap radius,  $r_h$  is the spherical cap height,  $D_{cyl}$  is the cylinder diameter,  $h_{cyl}$  is the cylinder height.

The non-smooth indenter was described as a modified version of the smooth spherical cap indenter, as the top part retains the spherical geometry, while the remaining part has been cut to provide the discontinuous changes of curvature. It is best described by a diagram shown in figure 11.

The dimensions for the actual stiffened panel is given in the table 4 below.

**Table 4:** Actual Stiffened Hull Panel (Grillage) Dimensions

Grillage Parts	Length (m)	Breadth (m)	Thickness (mm)
Plate	2.032	1.36	7.9
Stiffener Web	1.2838	0.17	7.9
Stiffener Flange	1.2838	0.1016	7.9
Stiffener Spacing	0.60945		

---

### 2.3.2. Material Model Parameters

For this study, two behaviour laws or material models will be utilised using the LS-DYNA explicit FE code, in order to investigate the strain rate influence with the different material models. The behaviour laws are described as follows;

- MAT24 – PIECEWISE LINEAR PLASTICTY

This is an elasto-plastic material type where an arbitrary stress-strain curve and arbitrary strain rate dependency can be defined. For the consideration of strain rate effects, two options were made available in LS-DYNA:

a). The use of the Cowper-Symonds model with the strain rate parameters  $C$  and  $P$  of which the initial yield stress is scaled. In this study the parameters  $C$  and  $P$  were taken as 3200 and 5 respectively.

b). The use of Load curve defining effective stress versus effective plastic strain (flow curve). In this study the flow curve used was extracted from the modified true stress-strain curve provided from the experiment.

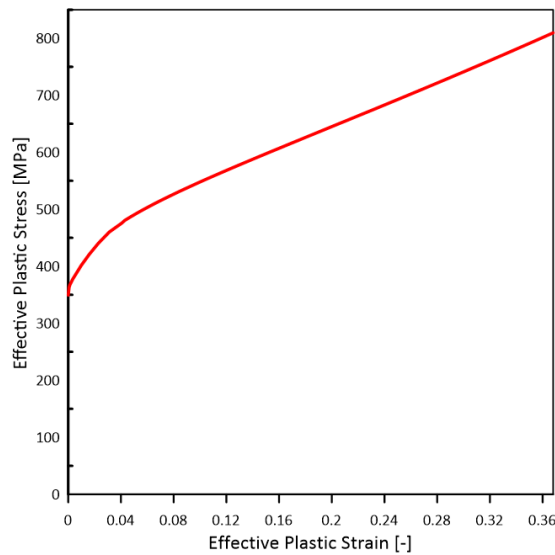


**Figure 7:** Flow curve to be used in order to account for strain rate.

- MAT18 – POWER LAW PLASTICITY

This is an elasto-plastic with isotropic hardening model which rate effect utilises the power law hardening principle. The yield stress  $\sigma_y$  as a function of plastic strain obeys the equation:

$$\sigma_y = k\varepsilon^n = k(\varepsilon_{yp} + \bar{\varepsilon}^p)^n \quad (14)$$

where  $\varepsilon_{yp}$  is the elastic strain to yield and  $\bar{\varepsilon}^p$  is the logarithmic effective plastic strain (LS-DYNA, 2018). Using the power law material model, inputs to the card requires the strength coefficient  $K$ , and hardening exponent  $n$ . These parameters

---

were obtained by curve fitting and made available during the experiment as shown in table 1.

To account for strain rate, the Cowper–Symonds model with the parameter  $C$  and  $P$  were inserted which scales the yield stress with the factor.

$$1 + \left(\frac{\dot{\varepsilon}}{C}\right)^{1/p} \quad (15)$$

### 2.3.3. Failure Criteria

Three different failure criteria will be investigated in this study, they are as follows:

- Strain based failure criteria as described in section 2.2.1 in equation 5 which was proposed by Peschmann and Kulzep.

$$\varepsilon_f = 0.056 + 0.54 \frac{t}{l_e}$$

- A consideration on stress state based failure as described in section 2.2.2 in equation 8 which is the RTCL criterion, and also follows the Swift instability (Swift, 1952 ) criterion.

$$D_{cr} = n + (\varepsilon_n - n) T/l_e$$

- Failure based on strain rate influence as described in section 2.2.4 using the algorithm provided by Paik et al. A simple script was programmed to follow this algorithm in order to obtain the dynamic failure strain value to be inserted in the material model card.

## 2.4. FEM Modelling and Simulations

### 2.4.1. Model Extent

The dimensions of the actual stiffened hull panel are shown in table 4. Some assumptions as follows were made, in order to be able to model correctly the idealised grillage:

- The stiffener end plates and stiffener end plate spacers (highlighted in green in figure 8) in the actual model were necessary to provide clamped boundary conditions to the stiffeners. Assuming their effects on the overall structural behaviour is negligible, then the stiffener webs and flanges were considered to be the same length as the corresponding plate dimension.
  - Also, the long and short plate boundaries (highlighted in red in figure 8) exist to provide clamped boundary conditions to the plate. These plate boundaries were ignored assuming they do not change actual dimensions of the plate.
-

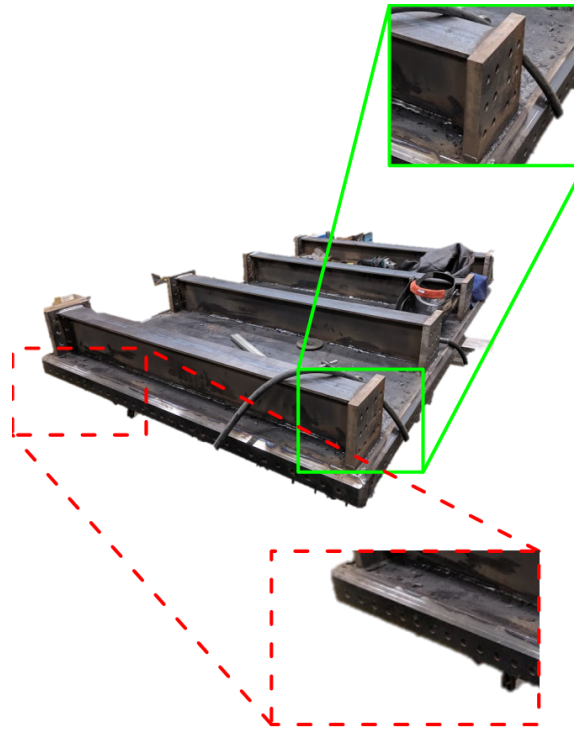


**Figure 8:** Illustration of assumptions for reproducing idealised model

With these assumptions, the idealised stiffened hull panel is characterised with the following dimensions as tabulated below:

**Table 5:** Idealised Stiffened Hull Panel (Grillage) Dimensions

Grillage Parts	Length (m)	Breadth (m)	Thickness (mm)
Plate	2.032	1.36	7.9
Stiffener Web	1.36	0.17	7.9
Stiffener Flange	1.36	0.1016	7.9
Stiffener Spacing	0.60945		

The modelling of the grillage and indenters were done using the MSC Patran/Nastran software. The plate, stiffeners and indenters were all modelled using shell elements. Material properties in table 1 were assigned, and dimensions from table 5 were used for the modelling. The idealised model is shown in the figure 9.

---

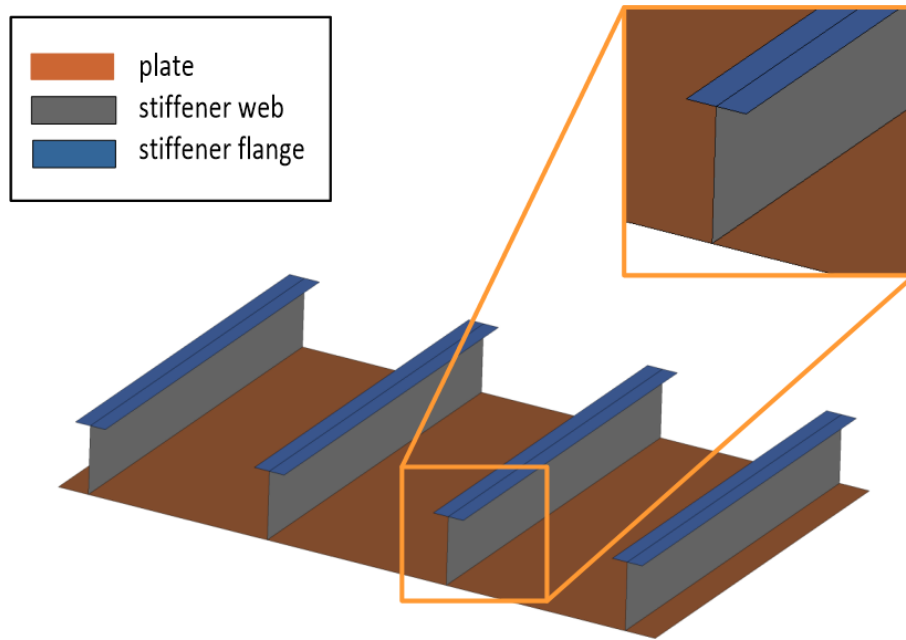


**Figure 9:** Idealised model for FEA

Furthermore, the smooth indenter was modelled as shown in the figure 10. Although, the smooth indenter has been known not to have induced fracture to the plate, several failure criterion and material models will be used for sensitivity analyses.

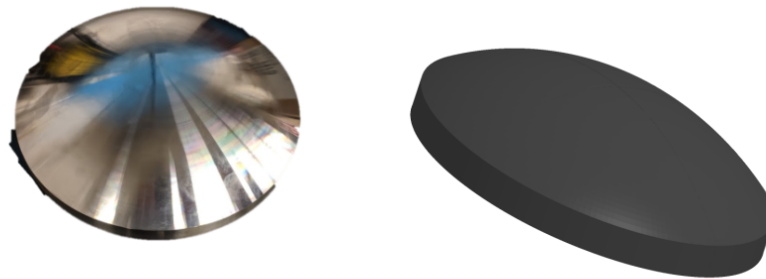


**Figure 10:** Smooth Indenter: a). Actual indenter b). Idealised model

The non-smooth indenter has the purpose of inducing a state of stress in the impacted plate that changes dramatically as the impact progresses with time. This non-smooth rigid indenter consists of a spherical cap transitioning into a tetrahedron-like shape. The spherical cap makes first contact with the hull plating, nominally inducing a state of biaxial tension in the hull plating. As the impact progresses, the hard chimes marking the transition from the spherical cap to the tetrahedron induce a combined state of tension and shear (Quinton, 2020). This hard shine is highlighted in green as shown in the figure 11 below.

---

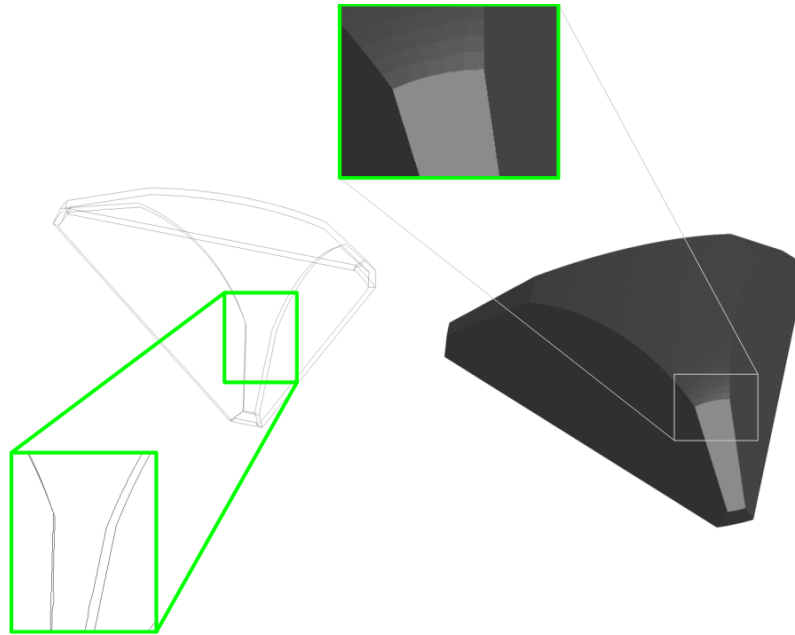


**Figure 11:** Modelled Rough Indenter

#### 2.4.2. Finite Element Model Description

The FE code utilised for the numerical analyses was the LS-DYNA nonlinear explicit code, because it is suited to for the analyses of dynamic nonlinear response (large displacements, plasticity) which may arise due to geometry, material or constraints. The version used was the LS-DYNA R V4.3.12 64bit. MSC Patran/Nastran was used to generate the geometry mesh and the outputs were imported into the LS-DYNA PrePost.

The extent of the geometry has been described in section 2.4.1. Furthermore, the grillage was clamped at the four edges of the plating and on the two longitudinal edges of the stiffeners to model the boundary conditions. Also, the grillage does not undergo any movement. The indenter was modelled as a rigid body, and only allowed to move in the direction of impact. Figure 12 gives pictorial representation of the setup.

The indenter was given an initial velocity of 4.429m/s toward the direction of impact using the INITIAL\_VELOCITY card in LS-DYNA in order to prescribe an initial velocity at the moment of the impact to the nodes of the indenter.

Also, from the experiment it was stated that both the grillage and the indenter were in motion, and the total energy at the moment of impact was equal to 88.3 kJ (see table 2). Furthermore, since the impacting and impacted structures (both carriages from the laboratory experiment) have the same mass and velocity at the moment of impact. As a consequence for the idealised model set-up, if the grillage is assumed fixed - it is clamped at all edges, the indenter kinetic energy have to be doubled. This implies that the mass of the indenter can be doubled :  $4500 \times 2 = 9000$  kg. Therefore, the density of the indenter was therefore increased to obtain an indenter of 9 tons.

---

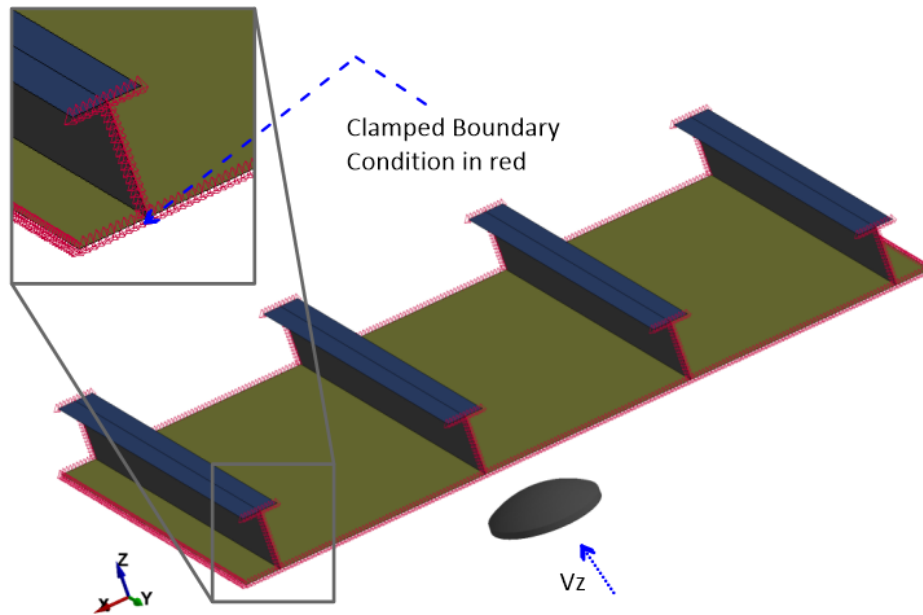


**Figure 12:** Simulation Set Up

The Belytschko Lin-Tsay shell elements (reduced integration method) with five integration points through the thickness were implemented. This was applied to the indenter, grillage plating, the stiffeners web and flange. This element formulation has particular methods for addressing hourglass effects resulted due to reduced-integration formulation, warping which occurs when a single shell element is out of plane, and shell theory (Quinton et al, 2016).

A mesh sensitivity study was carried out to determine the optimal mesh size of the finite element model. Four mesh sizes were investigated [8, 10, 15, 20]mm while maintaining a mesh size aspect ratio of unity to increase the quality of the element. From the mesh study, the optimum mesh size which was suitable to capture the grillage response was the 10mm mesh size with an approximate  $l/t = 1.3$ . It is important to note that, in order to avoid irregularities, the indenter mesh size was approximately the same as that of the plate.

For the application of moving load, the contact between the grillage and the indenter was initiated using the CONTACT\_AUTOMATIC\_SURFACE\_TO\_SURFACE card in LS-DYNA, with a static friction coefficient of 0.3, which is justifiable for friction between steel surfaces. Care was taken to ensure that there were no contact detection issues by optimising the proximity between the indenter and the grillage, and that the penalty contact detection algorithm is working as expected. Contact between the grillage parts was initiated using the CONTACT\_AUTOMATIC\_GENERAL formulation.

Because of the dynamic nature of the experiment, strain rate effect has to be taken into consideration. Two material models were used as behaviour law cards for comparison: Piecewise plasticity and Power law. The material properties used are available on table 1.

---

Additionally, Poisson coefficient = 0.33, tangential modulus = 1018 MPa, and Density = 7850 kg/m<sup>3</sup> were utilised.

Failure criterion was given for the plating, but for the webs and flanges, the failure strain was set to 0, because failure strain formula applies only for membrane tension deformation mode, which is not the case for the webs and flanges. In other words, only the plating is expected to fail.

### Sensitivity of failure criteria to mesh size

Generally, the choice of failure criteria to be used for impact analysis is still an ongoing research, as different conditions may lead to early or delayed fracture. The figure 13 shows how different failure criteria respond with respect to change in mesh size. It is evident that depending on the criterion, different mesh sizes yielded different effective plastic strain values. Furthermore, the finer the mesh, the higher the strains calculated at integration points in the elements at the vicinity of a hole and the more rapid erosion (element deletion) will take place.

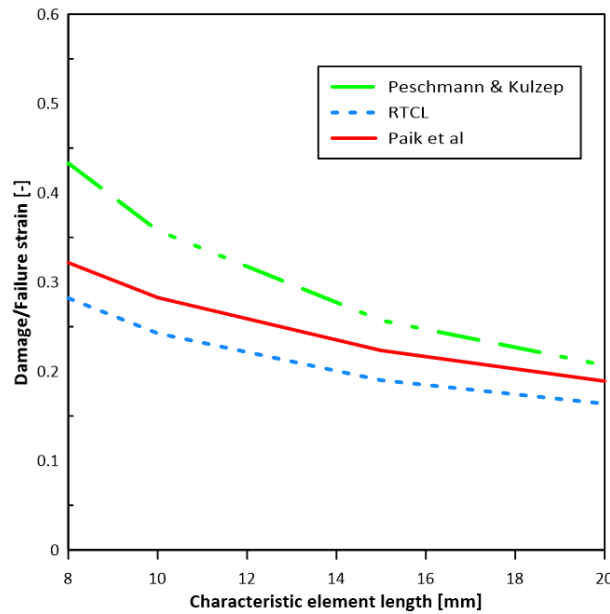


**Figure 13:** Sensitivity of the EPS, RTCL and Paik failure criteria to the mesh size.

As a compromise with computational time, and regards to accurate capture of strain concentration, 10mm mesh size was used for the numerical simulations. The machine used for these simulations was HP Intel(R) Xeon 3.40GHz processor, 12Gb ram and with 8 logical processors. Simulation time for one analysis was roughly 12 minutes.

**Table 6:** Failure criteria data for simulations: mesh size = 10mm

Paik et al	Pechmann and Kulzep	RTCL $D_{cr}$
0.283	0.358	0.243

## 2.5. Smooth indenter results: sensitivity to failure criteria

### 2.5.1. MAT24: Piecewise Linear Plasticity sensitivity to failure criteria by neglecting strain rate effect

The plots of force and internal energy using different failure criteria are shown in the figures below;

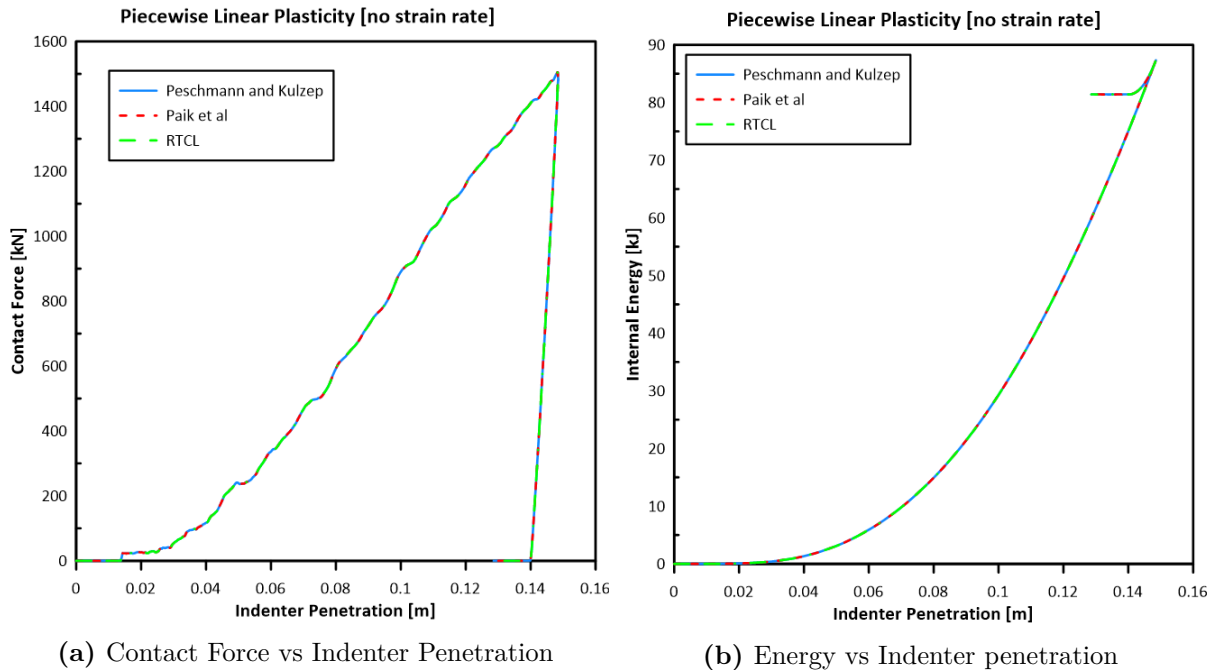


**Figure 14:** Force and Energy Plots for MAT 24 with different failure criteria

The indentation and deflection pattern of the grillage is shown in the figure below

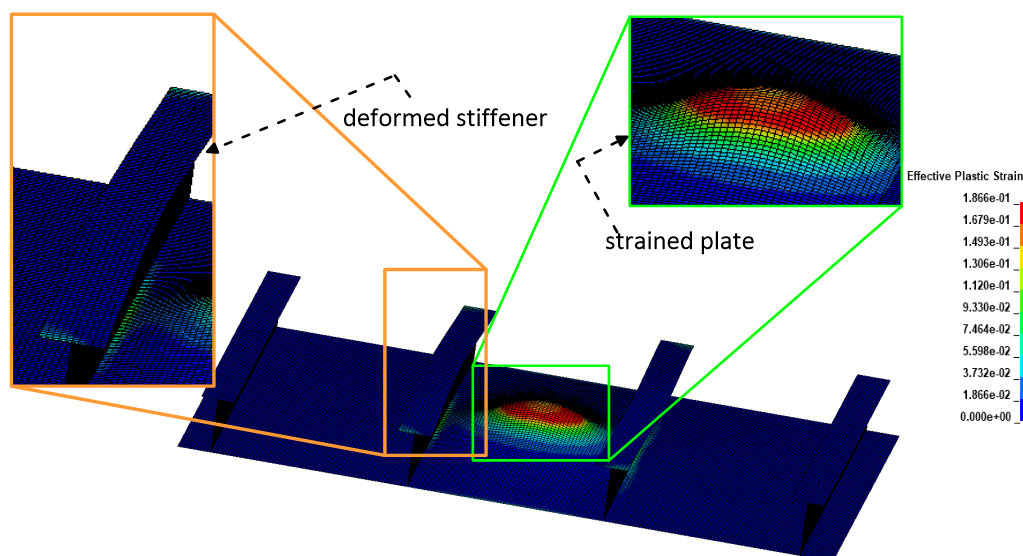


**Figure 15:** Grillage deflection and location of overstrained elements

From the plots in figure 14 it can be observed that all failure criteria followed same curve, and the grillage absorbed almost all the kinetic energy of 88.3 kJ with a maximum contact force of around 1500 kN. Furthermore, there was no fracture of the plate, but there was a deflection of the stiffener web and flange close to the point of impact which was due to strain distribution.

### 2.5.2. MAT24: Piecewise Linear Plasticity sensitivity to failure criteria by considering strain rate effect

By considering strain rate effects due to the high speed of impact the following results were obtained.

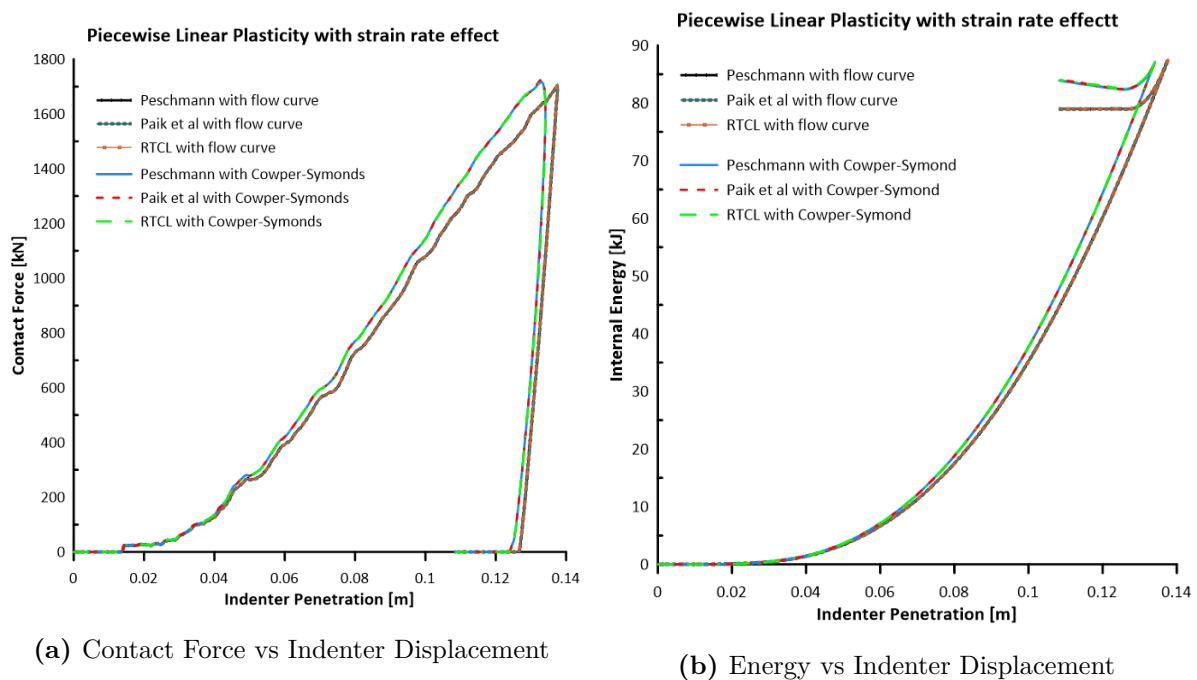


**Figure 16:** Force and Energy Plots for MAT 24 using different failure criteria

From figure 16, because of the strain rate consideration in absorbing the kinetic energy, there was an increase in the contact force (about 13%) and decrease in indentation time to reach maximum kinetic energy. The penetration depth was decreased as compared to results obtained without considering the strain rate effect. It is interesting to note that the flow curve plot attained a little indentation penetration more than the Cowper-Symonds strain rate plot.

### 2.5.3. MAT18: Power Law Plasticity sensitivity to failure criteria by neglecting strain rate effect

The results for the internal energy and contact force using the MAT 18 behaviour law without strain rate consideration are shown below.

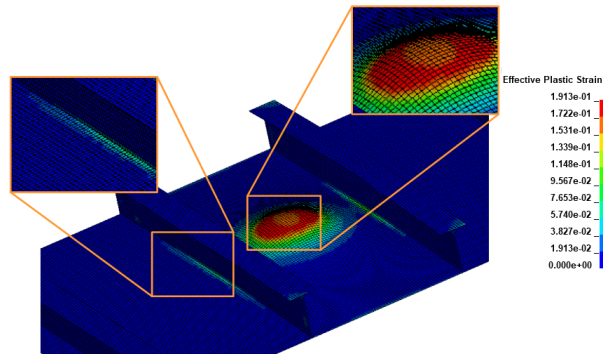


**Figure 17:** Grillage deflection and location of overstressed elements for power law

From figure 17, we can observe that with power law for the smooth indenter, the plate also did not attain fracture. Because of the smooth nature of the indenter which does not induce a combine state of tension and shear, the grillage plating likewise experienced over-straining at the point of impact. The intersection between the plate and the stiffener web also experienced some straining. Furthermore, the two stiffeners at close proximity with the point of indentation observed same deflection pattern as with Piecewise Linear Plasticity, as shown in figure 17. Furthermore, from figure 18, all failure criteria followed as expected the same curve pattern which implies that in this case; using the power law for the smooth indenter without strain rate consideration, the failure criteria had no influence on the results because there was no failure.

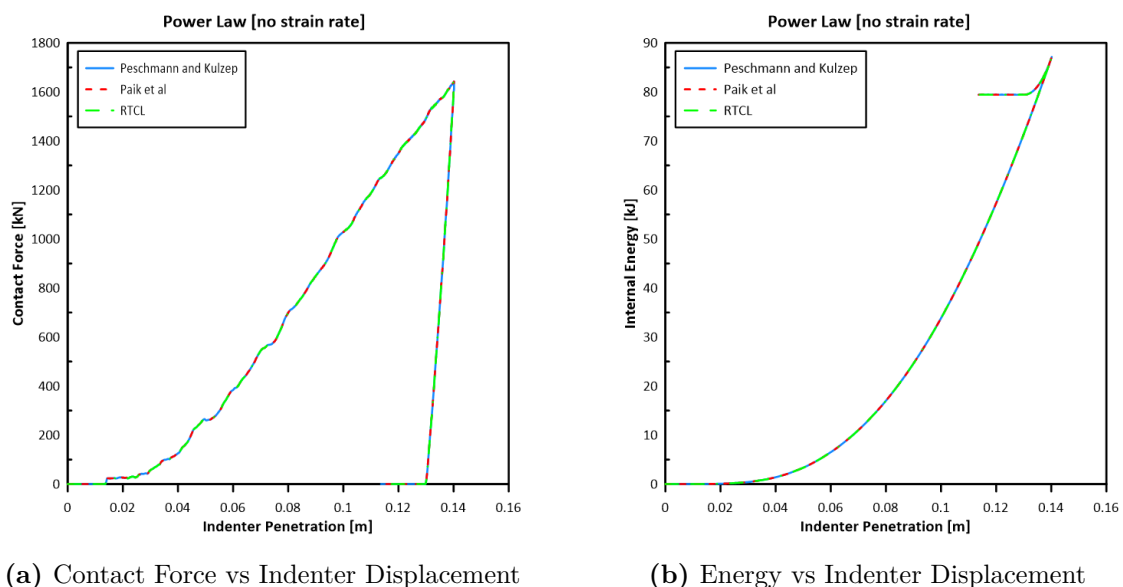


**Figure 18:** Force and Internal Energy Plots for Power Law using different failure criteria

---

### 2.5.4. MAT18: Power Law Plasticity sensitivity to failure criteria by considering strain rate effect

With the Cowper-Symonds parameter:  $C=3200$  and  $P = 5$ , the strain rate was accounted for and the results obtained are shown below;

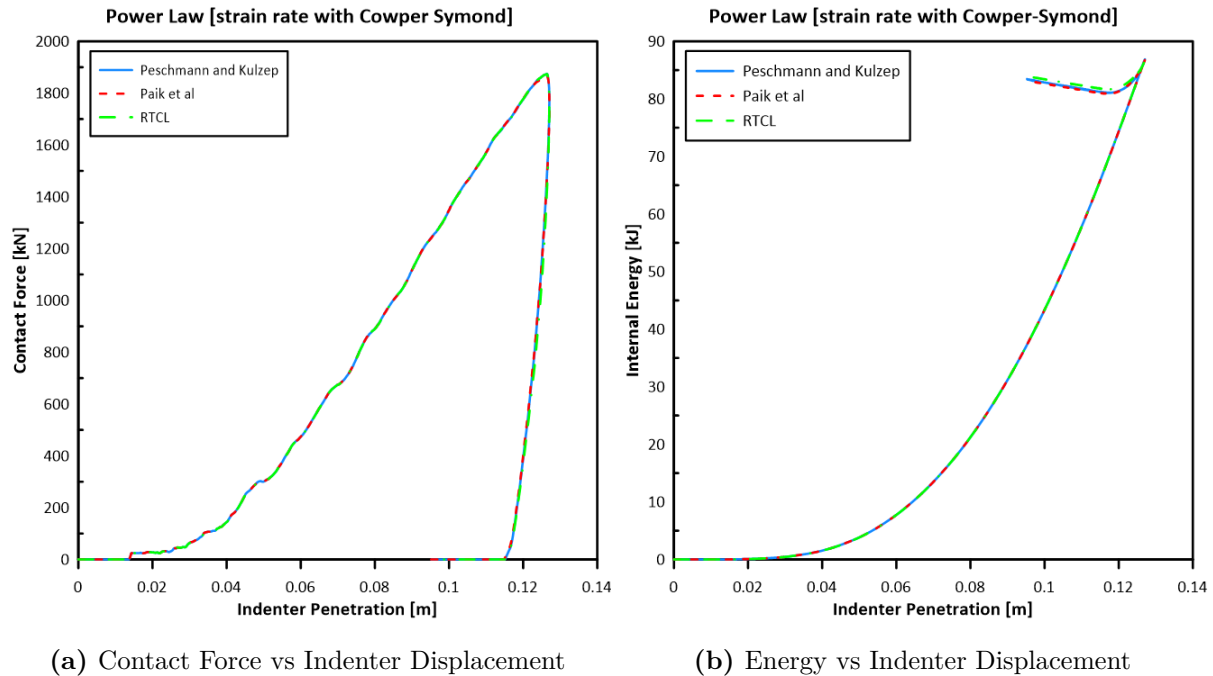


**Figure 19:** Force and Internal Energy Plots for Power Law using different failure criteria

When the Cowper-Symonds strain rate parameters are considered for the power law, the indentation period reduced, indentation depth decreased, and the force required to absorb the kinetic energy increased by 12% as compared to power law without strain rate effect. This shows the influence of strain rate in both material models. Moreover, the influence of the failure criteria cannot be examined in this case because, the smooth indenter did not fracture the plate.

## 2.6. Rough indenter results: sensitivity to failure criteria

### 2.6.1. MAT24: Piecewise Linear Plasticity sensitivity to failure criteria by neglecting strain rate effect

Due to the nature of the rough indenter, there exist the possibility of fracture at some point in time during indentation. An energy balance is always useful to verify that the transfer of energy (kinetic  $\geq$  internal + sliding) seems to be physical. An energy balance for a rough indenter simulation is shown below;

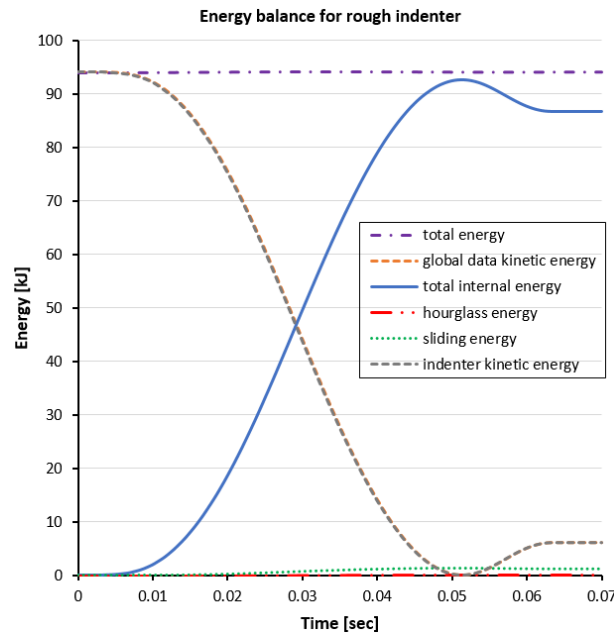


**Figure 20:** Energy balance for the rough indenter using Peschmann & Kulzep failure criteria

Although this energy balance was plotted for the case without strain rate consideration using the Peschmann and Kulzep failure criteria, it can be applied to other cases of rough indenter simulations. The major aim was to illustrate that the sum of the total internal energy, hourglass energy and sliding energy must be less than or equal to the initial kinetic energy. The initial kinetic energy of 94.11 kJ for the rough indenter simulation will be constant irrespective of the simulation case, but the other energies will vary.

By plotting also the total energy which is constant and equal to the initial kinetic energy, It can be verified that the energy balance is physical. As the hourglass is concerned, the hourglass energy must be kept lower than 5% of the total internal energy.

The force and energy plots for Piecewise Linear Plasticity when strain rate effect are neglected are shown below;

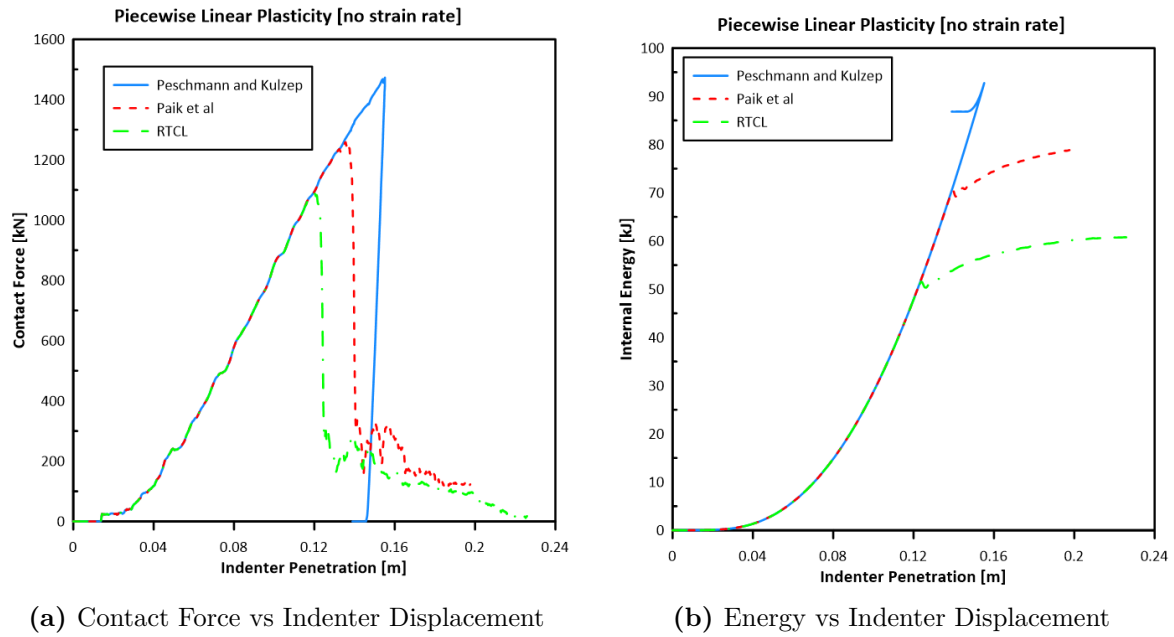


**Figure 21:** Force and Energy Plots for Piecewise Plasticity using different failure criteria

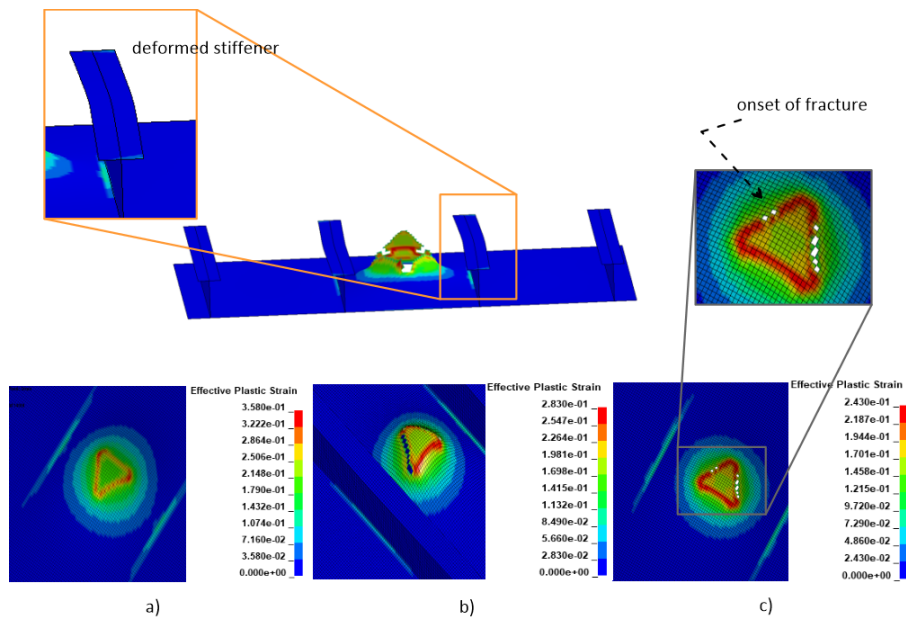


**Figure 22:** Grillage deflection and location of highly strained elements/fracture: a) Peshmann, b) Paik et al, c) RTCL

By neglecting the influence of strain rate, it can be observed from the figure 21, that with RTCL and Paik et al formulations for predicting the failure, caused a fracture of the grillage as can be observed in the figure 22. The plate could not absorb all the initial kinetic energy of the indenter prior to failure. Peschmann and Kulzep formulation caused the plate to have more resistance to penetration because of the higher value of the effective failure strain which led to the plate absorbing an additional 5% of energy. Thus, the plate did not fracture.

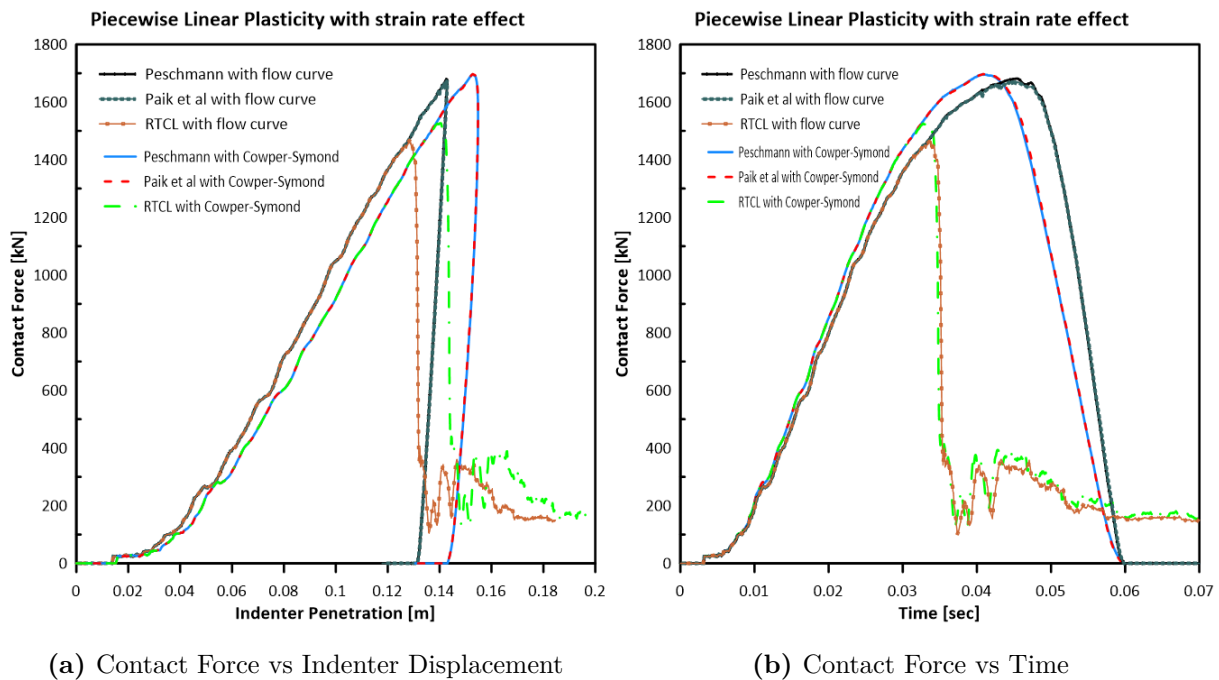
From figure 22, the deflection of the two stiffeners at close proximity to the point of impact is shown, this is due to the boundary condition. Furthermore, there exist strain concentration at the joints connecting the stiffener webs to the plate.

Figure 22(a), (b), (c) represent the behaviour of the plating according to the failure criteria implemented. Figure 22(c) shows that the onset of fracture occurred at the hard chine of the non-smooth indenter which led to the inducing of fracture.

### 2.6.2. MAT24: Piecewise Linear Plasticity sensitivity to failure criteria by considering strain rate effect

Two strain rate methodologies for considering strain rate effect are: with flow curve and with the Cowper-Symonds strain rate parameters. The flow curve is the effective plastic stress versus effective plastic strain data which was extracted from the modified true stress-strain curve obtained from experiment (see section 7).

The results obtained while considering the strain rate effect using the MAT 24 behaviour law are shown below:



**Figure 23:** Force Plots for Piecewise Linear Plasticity using different failure criteria

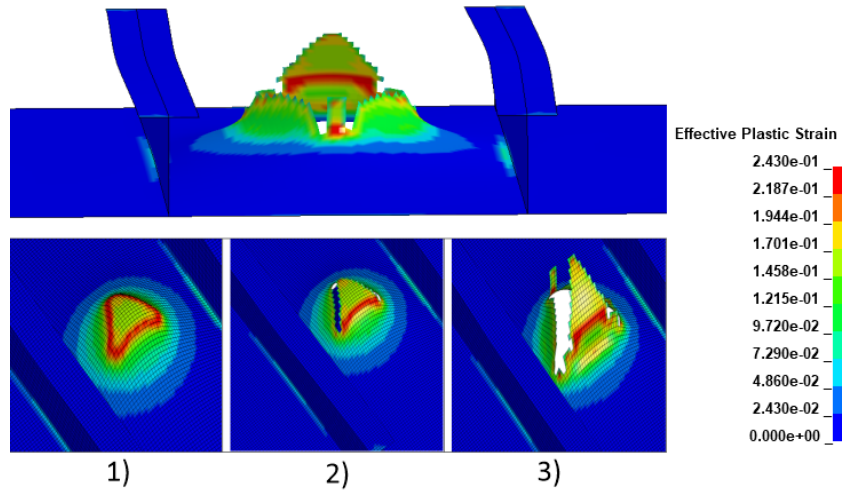


**Figure 24:** Grillage deflection and stages of fracture for RTCL damage criteria

When the influence of strain rate is taken into account, the resistance to penetration of the stiffened hull panel increased by more than 13% for both conditions of flow curve and Cowper-symond parameters. This is due to the rate effect of the material. Furthermore, in this case fracture was observed only with the RTCL damage criteria.

Figure 24 shows the stages of damage evolution from stage 1 to 3. In stage 1, it can be observed that strain concentration is higher at the surrounding elements in contact with the hard chine of the non-smooth indenter. Similarly, the stiffeners close to the point of contact can be observed to have undergone slight tripping due to the impact.

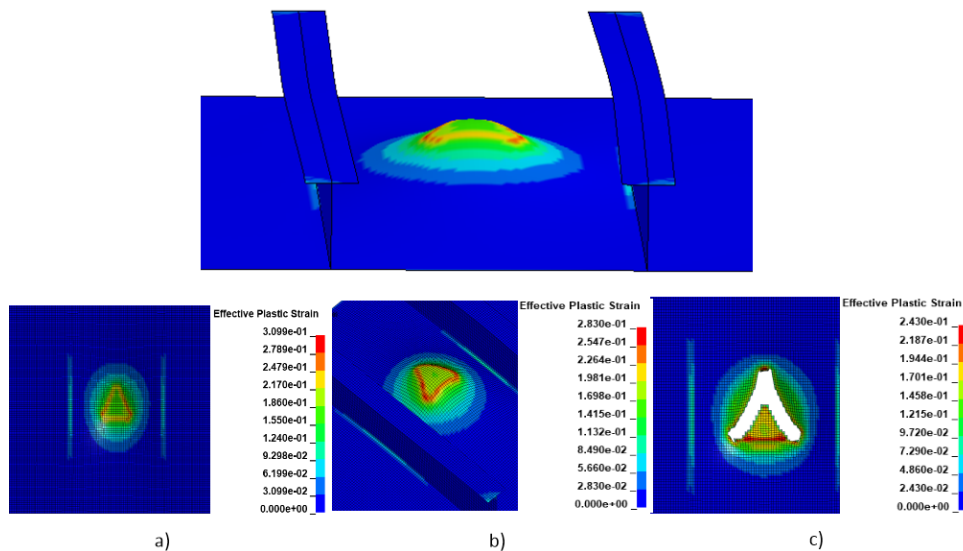
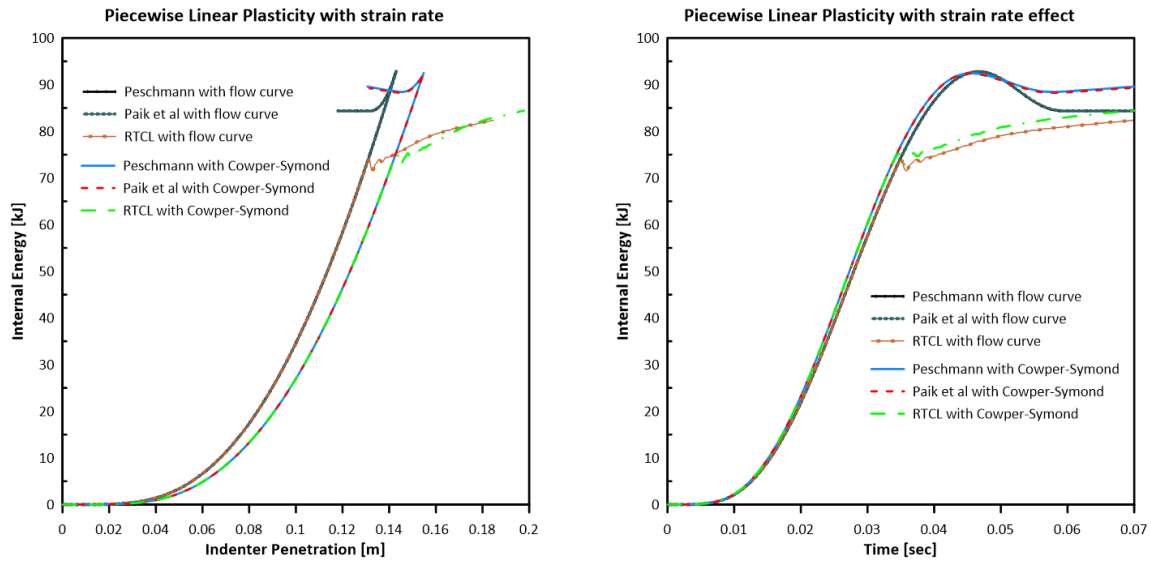


**Figure 25:** Grillage deflection and location of highly strained element/fracture for Cowper-Symond strain rate effect: a) Peshmann, b) Paik et al, c) RTCL



(a) Internal Energy vs Indenter Displacement

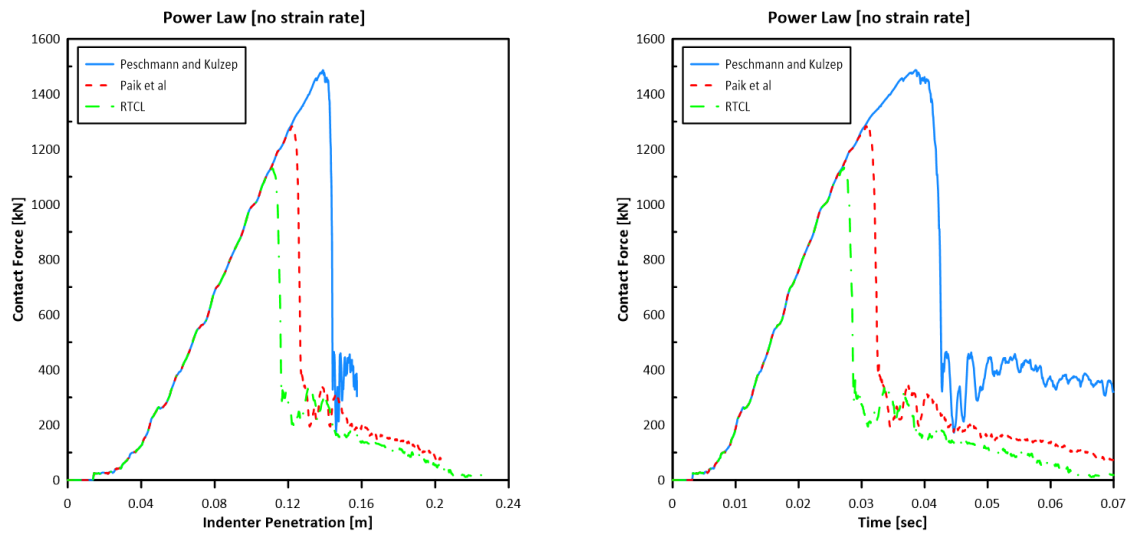
(b) Internal Energy vs Time

**Figure 26:** Energy plots for Piecewise plasticity for different failure criteria

Figure 25 illustrates the behaviour of the grillage for different failure criteria. Peschmann and Kulzep, and Paik et al criteria achieved denting of the grillage plating, while RTCL damage criterion fractured the plate at about 0.035 seconds.

The internal energy absorbed by the grillage varies depending on the failure criteria, for instance with the RTCL damage criteria the maximum energy absorbed was about 82 kJ which is around 87% of the initial kinetic energy, while with Peschmann and Kulzep, the maximum energy absorbed was about 97% of the initial kinetic energy of the rough indenter. Furthermore, in terms of indentation depth, the maximum penetration was achieved using the Cowper-Symonds strain rate parameters.

### 2.6.3. MAT18: Power Law Plasticity sensitivity to failure criteria by neglecting strain rate effect



(a) Contact Force vs Indenter Displacement

(b) Contact Force vs Time

**Figure 27:** Force Plots for Power law plasticity for different failure criteria

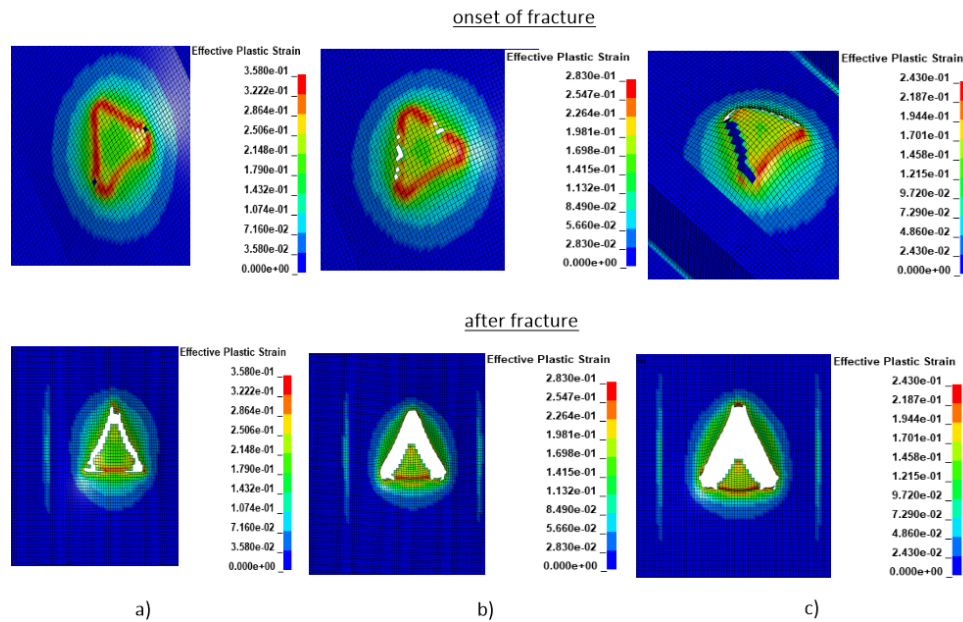


**Figure 28:** Grillage location of fracture for power law without strain rate effect: a) Peshmann, b) Paik et al, c) RTCL

When the influence of strain rate is ignored, it can be observed from figure 27 that the three failure criteria lead to fracture of the plate with the maximum resistance to penetration being with the Peschmann and Kulzep failure model at about 0.14m of indenter penetration. The fracture initiation and evolution is shown in figure 28. All three failure criteria followed the same fracture propagation pattern due to the nature of the non-smooth indenter.

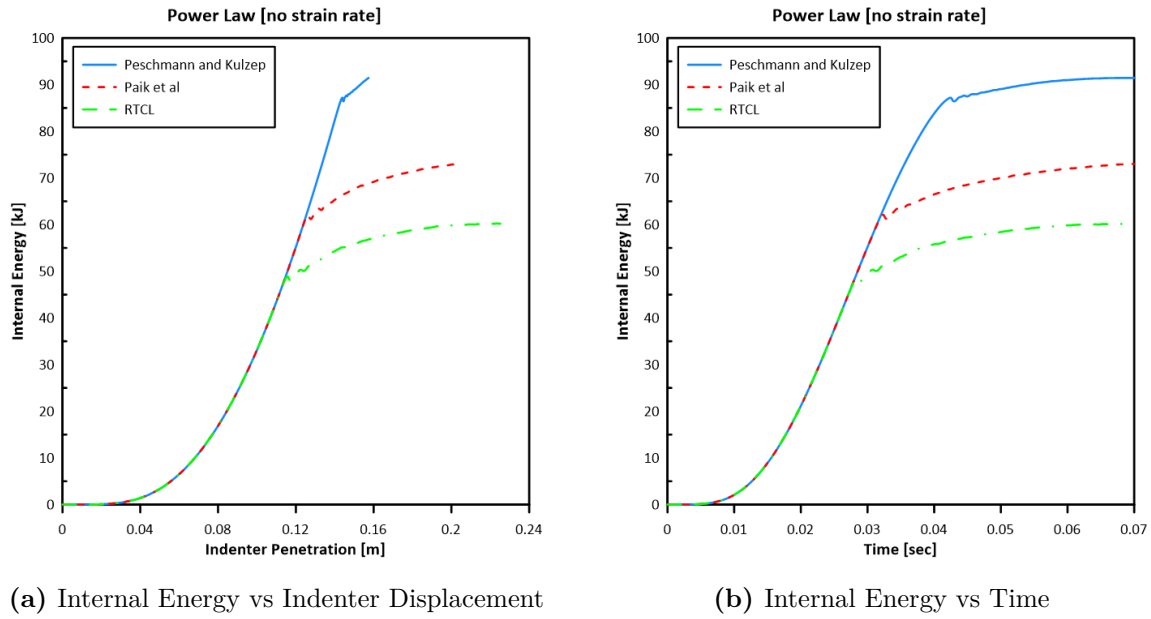


**Figure 29:** Energy plots for Power law plasticity for different failure criteria

With regards to energy absorption, the area under the force-displacement plot shows that the grillage with RTCL damage model had the least energy absorption capacity. As shown in figure 29, the maximum absorbed energy with the RTCL model was about 30% less than the maximum kinetic energy from the experiment and about 67% of the initial kinetic energy of the indenter which is not the case for Peschmann and Kulzep failure model which absorbed about 97% of the initial indenter kinetic energy.

The energy balance for the RTCL damage criteria is given in figure 30. It can be observed that after rupture, the indenter keeps some kinetic energy.

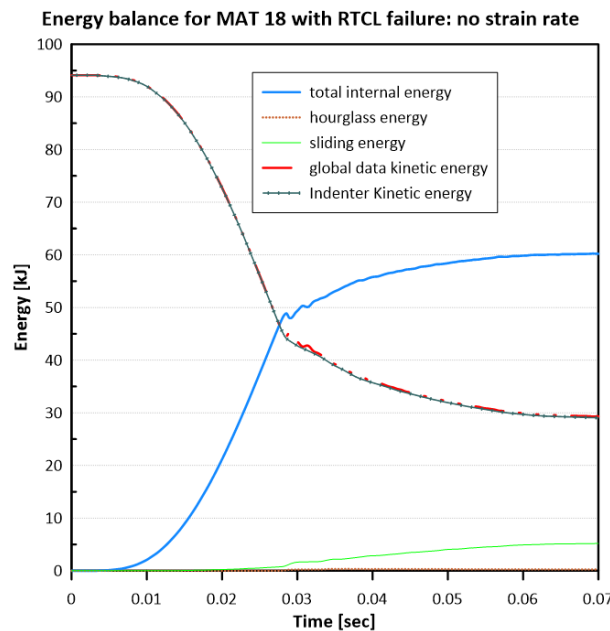


**Figure 30:** Energy balance for RTCL failure criteria with rough indenter

### 2.6.4. MAT18: Power Law Plasticity sensitivity to failure criteria by considering strain rate effect

Utilising the Cowper-Symonds strain rate sensitivity parameters  $C$  and  $P$ , we can check the influence to fracture propagation. The results for this case is shown in the figures below:

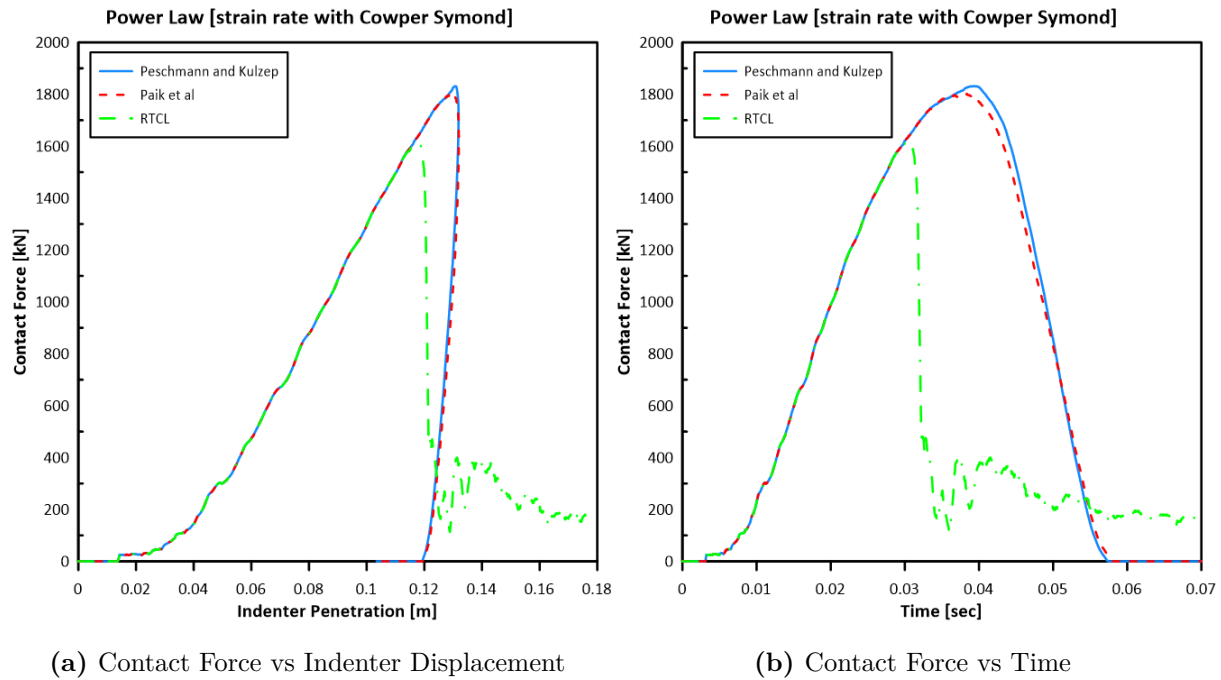


**Figure 31:** Force Plots for Power law plasticity for different failure criteria

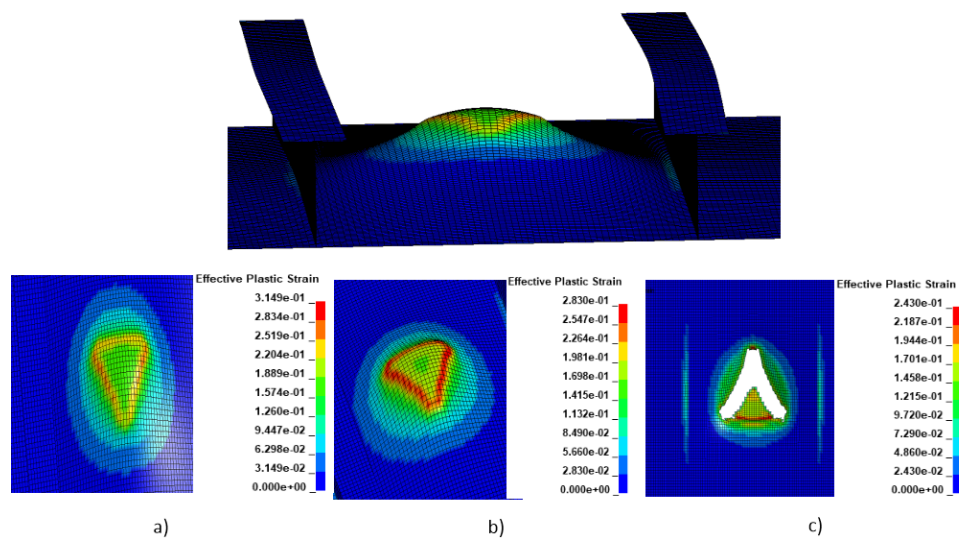


**Figure 32:** Grillage location of highly strained elements/fracture for power law with strain rate effect: a) Peshmann, b) Paik et al, c) RTCL

From the results, it can be observed that the consideration of strain rate effect can cause a tremendous change in the behaviour of the plate. Especially considering the RTCL damage criteria, the resistance to penetration of the plate increased by about 45% as compared with previous result without the influence of strain rate. Furthermore, the penetration depth increased because of the increase in contact force.

Figure 32 shows the nature of deflection of the plate and the stiffeners close to the point of impact. It also illustrates the influence of the failure criteria to plate fracture, as it is obvious that with Peschmann-Kulzep failure formulation, fracture was not induced to the plate. With the Paik et al formulation, there was significant plastic straining, which might result in fracture if the effective plastic strain was to be varied say 5% less. Figure 33 shows the high influence of strain rate consideration to the energy absorption of the grillage. With strain rate consideration, Paik et al formulation behaves almost alike to Peschman-Kulzep formulation.

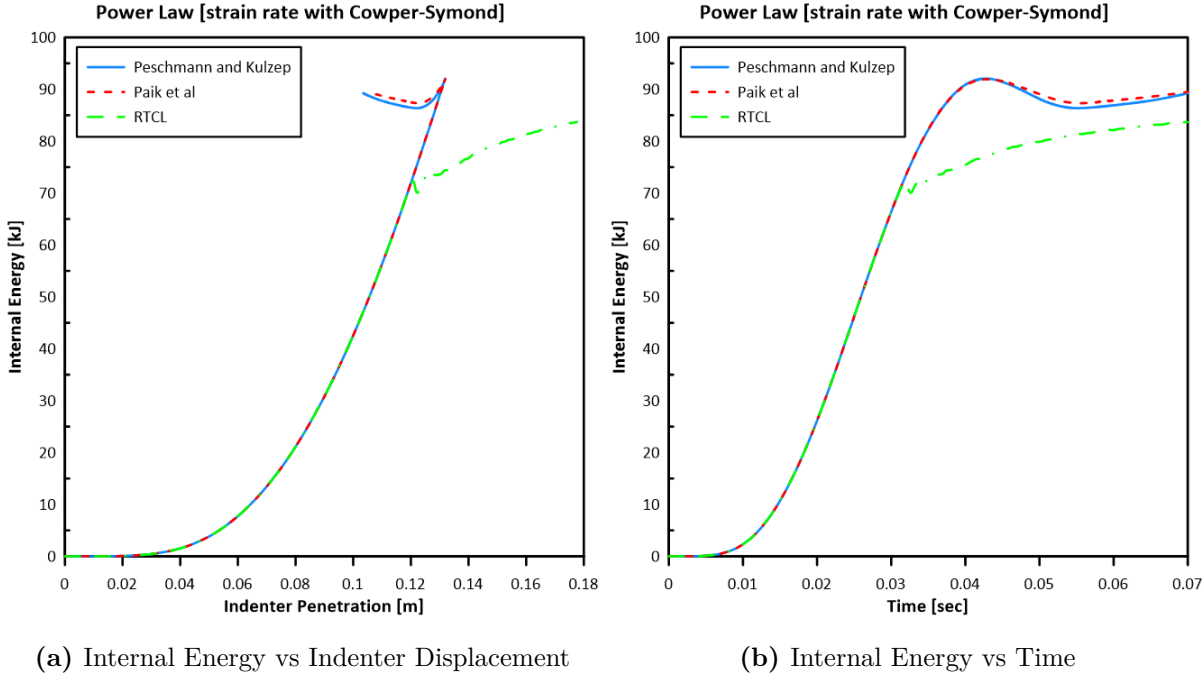


**Figure 33:** Energy plots for Power law plasticity for different failure criteria

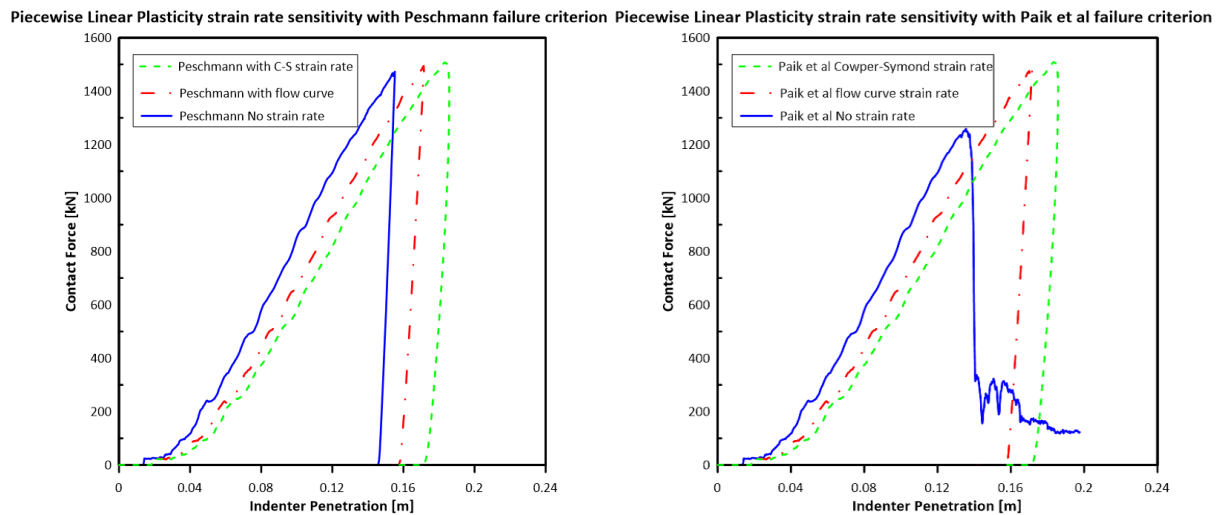
## 2.7. Further sensitivity analyses on rough indenter results

### 2.7.1. Strain Rate Effect

The idea of considering the strain rate effect is to show the influence of the dynamic nature of impact to fracture. In this study, because of brevity focus will be on the **non-smooth indenter**. This is due to the fracture initiation when using different behaviour laws and failure criteria.

The MAT 24: Piecewise Linear Plasticity will be used for the strain rate sensitivity analyses, because of brevity and also, it has been known to yield good results when carrying out impact studies. Furthermore, two failure criteria will be used; Peschmann & Kulzep which is commonly utilised by researchers and the Paik et al criteria which was developed for dynamic impact studies.

The force indenter displacement plots for both failure criteria are shown in figure 34.



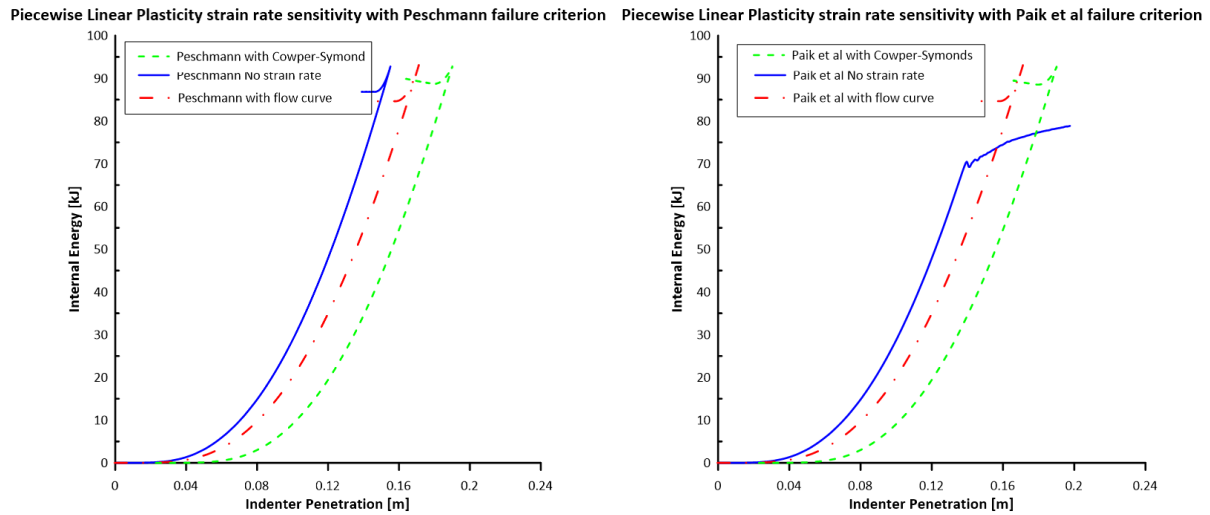
(a) Force vs Indenter Displacement Peschmann      (b) Force vs Indenter Displacement Paik et al

**Figure 34:** Force plots for different different failure criteria showing strain rate sensitivity

We can observe the influence of strain rate to the indenter penetration and to the contact force when different failure models are taken into account. For instance, the Paik et al failure criteria under estimated the resistance to penetration when strain rate is not taken into consideration.

There was a drastic change in the value of contact force required to induce fracture on the plate when strain rate is taken into consideration. The contact force using the Paik et al failure criteria increased by more than 11%. Similarly, the indentation increased by more than 20% when the influence of Cowper-Symonds strain rate is taken into consideration.

The energy indenter displacement plots for both failure criteria are shown in figure 35.



(a) Energy vs Indenter Displacement Peschmann      (b) Energy vs Indenter Displacement Paik et al

**Figure 35:** Energy plots for different different failure criteria showing strain rate sensitivity

The influence of strain rate using the Peschmann and Kulzep failure criteria was more pronounced with regards to the indenter penetration as there was about 20% increase with Cowper-Symonds strain rate sensitivity parameter, and about 13% increase with the effective stress-strain curve. This is also due to the value of the failure strain implemented. It can be noticed that as a consequence of lower resistance to penetration fracture occurred hurriedly when strain rate effect is neglected which is visible with the Paik et al formulation.

Despite the role played by the strain rate in dynamic loading, it is also important to point out the influence of the failure strain value to fracture initiation. As it is known that fracture is initiated when the effective plastic strain at all integration points have exceeded the effective plastic strain value inputted in the material model card. This makes it a challenge to know which failure criteria is best. With regards to the energy absorption, we can check which failure criteria can be well suited. For instance if the grillage is assumed to absorb all the total maximum kinetic energy of 94.11 kJ. Therefore, from the plots we can make a choice as to which failure criteria together with the strain rate effect consideration were close to this energy absorption value.

### 2.7.2. Different Behaviour Laws

Checking the sensitivity of the piecewise plasticity and the power law material laws to different failure criteria; Peschmann & Kulzep and Paik et al, the following results were obtained.

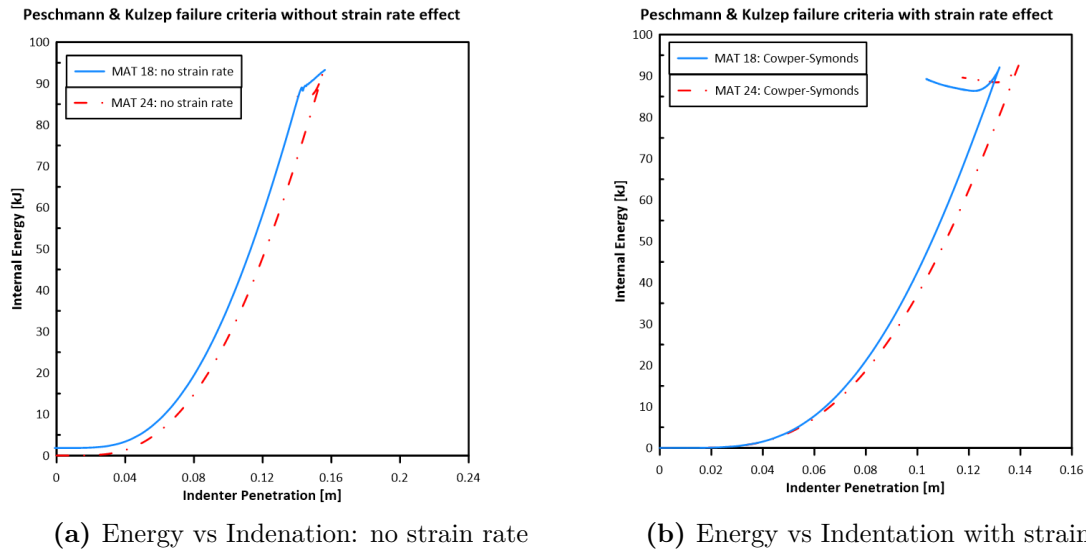


**Figure 36:** Internal Energy plots for MAT24: Piecewise Plasticity and MAT18: Power Law

It can be observed from figure 36 that with the Peschmann and Kulzep failure criteria, the sensitivity of both material models are alike with respect to energy absorption and resistance to penetration. Major difference is that the indenter penetration varies as the penetration depth is much lesser without strain rate effect, because the grillage fails earlier when the strain rate is not accounted for. Also, without strain rate effect the power law model attained rupture of the grillage at about 0.145m indenter penetration.

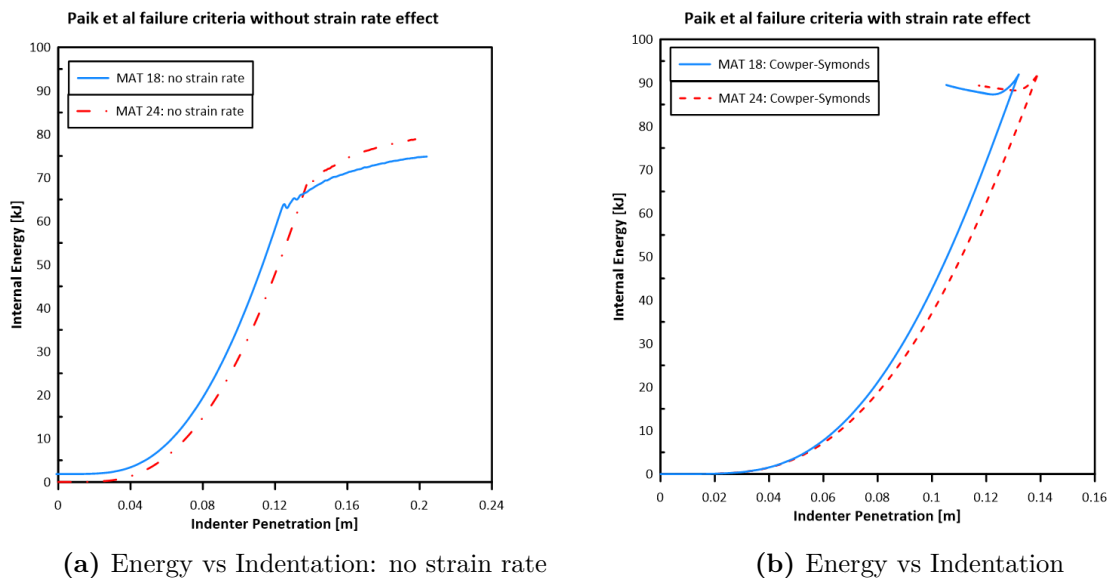


**Figure 37:** Internal Energy plots for MAT24: Piecewise Plasticity and MAT18: Power Law

---

With the Paik et al failure formulation, the initiation of fracture only occurs when the strain rate influence is neglected as can be observed from the figure 37 for both material models. When strain rate is taking into account, both material models also behave alike with respect to internal energy and contact force, and has more pronounced difference in indenter penetration. This is also due to the contributing effect of the value of the effective failure strain.

## 2.8. Discussion and Conclusion of Benchmark study

From this impact study, the influence of various parameters such as the strain rate, the material model, the failure criteria and the nature of the indenter have been studied. The purpose of this study was to investigate the different ways to model the impact of a rigid indenter to a deformable metallic grillage.

This work presented a series of impact analysis of a stiffened hull panel using the smooth and non-smooth indenter. The analyses were conducted using the LS-DYNA explicit NLFE code. Based on two different behaviour laws and three failure criteria, several numerical simulations and analyses were carried out to check for sensitivity to these different conditions. It could be summarised that strain rate effect plays a major role in the considered impact scenarios, and should be considered in numerical simulations. Furthermore, with the power law being fitted correctly, its behaviour with respect to piecewise plasticity are alike.

It is also interesting to point out the high influence of failure criteria being utilised. Generally, in impact analyses the choice of which failure criteria to utilise is always a question. We have observed, that the RTCL and the Paik et al failure criteria were very sensitive to strain rate effect with respect to resistance to penetration, energy and fracture initiation. Furthermore, the Peschmann and Kulzep failure criteria difference was more pronounced in terms of indenter penetration time and depth when strain rate and different material models were investigated.

With regards to which failure criteria to utilise, it would be recommended to select the Paik et al formulation because, Peschmann & Kulzep have recommended that their criteria is well suitable for a characteristic element length to thickness ( $l_e/T$ ) ratio greater than 5, but in this study the  $l_e/T$  was about 1.3. Secondly, Paik et al criteria was strictly formulated for dynamic loading condition to take into consideration the strain rate effect. Finally, in terms of energy absorption and resistance to penetration, we have seen that the Paik et al formulation gave realistic results when strain rate effect is considered.

In terms of fracture initiation and stiffener deflection pattern, it was observed that the hard chine in the non-smooth indenter served as an initiation mechanism of fracture as compared with the smooth indenter which does not initiate fracture. The two stiffeners

---

close to the point of impact have been seen to undergo deformation due to the impact force of the indenter to the plate with major strain localisation at the intersection between the stiffeners and the grillage plating.

Finally, it has been demonstrated that numerical technologies are capable of capturing damage and fracture due to dynamic impact, provided that good models for predicting fracture are employed. Also, this shows that impacts may not always be quasi-static, and that the impacting body will not always be smooth, but may have other shapes which are capable of inducing dynamic stress and shear states. Although, numerical analyses are cheaper to execute than experimental analyses, results validation are based on experiments. This experimental validation will serve as a basis for future numerical models in investigating impact analyses.

### 3. SHIP GROUNDING

Ship grounding is a phenomenon whereby a ship impacts on seabed obstructions. It can be impact on rocks, shoals, or reefs as shown in figure 38. Accidental grounding events causes breaching of ship hull and may lead to water ingress. This in turn will have critical influence of structural integrity, and in case of excessive flooding, may lead to total ship loss.

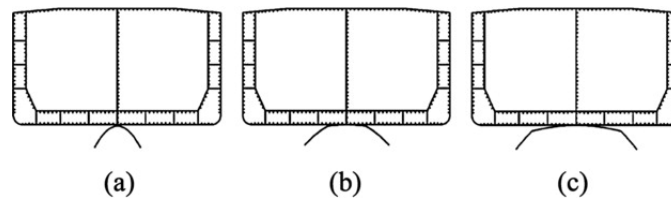


**Figure 38:** Different seabed topologies: (a) rock, (b) reef (c) shoal (From: Alsos, 2007).

It has been observed that loading condition, size and the shape of the seabed topology greatly influence the degree of damage. For instance, in figure 38 grounding on rock will lead to a tearing-dominating failure mode of the hull structure, while grounding on shoal may not lead to tearing but denting which will affect the global hull girder resistance and may give rise to hull collapse (Lin et al, 2007).

This chapter aimed to utilise the rock seabed topology to illustrate that in ship grounding events, the damage extent is highly influenced by the external hydrodynamic forces, velocity of the ship, point of impact and location of the ship centre of gravity. Furthermore, multiple breaches simulation will be analysed to demonstrate that it is possible for several compartments of a ship to be damaged during grounding events. The LS-DYNA explicit NLFE code will be used in conjunction with the MCOL subroutine to account for the external hydrodynamic forces.

#### 3.1. Literature Review on Ship Grounding

Grounding events can be of three types;

- Mechanics of vertical action called stranding (Amdahl et al, 1992)
- Mechanics of horizontal action called raking (Wang et al, 1997)
- A combination of both vertical and horizontal actions.

According to (Hong and Amdahl, 2012), ship grounding can be divided into internal and external sub-model dynamics. With the Minorsky method being the pioneer when it comes to crashworthiness of ships. Furthermore, he stated that during stranding scenario, ship bottom structures behave like right angled collision of ship side shells structures.

### 3.1.1. Theoretical Approaches on Ship Grounding

Several models and assumptions for different purposes have been developed with the simplest being the Minorsky's (1959) one dimensional approach. Minorsky showed that the deformed volume of hull structure relates proportionally with its crashworthiness (Alan et al, 2009).

Simonsen (1997) developed a simplified analytical approach to calculate the structural resistance during raking grounding scenario. He used his formulation for developing the collision and grounding code DAMAGE.

A study on plate tearing by a rigid wedge, and bottom damage in ship grounding was investigated by Shengming Zhang (2001) by formulating a semi-empirical approach to determine grounding force in the case of raking grounding event. Furthermore empirical formulations for determining the damage resistance and the extend of the damage was developed.

The plastic mechanism analysis of the resistance of ship longitudinal girders in grounding was also investigated by Hong and Amdahl (2008). An analytical formulation for the total energy dissipation was formulated and basic folding mechanism was established. The horizontal resistance was also derived which according to Hong and Amdahl depends on crushing distance and wave angle. The empirical formulation agreed reasonably with numerical results.

Nguyen et al (2011) made a study on the dynamic grounding of ships and showed that the topology of the seabed is a key parameter to consider for response analysis during ship grounding. A generalised model for the shape of the seabed for ship grounding events was also introduced.

Hong and Amdahl (2012) developed a simplified analytical model for evaluating resistances of double bottoms under grounding scenarios, but their model verification was only for the distortion energy, which cannot adequately describe structural performance during shoal groundings in all aspects.

Jia Zeng et al (2014) proposed a theoretical model based on upper bound theorem for ship bottom plate tearing when the ship is subjected to a grounding over a cone-shaped rock. He developed a simplified kinematically admissible model to capture the major energy dissipation patterns which include friction, stretching, bending, and fracture.

Sun Bin et al (2016) gave an analytical method based on the plastic-elastic deformation mechanism to predict the ultimate strength of a ship hull after grounding event. Consideration was mostly on shoal seabed type which impact caused a predominant denting of the ship bottom structure. This denting has been known to threaten the global hull girder resistance, and can lead to hull collapse. The analytical formulation was validated using numerical simulations.

---

### 3.1.2. Numerical Approaches on Ship Grounding

Generally, because of advancements in computational power, FEA of large ship structures subjected to impacts have been made practicable.

The influence of the shape and size of the seabed during grounding was investigated by Hagbart and Amdahl (2007). By several FEM simulations, the resistance to penetration of the ship bottom was determined at various points of stranding and with different seabed topologies.

A verification of a simplified analytical method for the prediction of structural performance during ship grounding from numerical simulations was presented by Zhiqiang et al (2011). The simplified approach calculated resistance and distortion energy during shoal grounding accidents. Several numerical simulations were used to verify this analytical method.

FEA in crashworthiness analyses have recently been implemented by different researchers. For instance, the progressive failure of a double bottom was analysed by AbuBakar and Dow (2013) using the ABAQUS NLFE code. Different model extents were investigated in order to account for plastic deformation and the evolution of damage: an unstiffened plate, single stiffened panel and a panel with two stiffeners. Experimental data were available for result validation.

Calle et al (2017) made a comparison between scaled experiments and numerical analysis by taking into consideration ship grounding and collision. A series of grounding and collision tests of marine structures in reduced scale were reported and experimental tests were used to validate the FEA. Different numerical and experimental aspects such as failure criteria, weld joints, misalignment in tests and mechanical properties of the material were shown to have influence on ship grounding analyses. They concluded that the use of experimental tests continue to be one of the best ways of validating numerical results, because there still exist some discrepancies which are due to material characterisation, failure criteria, hydrodynamic effects, and to mention but a few.

Prabowo et al (2018) evaluated the structural crashworthiness and progressive failure of double hull tanker under raking grounding condition, and investigated the influence of geometric parameters to the structural behaviour by using the NLFEM on an idealised tanker structure. Furthermore, the seabed topology were modelled, and several locations were targeted for impact. The structural failure and damage extent were also investigated.

A benchmark study has also been carried out to compare the results obtained from FE analysis with experimental tests. This study checked for the influence of key parameters such as friction coefficient and failure strain values in the numerical simulations of grounding scenarios using a double bottom design. The numerical simulation results showed good agreement with experimental tests, and illustrated that NLFEA can be used to estimate the damage extent in grounding scenarios (Brubak et al, 2019).

---

## 3.2. Finite Element Model Set-Up

### 3.2.1. Material model

The elastic-plastic material model was applied for the ship, the material option adopted was the “PIECEWISE LINEAR PLASTICITY” which allows for the input of failure criteria in order to account for fracture (element deletion).

The material model adopted for the rock was the rigid body material model : “MAT\_RIGID”, because the rock is considered to be non-deformable. Although Young’s modulus, and Poisson’s ratio were applied, they are used for determining the sliding interface if there is a contact between the rock and the ship.

Mild steel was considered as the design material for the ship, the material properties are shown in table below.

**Table 7:** Material model properties

Material	$\sigma_Y$ (MPa)	$E_t$ (MPa)	$\nu$ (-)	$\rho$ (kg/m <sup>3</sup> )	$E$ (GPa)
Mild steel	240	1018	0.3	7850	210

From table 7,  $\sigma_Y$  is the yield stress,  $E_t$  is the tangential modulus for plastic hardening,  $\nu$  is the Poisson’s ratio,  $\rho$  is the mass density, and  $E$  is the Young’s modulus.

### 3.2.2. Material failure

In numerical analyses involving collision and grounding, one of the most vital parameter to be considered is the failure criterion as it has strong influence in the overall analyses in terms of fracture, energy absorption and deformation mode. The material failure criteria is normally coupled with the material model card in order to predict the onset of rupture. Various failure criteria have been summarised by Calle et al. In this project, the failure criteria adopted was the strain-based failure which is dependent on the mesh size as described in section 2.2.2. The Peschmann and Kulzep formulation gave the effective plastic strain at failure to be:

$$\varepsilon_f = 0.056 + 0.54 \frac{t}{l_e} \quad (16)$$

where  $t$  is the plate thickness,  $l_e$  is the characteristic finite element length. Elements are deleted once the effective plastic strain calculated at all integration points of the shell element has exceeded a given threshold ( $\varepsilon_f$ ) value. In order to use this formulation in the model, the following assumptions were made:

- The structural elements of the double bottom that were considered to fail due to excessive tension (raking) or compression (stranding) include: the outer shell, floors and the inner shell.

- The girder is assumed not to fail during both stranding and raking processes, but may undergo compression during standing, therefore the effective plastic strain was assigned zero in the material card.

With these assumptions, the effective failure strains were calculated and are shown in the table 8. It is important to note that the mesh size depicted in the table represents the fine mesh in the areas of possible impact. A description with labels about the model structural members will be shown in section 3.2.3.

**Table 8:** Material effective plastic strain values for ship structural members

Part No.	member	thickness [mm]	mesh size [mm]	$l_e$ [mm]	$\varepsilon_f$ [-]
1	outer shell	15	30	42.4	0.247
2	floors	15	30	42.4	0.247
3	girders	20	30	42.4	0.0
4	inner shell	10	30	42.4	0.183

### 3.2.3. Model extent

#### Double bottom passenger ship

The idealised ship was modelled based on the Floodstand passenger ship provided by Meyer Werft shipyard in the framework of FLARE project. As grounding incidents are known to occur on the bottom part of a ship, the finite element model was focused on the double bottom structure. Furthermore, the structural members were also idealised using the shell elements. The modelling was done using the MSC Patran/Nastran software, and the mesh geometry was imported to LS-DYNA pre/post V4.3.12 where boundary conditions were imposed and keyword file generated.

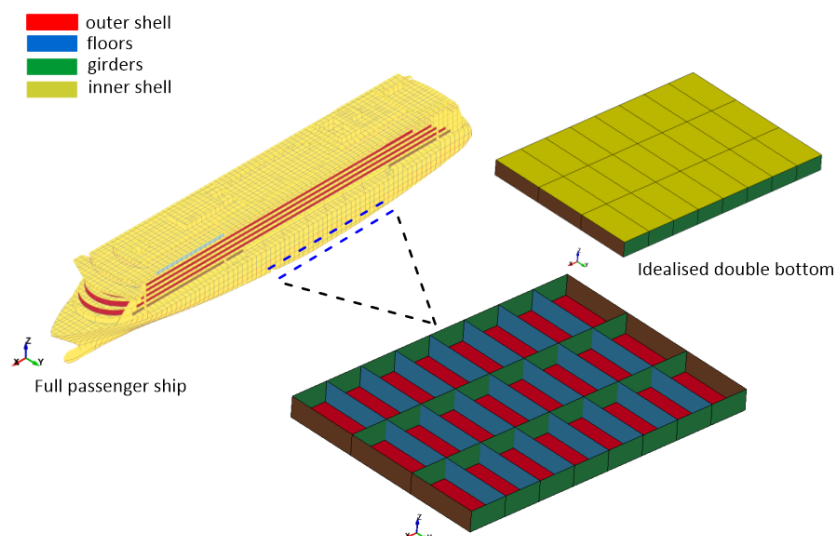


**Figure 39:** Idealised geometry of the double bottom for grounding analysis

The dimensions of the idealised model is 24 metres by 17.1 metres with the particulars of the structural members described in table 9.

**Table 9:** Dimensions of double bottom structural members

Member	Length [m]	height [m]	Spacing
floor	17.1	1.6	3 m between two floors
girder	24	1.6	5.7 m between two girders

### Rock geometry

The seabed was already modelled by another student as a conical rock, with an half angle  $\theta$  of  $37^\circ$ , approximate height  $h$  of 3.5 metres and an approximate width  $w$  of 5.1 metres. This geometry will serve the purpose of the rock in a collision scenario. The geometry is shown in figure 40.

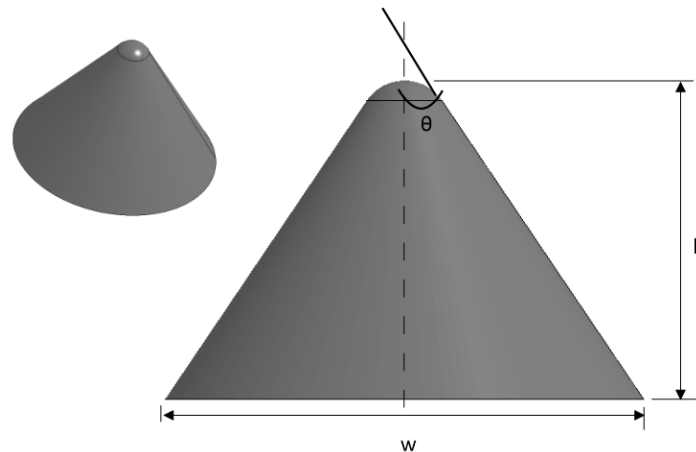


**Figure 40:** Seabed rock geometry

#### 3.2.4. Finite element model description

For numerical analyses, the LS-DYNA nonlinear explicit code was implemented together with MCOL subroutine (which will explained in subsection 3.3.2) to account for external hydrodynamic forces. The version utilised was the LS-DYNA R V4.3.12 64bit.

#### The element characteristic length

Generally, FE analyses are approximate solutions, and the accuracy of the analysis depends on numerous factors such as mesh density. It has been known that mesh density plays a vital role in capturing material failure and deformation mode.

Mesh sensitivity analyses had already been carried out by a Ph.D. student in ICAM, and the optimum mesh size for the impacting surfaces was given as 30 mm. Furthermore, it was advised that for better results, one should maintain an element aspect ratio ( $l/w$ )

close to unity and maximum of 5. This advice was followed especially in the surrounding region of impact. Mesh sizes were gradually increased farther away from the impacting zones (see figure 41) in order to reduce the computational costs, a good distribution of mesh and better mesh quality in terms of taper ratio, Jacobian ratio, skew angle, etc.

### **Element type**

The Belytshko Lin-Tsay shell element type was utilised as it is more computationally efficient with a reduced integration formulation than the Hughes-Liu shell elements. Five integration points through the shell element thickness were implemented so as to capture better plastic variation through the shell thickness. This element type was applied to the double bottom structural members: the outer shell, floors, girders and the inner shell.

### **Parts**

In LS-DYNA, the PART cards are used to define material information, hourglass type, and section information. This helps in grouping structural components under the same part. For instance each structural member had its part defined because of same properties, that is, all deformable floors belong to a part, all deformable girders belong to a part, and so on. Furthermore, the SET\_PART card combines all the parts that belongs to the ship by assessing their part identification numbers.

Additionally, there exist the PART\_INERTIA card which allows the definition of inertia properties, true mass, initial positions, and velocities. The PART\_INERTIA card is used to model the remaining part of the ship and it is applicable to rigid body material (which will be discussed further in section 3.3).

### **Boundary conditions**

For the double bottom, the boundary condition was imposed using the set-node-list option on the two extreme girders as shown in the figure below. For the rock, the BOUNDARY\_SPC (Single Point Constraint) LS-DYNA card was imposed to restrict all translations and rotations of the rock.

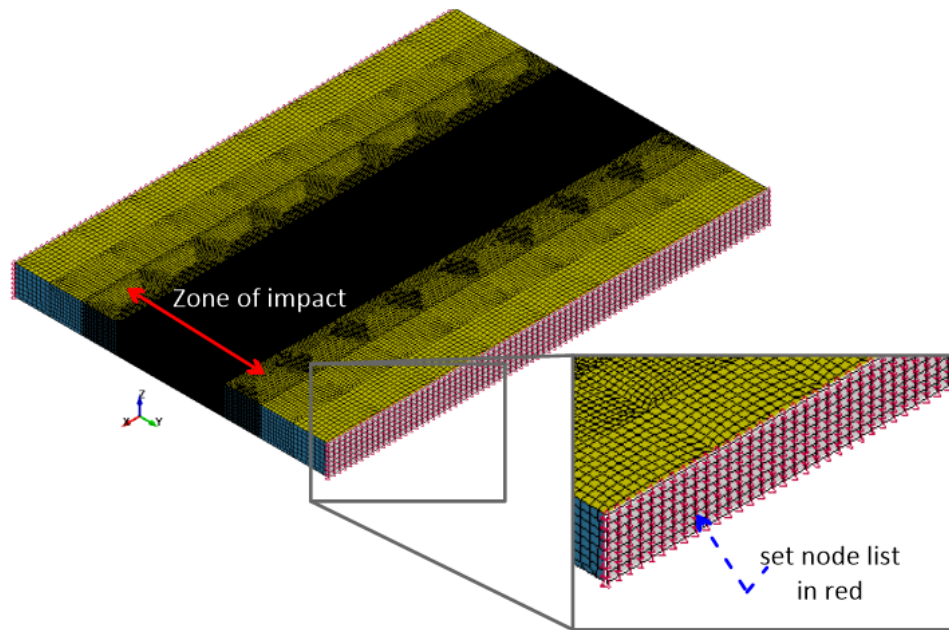


**Figure 41:** Meshed double bottom

### Contact modelling

According to Paik (2017), thin-walled structural components can undergo contact between each other during crushing, therefore it is of crucial importance to model contact problems properly. Paik considered two contact problems: the general contact which is affected by surfaces between different structural members, and the self-contact which is affected by structural components themselves due to crushing. Paik further showed that the effect of overlapping contacted surface can be of significance in terms of energy absorption capabilities and resultant forces. The figures below give description of the importance of proper contact modelling.

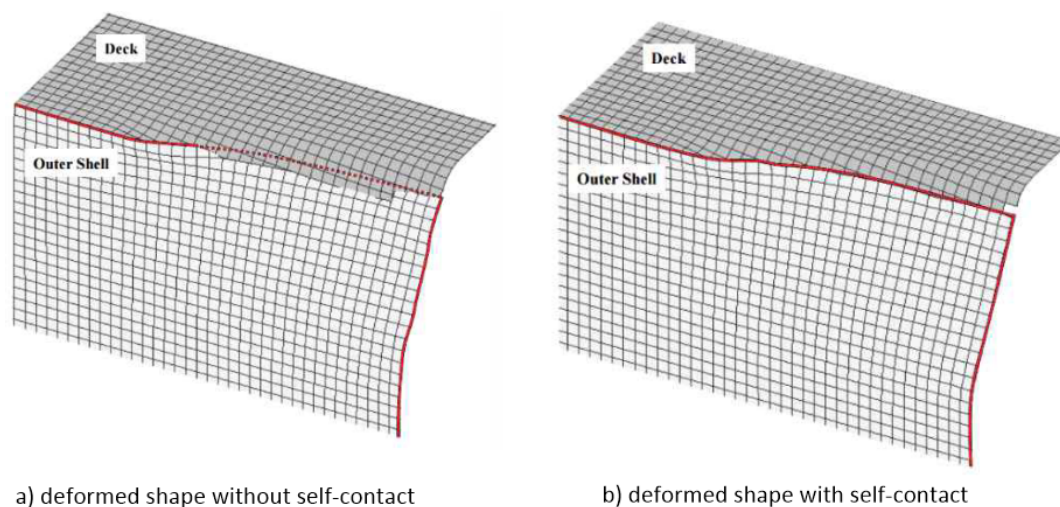


**Figure 42:** Example of structural crashworthiness with or without self-contact phenomenon in terms of deformed shape. From

In this study, two contact modelling techniques were implemented:

- `CONTACT_AUTOMATIC_GENERAL` this is to create an auto contact between the ship parts. For instance contact between the outer shell and the floors. This contact model also checks for edge-to-edge penetration along the length of the element.
- `CONTACT_AUTOMATIC_SURFACE_TO_SURFACE` this is to create contact between the ship structure and the rock. Care was taken to ensure that there were no initial penetration between the outer shell and the rock.

For confirmation of the contact model, some test simulations were ran to ensure there was no contact detection issues.

For friction effect modelling, normally it is advised to perform some sensitivity analyses on the value of friction coefficient to utilise, because the higher the friction coefficient, the higher the resistance and vice versa. As the resistance may change because of different values of the friction coefficient, similarly, the deformation mode may change slightly as well. In this study, the static and dynamic friction coefficient were assumed as 0.3 for all cases.

### 3.3. External Dynamics Due to Hydrodynamic Forces

During grounding events, vessels are navigating on the sea and therefore not fixed in any direction but are free to move even after impact. The importance of modelling the water effect has given a rise to recent researches, because most researchers have focused on fixing the direction of the vessel and allowing the rock to make the impact, which does not represent the reality. The effect of sea water especially the hydrodynamic forces should be taken into account, and in this study we are going to observe the role played by the hydrostatic restoring forces. Also, the added mass effect of the surrounding water on the ship's motion can affect the total kinetic energy of the vessel and part of the kinetic energy can be consumed for the movement of the ship in the ocean.

In the next section, a brief description of finite element methodology will be described, followed by the modelling of the surrounding water using the MCOL functionality.

#### 3.3.1. Explicit Finite Element Analysis

Nowadays, because of the increase in computational power FE analysis can be implemented in various impact problems including grounding. Most researchers now make use of this approach to investigate various scenarios and parameters involving grounding analyses. Because of the dynamic nature of these events as the bodies are subjected to high time-dependent motions, it is required to make use of explicit solutions

The governing equation of motion for dynamic analysis is given as:

$$[M] \{x''(t)\} + [C] \{x'(t)\} + [K] \{x(t)\} = \{F(t)\} \quad (17)$$

Where  $[M]$  is the structural mass matrix,  $[C]$  is the damping matrix,  $[K]$  is the stiffness matrix, and  $\{F(t)\}$  is the external force vector.  $x(t)$ ,  $x'(t)$  and  $x''(t)$  are the unknown nodal vectorial displacement, velocity and acceleration of the system respectively.

To solve the equation 17 above, Le Sourne (2015) used the Newmark direct integration method as it solves the solution at time step  $t_{n+1} = t_n + \Delta t$  when the time step  $t_n$  is known. Taylor's series are used to approximate the displacement and velocity at the next time step  $t_{n+1}$ . The initial conditions are given as  $x(0) = x_0$  and  $\dot{x}(0) = \dot{x}_0$ . With the Taylor's series corresponding motions can be solved.

$$M[\ddot{x}_{n+1}] + [C]\dot{x}_{n+1} + [K]x_{n+1} = F_{n+1} \quad (18)$$

$$x_{n+1} = x_n + \Delta t \dot{x}_n + \frac{\Delta t^2}{2} [(1 - 2\beta)\ddot{x}_n + 2\beta\ddot{x}_{n+1}] \quad (19)$$

$$\dot{x}_{n+1} = \dot{x}_n + \Delta t [(1 - \gamma)\ddot{x}_n + \gamma\ddot{x}_{n+1}] \quad (20)$$

$\beta$  and  $\gamma$  are the Newmark's constant. When  $\beta$  is zero, the integration scheme is said to be explicit, because the state of the system in the current time step can be calculated with respect to the previous step, and when  $\beta$  is not equal to zero the solution is said to be implicit.

Generally, the explicit solution is less costly in terms of the computation time, but it is not unconditionally stable, because it requires a very small time step  $\Delta t$  which must be less than a critical value. The time step must be less than the length of time it takes a signal travelling at the speed of sound in the material to transverse the distance between the node points. A critical time step is given by:

$$\Delta t_{\text{critical}} \leq \alpha \left( \frac{l_e}{c_e} \right) = \frac{l_e}{\sqrt{\frac{E}{\rho}}} \quad (21)$$

where  $\Delta t_{\text{critical}}$  is the critical elemental time step,  $\alpha$  is a safety factor,  $l_e$  is the characteristic element length,  $c_e$  is the wave propagated speed of sound for a specific material,  $E$  is the Young's modulus, and  $\rho$  is the mass density.

### 3.3.2. MCOL Description – Combining Ls-DYNA and MCOL

In this study, MCOL functionality was used together with the LS-DYNA explicit NLFE code in order to simulate ship grounding by taking into account the effects of external

hydrodynamic forces. Upon using the LSDYNA/MCOL tool for the ship grounding analyses, the resultant forces and moments are calculated at each time step during the simulation in LS-DYNA, and with these values, the new position, velocity, and acceleration of the ship are then updated in MCOL, and transmitted back to LS-DYNA for the next integration time step. MCOL uses the external rigid body dynamics to account for the ship motion using the equation below (Le Sourne et al., 2003):

$$[M + M_\infty] \ddot{x} + G\dot{x} = F_W(x) + F_H(x) + F_V(x) + F_C \quad (22)$$

where  $M$  is the structural mass matrix,  $M_\infty$  is the added mass matrix,  $x$  is the earth-fixed position of the centre of mass of the ship,  $G$  is the gyroscopic matrix,  $F_W$  is the wave damping force vector,  $F_H$  is the hydrostatic restoring force vector,  $F_V$  is the viscous force vector and  $F_C$  is the contact force vector. The details for the calculation of  $G$ ,  $F_W$ ,  $F_H$  and  $F_V$  can be found in (Le Sourne et al., 2001).

LS-DYNA/MCOL solutions have been validated with a real ship which had undergone a collision. The figure 43 below gives an illustration of how clearly the results from MCOL imitated a collision after the simulation result was superposed on the photo of the real damaged ship hull. LS-DYNA/MCOL requires fine mesh to obtain reliable results, this makes the computation time longer. This is also another motivation for this study, in order to provide a validation base for the FLARE solver which incorporates MCOL using super-element methods, and thus computation time will be drastically reduced.



**Figure 43:** Comparison of LS-DYNA/MCOL simulation with real ship. (From: Le Sourne et al., 2003)

Six degrees of freedom are used to describe the motion of rigid bodies, and their dynamic motion equations are normally separated into translational and rotational motion. As stated earlier, MCOL makes use of rigid body dynamics. For each ship considered, MCOL uses two frames of references. The first one is a body fixed frame with its origin being the centre of mass of the ship with an x-axis along the forward axis of the vessel, a starboard

y-axis, and a downward z-axis. The second frame of reference is an earth-fixed frame defined as the initial position of the body-fixed frame as shown in the figure below. The ships motion is defined by its roll, pitch and yaw and by translation of its centre of mass from its initial position (Le Sourne, 2012).

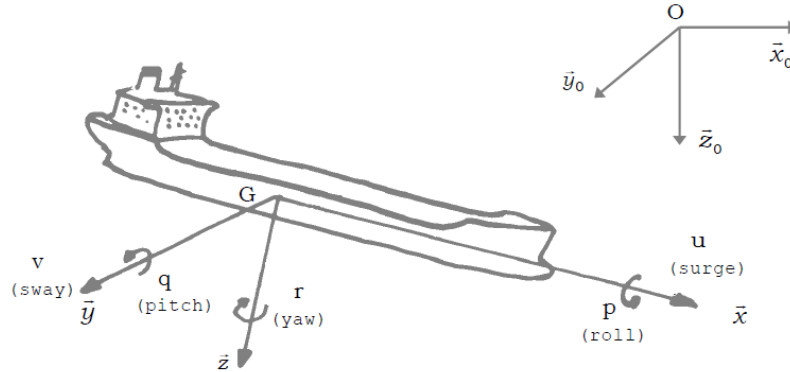


**Figure 44:** Body-fixed and earth-fixed frames of references. From

To make the link between LS-DYNA and MCOL solvers, the BOUNDARY\_MCOL card was inserted in the Ls-Dyna keyword datafile. The cards are shown below:

```
*BOUNDARY_MCOL
$  NMCOL|  MXSTEP|  ENDTMCOL|  TSUBC|  PRMTCOL|
    1  2000000  0.0  0.2  5.000E-03
$  rbmcol|  mcolfile|
    5  Ship_1.mco
$
```

**Figure 45:** Coupling card for LS-DYNA/MCOL simulation

The figure 45 above gives the control parameters relative to the LS-DYNA coupling where;

- NMCOL is the number of ships considered
- MXSTEP is the maximum time step in MCOL calculation
- ENDTMCOL is the MCOL termination time or LS-DYNA termination time if zero is inserted
- TSUBC is the time interval for MCOL subcycling. Subcycling is a technique introduced to reduce the computation time by updating the hydrodynamic forces with a different time step than the MCOL calling frequency.
- RBMCOL represents the rigid ship part identification. This means the LS-DYNA rigid body material assignment for the ship. As explained earlier, the idealised model was just a section of the double bottom, but in order to take into account the remaining ship sections, rigid body was implemented using the PART\_INERTIA card.

- MCOLFILE this is the input file name for the ship in investigation. The input file is an mco extension file that contains the mass matrix of the ship, hydrostatic restoring matrix, buoyancy reference parameters, added mass matrix, viscous damping, convergence parameters, wave damping matrixes and the modal matrixes. Normally, these parameters are obtained using hydrodynamic/seakeeping software such as the ARGOS or HydroStar.

In order to take into account the other parts of the ship using the PART\_INERTIA cards, two passenger ships parameters were considered with their MCOL data file. The ship particulars are tabulated below:

**Table 10:** Ships to be considered for LS-DYNA/MCOL grounding simulations

Name	LOA[m]	Beam[m]	$\Delta$ [tons]	$I_{xx}$ [ $kgm^2$ ]	$I_{yy}$ [ $kgm^2$ ]	$I_{zz}$ [ $kgm^2$ ]
Floodstand	241	32	33923	4.10E+09	1.22E+11	1.26E+11
Ship_1	153	20	5880	2.56E+08	6.38E+09	4.23E+09

The reason for selecting these two ships was to investigate their different behaviours when a grounding event occur as they represent a very large ship and a smaller ship respectively. The effects of external hydrodynamic forces on both ships will be examined. It is important to note that the length and beam of Ship\_1 were not readily available. Therefore, similar passenger ships with the same displacement range were used as indicators for these two parameters only. The purpose of requiring the length of the ship is to investigate the pitch motions and this will be explained better in section 3.7.1.

### PART\_INERTIA

The inputs to this keyword that take into consideration the rigid part of the ship which is to be used for the MCOL program are given below;

```
*PART_INERTIA
Ship Rigid Part
$#      pid      secid      mid      eosid      hgid      grav      adpopt      tmid
        5         5         5         0         0         0         0         0
$      Xc|      Yc|      Zc|      tm|      ircs|      nodeid|
        0.0      0.0      5.0  5.88E+06      1
$      Ixx|      Ixy|      Ixz|      Iyy|      Iyz|      Izz|
        2.56E+08      0.0      0.0  6.38E+09      0.0  4.23E+09
$      VTX|      VTY|      VTZ|      VRX|      VRY|      VRZ|
        1.5      0.0      -1.5      0.0      0.0      0.0
$      XL|      YL|      ZL|      XLIP|      YLIP|      ZLIP|      CID|
        1.5      0.0      0.0      0.0      -1.0      0.0
```

**Figure 46:** PART\_INERTIA card for MCOL rigid body

This option allows the inertial conditions and inertial properties to be defined rather than calculated from the finite element mesh, and this applies to the remaining part of the ship which is considered as a rigid body.

From figure 46, the important variables to point out are:

- $pid$  which is the part identification: a unique number assigned to each ship part
- $secid$  which is the section identification: a unique number that defines the section parameters such as element formulation, number of integration points, element thickness, etc.
- $mid$  is the material identification: a unique number for material type which must have already be defined.
- $X_c$ ,  $Y_c$ , and  $Z_c$  are the global x, y, and z-coordinate of the centre of mass of the ship in metres.
- $tm$  is the translational mass of the rigid body in kilogram.
- $I_{xx}$ ,  $I_{yy}$ , and  $I_{zz}$  are the components of the inertia tensors for the rigid body in  $kg.m^2$
- $VT_x$  and  $VT_z$  are the initial translational velocities in  $m/s$  of the rigid body in global x and z directions respectively.

### 3.4. Pure Raking Grounding Simulations

As mentioned earlier in section 3.1, raking grounding involves the mechanics of horizontal action of the ship. This means only horizontal (surge) velocity of the ship will be taken into account during the grounding event. In this section, the following pure raking scenarios will be investigated for Ship\_1:

- Raking with  $V_x = 2$  m/s
- Raking with  $V_x = 4$  m/s

In these two raking scenarios, location of impact will be in-between two girders as shown in the figure 47. Furthermore, for considering the remaining part of the ship, the two extreme girders will be taken as the rigid part.

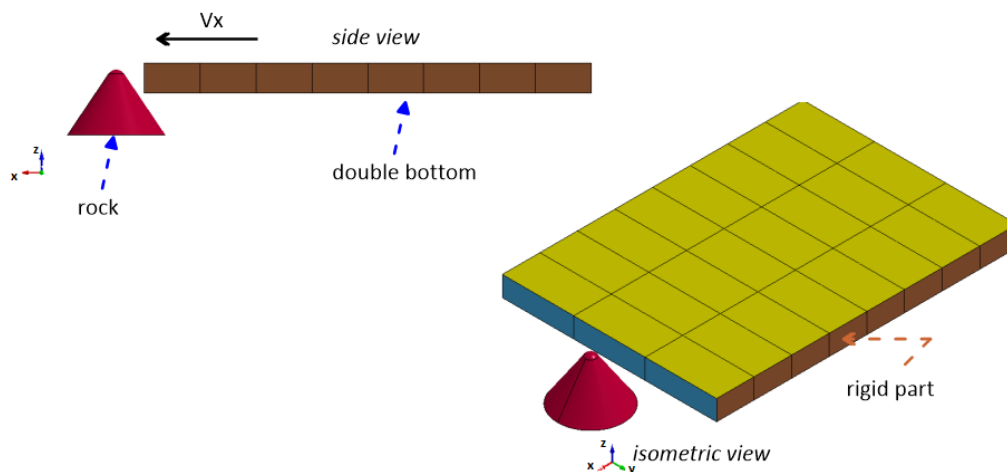


**Figure 47:** Set-up for pure raking simulations

In the PART\_INERTIA card, the mass and inertia that should be inserted are the inertia components of the rigid part which are obtained by subtracting the mass and inertia of the modelled (deformable) bottom from the mass and inertia of the whole ship. In this simulation set-up, for the longitudinal position it was assumed that the centre of the idealised model (along X axis) is located exactly below the ship's centre of gravity, and regarding the transverse coordinate,  $Y_c=0$ .

An initial velocity was prescribed for the deformable parts of the ship by inserting the corresponding horizontal velocities of investigation using the INITIAL\_VELOCITY\_GENERATION card. Similarly, the same initial velocity for the rigid part of the ship was prescribed using the PART\_INERTIA card.

### 3.4.1. Case 1: Raking with $V_x = 2\text{ m/s}$

The results for raking grounding simulation with a velocity of 2 m/s and simulation time of 15 seconds are given below:

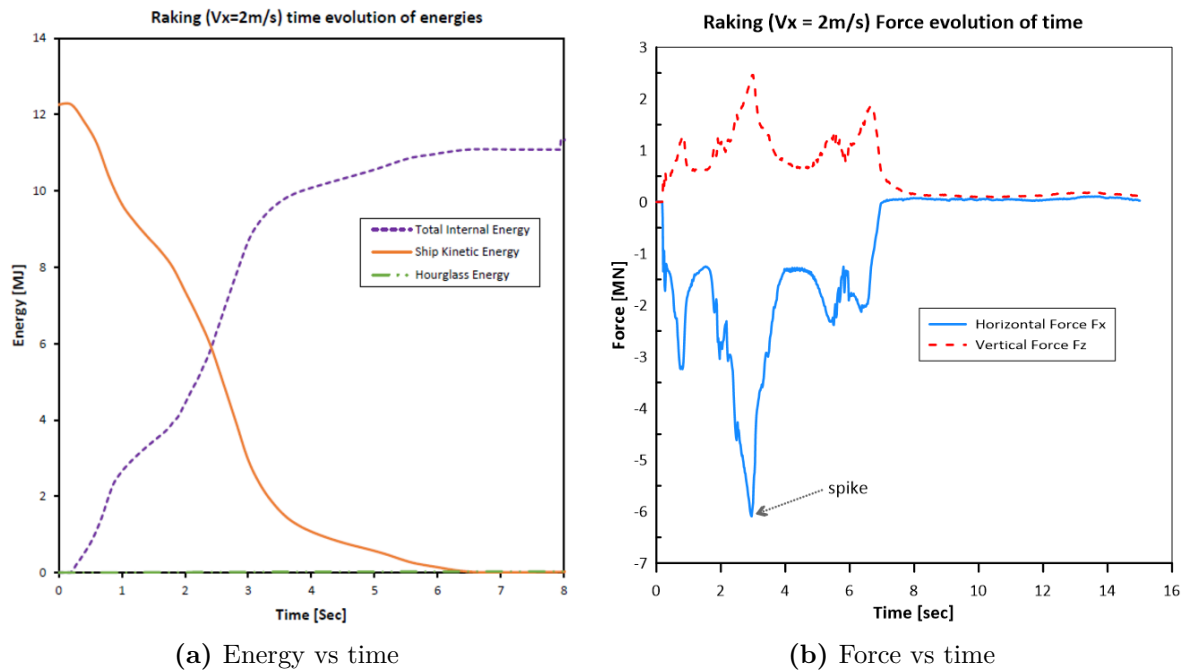


**Figure 48:** Time evolution of energies and force plots for Raking (2 m/s) grounding simulation

From figure 48 it can be observed that with a simulation time of 15 seconds and an initial horizontal velocity of 2 m/s, the ship came to halt at about 7 seconds after breaching two transverse floors. Based on the utilisation of the reduced integration scheme, it was necessary to check for the hourglass effect on the energy. From figure 48a, it can be seen that the energy spent to control hourglassing is reasonable as it is far lower than the required maximum 5% of peak total internal energy.

Progressive failure can also be possibly predicted by accessing the crushing force which is the structural resistance as shown in figure 48b. The spikes indicated in the figure illustrate the crushing of the transverse floors. These spikes acts as high resistance (shock) to the structure in experiencing loads at short time. The height of the spike or the increase in resistance force is also influenced by the damaged volume of the structural member as can be observed in figure 49, because the damaged members volume increased as the ship continues to move until it gradually loses all velocity.

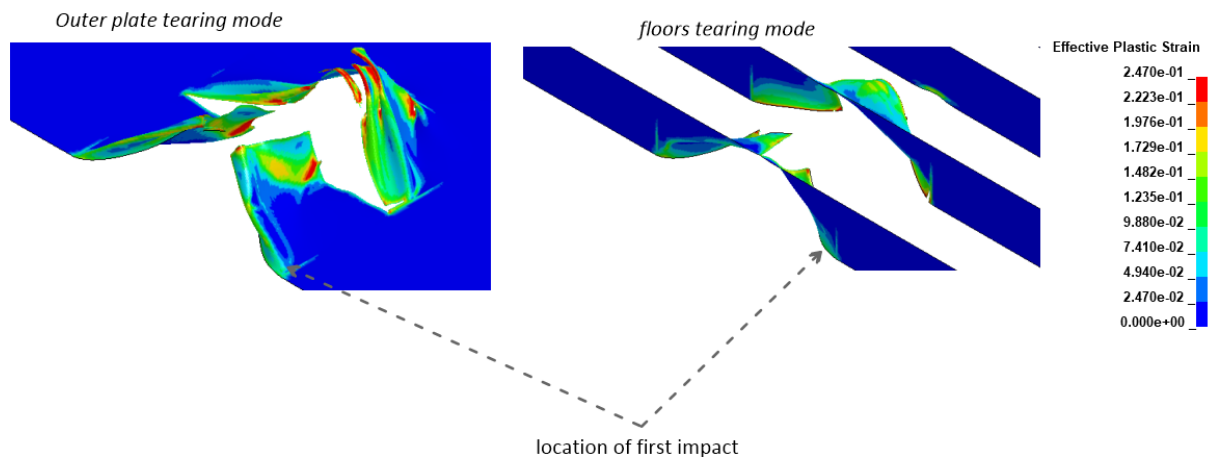


**Figure 49:** Failure modes of the double bottom structure for raking (2m/s) grounding simulation

The dominating failure mode in this raking case is shown in the figure 49, the location of the first impact was between two longitudinal girders. Due to the initial velocity of the ship, only two transverse floors were breached together with their corresponding outer shell sections. It is important to note that the shape of the rock also contributed to this failure mode, as the rock has a large impacting surface together with the half angle of  $37^\circ$  which means that the rock is not very sharp.

From the figure, we can observe the tearing of the outer shell at first impact, then successively there was crushing and folding of the outer shell which increased the volume of destroyed members thereby giving a rise to the structural resistance and internal energy. Similarly the floors experienced cutting with a thin shell layer holding them from tearing apart.

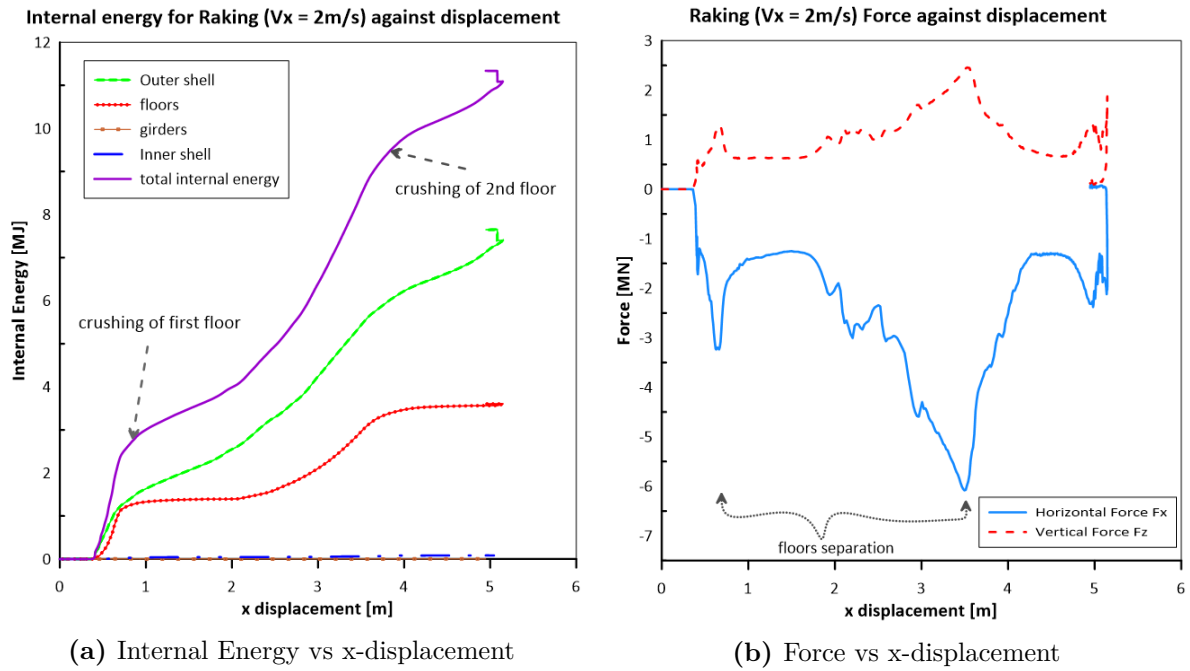


**Figure 50:** Internal Energy and force plots versus x-displacement for Raking (2 m/s) grounding simulation

The contributions of various structural members to the total energy absorption is presented in figure 50a, it can be observed that the outer shell contributed the highest with about 67% of the total internal energy. This is due to the high volume of the crushed outer shell plating, and the least were the inner shell plating and the girders because there was little or no direct impact on them. The areas of total crushing of the first and second transverse floor were also depicted as the hilly points of the total internal energy curve, while the valley areas should represent the outer shell tearing. This also explains why the outer shell had more contribution to the total internal energy than any other structural members in this case of raking.

It has been observed that raking grounding cases led to remarkable fluctuations on the longitudinal and vertical direction as can be seen in figure 50b  $F_x$  and  $F_z$  respectively. These forces correspond to the action of the rock over the ship, therefore  $F_x$  is negative and  $F_z$  positive. From same figure, it can also be seen that the distances between spikes are the separation between two transverse floors. The maximum resistance force for  $F_x$  was obtained at about 3.5 metres penetration with a structural resistance of about -6 MN. This is due to the dominating direction (x-direction) of the raking scenario.

### 3.4.2. Case 2: Raking with $V_x = 4\text{ m/s}$

The results for raking grounding simulation with a velocity of 4 m/s and simulation time of 10 seconds are given below:

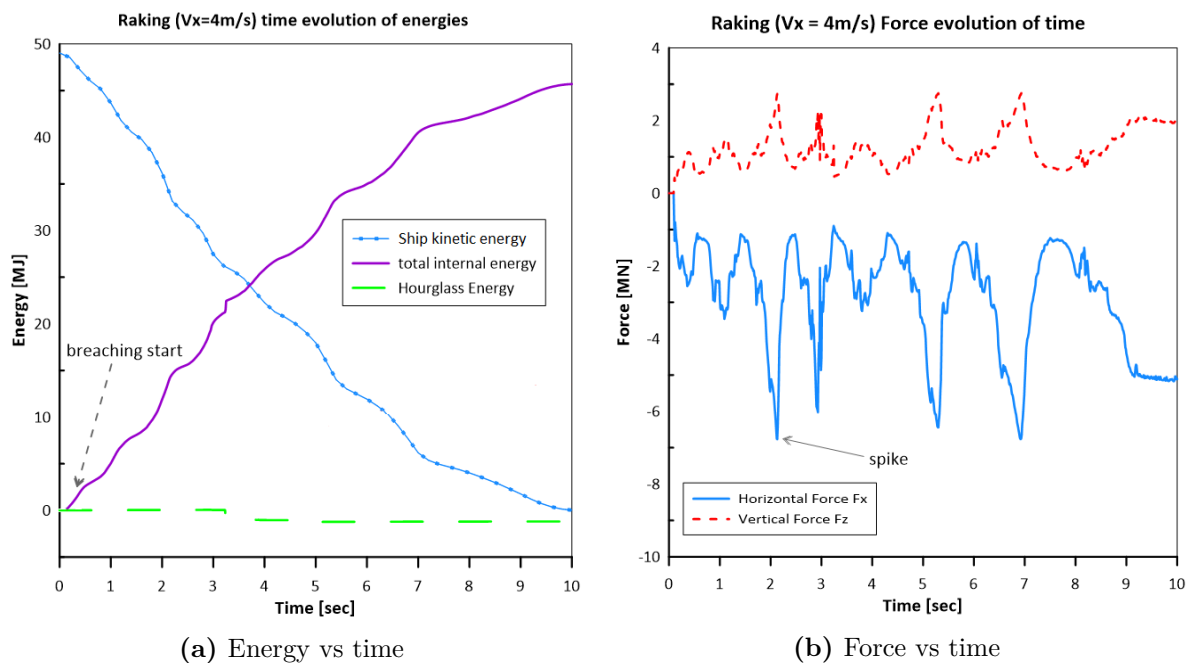


**Figure 51:** Time evolution of energies and force plots for Raking (4 m/s) grounding simulation

With the doubling of the initial velocity to 4 m/s there was drastic changes in the behaviour of the double bottom in terms of the increase in the kinetic energy, internal energy, structural resistance and the breach length. The time evolution of energies and structural resistance are depicted in figure 51. Similarly the spikes on figure 51b are related to the total crushing of the transverse floors. The horizontal force was very dominant with a maximum of about -6.8 MN, and the ship came to halt at about 9.3 seconds after breaching eight transverse floors and exhausting all initial kinetic energy.

Furthermore, the hourglass energy in this case was negligible due to the far lower energy necessary to check for the hourglass effect on the energy. The deformation modes are illustrated in the figure 52.

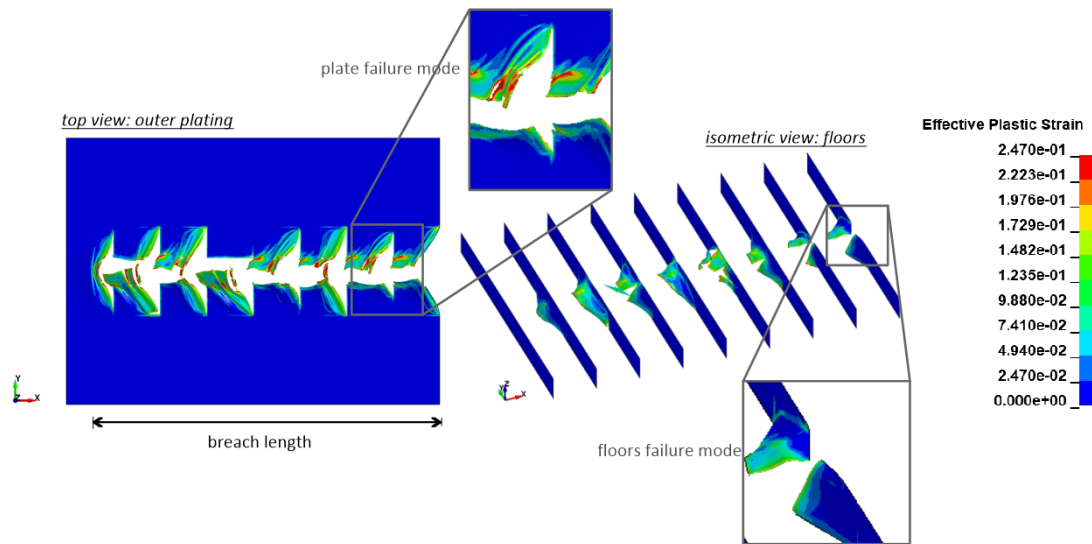
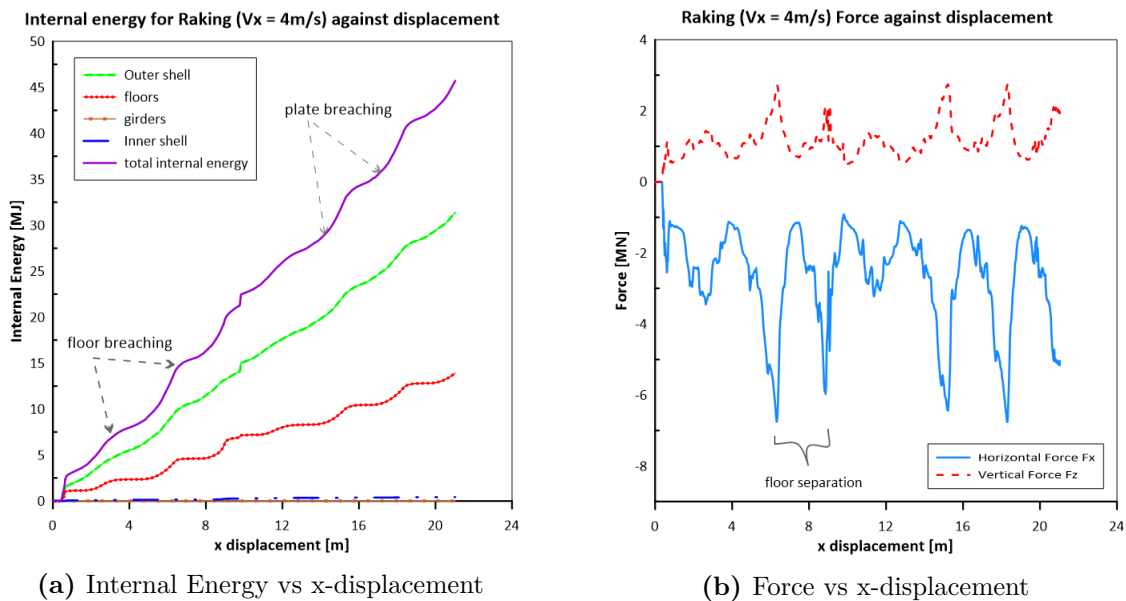


**Figure 52:** Failure modes of the double bottom structure for raking (4m/s) grounding simulation

As expected, with the 4 m/s horizontal initial velocity, the double bottom had a larger breach length of about 22 metres. Due to the nature of the rock and the speed of impact, it can be observed that the first two floors were torn into two at the point of impact, and consecutively there was stretching and cutting of the remaining six floors. The major failure mode for the outer shell plating is tearing which was followed by folding and crushing of the plate. During the raking scenario, the folding of the outer plating as the ships runs over the rock gradually increased the volume of the structural members required to resist the penetration at a point in time, and this also contributed to the increase in structural resistance at that particular period before complete crushing is achieved.



(a) Internal Energy vs x-displacement

(b) Force vs x-displacement

**Figure 53:** Internal Energy and force versus displacement plots for Raking (4 m/s) grounding simulation

Similarly, the zones showing the floors and plate breaching points are represented in figure 53. The major contributors to the total internal energy were the outer shell which contributed about 69% of the total internal energy and the floors. This is evident because they were the main structural members that experienced the raking event directly. Also, the difference between two spikes in the force displacement plot represents roughly the gap between two floors. These spikes were due to the increase in contact force which acted as shock to the structure when the transverse floors were crushed.

A summary of the pure raking grounding scenario is tabulated below:

**Table 11:** Pure raking comparison

Raking case:	2 m/s	4m/s
Initial Ship K.E [MJ]	12.3	49
Max. resistance force, $F_x$ [MN]	-6.1	-6.8
Breach length [m]	6	22
Time for ship halt [sec]	7	9.3

**Table 12:** Pure raking Internal energy comparison

Raking case:	2 m/s		4m/s	
Max. total internal energy [MJ]	11.3	%I.E	45.7	%I.E
Outer shell [MJ]	7.65	67.70	31.38	68.67
Floors [MJ]	3.61	31.95	13.90	30.42
Girders [MJ]	0.00	0.00	0.01	0.00
Inner shell [MJ]	0.08	0.71	0.42	0.92

From the table 12, we can see that for the pure raking grounding scenario in-between two girders, the major contributors to the deformation energy were the outer shell plating and the floors. This was also due to the positioning of the rock with respect to the bottom girders.

Furthermore, it is also important to point out the role played by the initial velocity in generating the breach on the double bottom which is evident by the increase in breach length from about 6 metres to 22 metres when the initial velocity was doubled.

### 3.5. Pure Stranding Simulations

Stranding is a grounding phenomena which involves the vertical action of the ship over an obstruction. It is important to note that all simulations performed for stranding were ran in order to have some reference solutions for the super-element code validation.

For pure stranding, only vertical (heave) velocity of the ship will be taken into consideration during the grounding event. In this section, the following scenarios will be investigated on Ship\_1:

- full stranding on plate with  $V_z = -3.0$  m/s
- medium stranding on plate with  $V_z = -1.5$  m/s
- stranding on girder with  $V_z = -2.0$  m/s
- stranding on intersection  $V_z = -1.5$  m/s

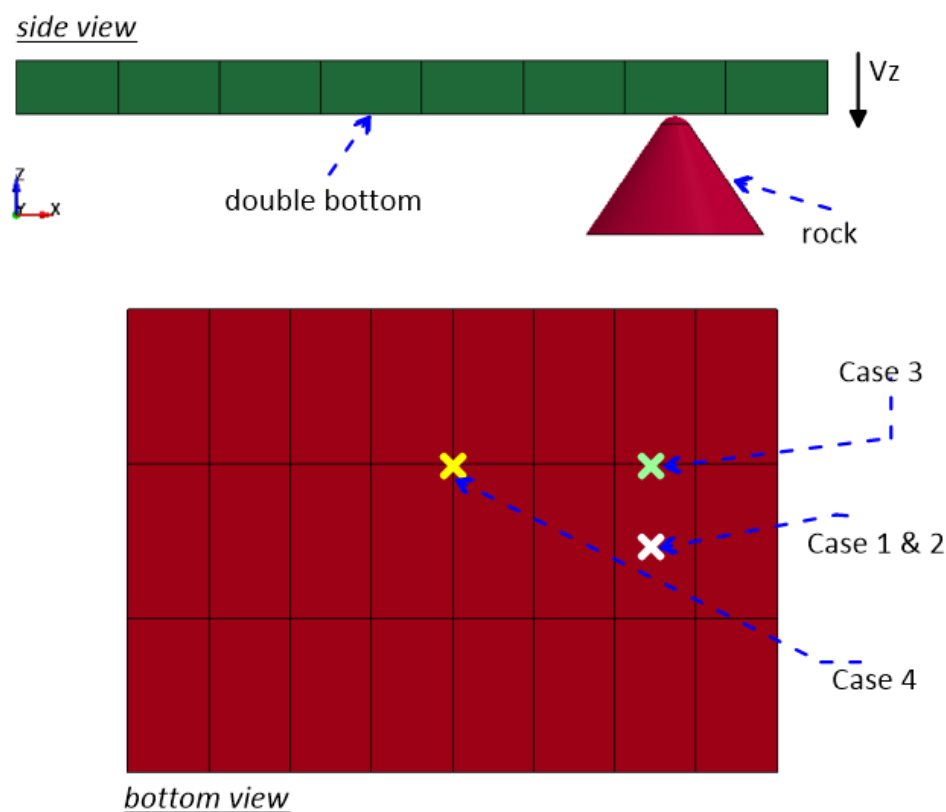


**Figure 54:** Set-up for pure stranding simulation with impact points

In these pure stranding simulations, figure 54 gives an illustration of the scenarios considered in this section. The two extreme longitudinal girders were taken as the rigid part of the ship in order to account for the remaining ship sections. Furthermore, an initial velocity was prescribed for the deformable parts and rigid part of the ship by inserting the corresponding vertical velocities of investigation using the INITIAL\_VELOCITY\_GENERATION and PART\_INERTIA cards respectively. It is important to note that the velocities in both cards should be the same for consistency reasons.

### 3.5.1. Case 1: full stranding on plate with $V_z = -3.0$ m/s

For this stranding scenario, the point of impact was the outer shell plating located in-between two longitudinal girders.

The results for this stranding scenario with a vertical velocity of -3.0 m/s and simulation time of 4 seconds are given below;

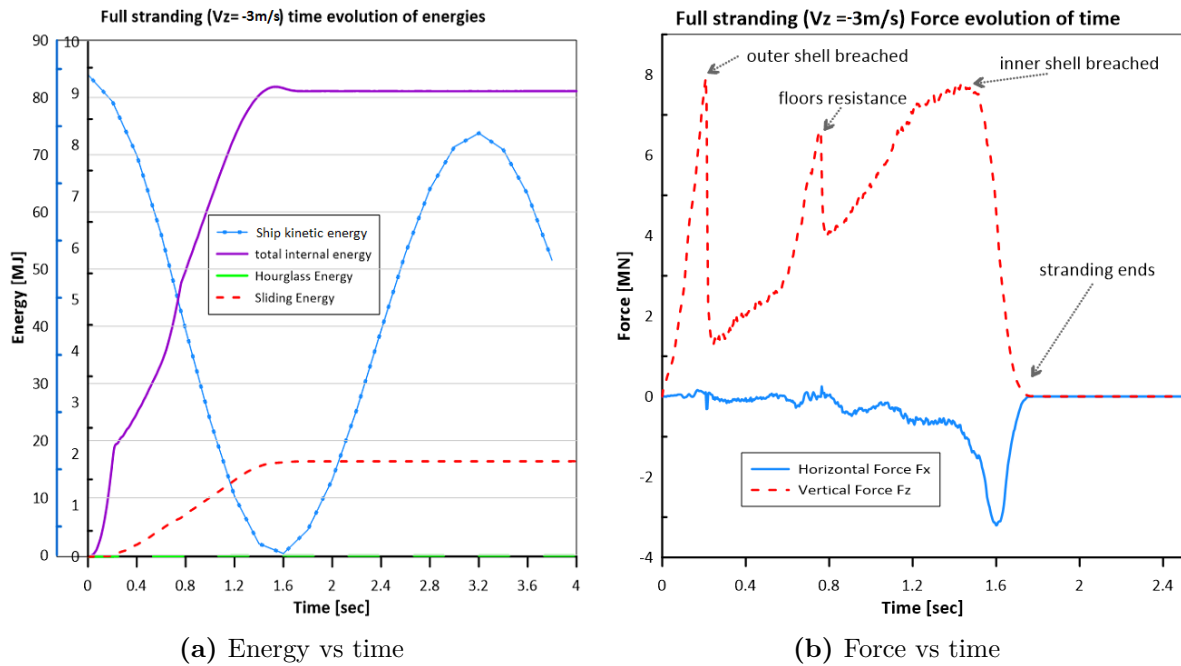


**Figure 55:** Energy and force plots vs. time for full stranding (-3 m/s) grounding simulation

In the figure 55a, the kinetic energy of the ship obtained from MCOL was plotted on a different vertical secondary axis coloured in blue for better representation. The other energies maintained same vertical axis in black.

At about 1.64 seconds, there was no more change in internal energy as the stranding ended at this point in time, and the kinetic energy was almost exhausted. After the stranding, due to restoration force of buoyancy, the ship experienced an upward movement which caused it to pick up some additional kinetic energy. Furthermore, the hourglass energy had negligible effect on the total energy.

The force versus time plot (figure 55b) also illustrates the distribution of the contact force experienced by different structural members. Although two directions of forces were investigated, the dominating was the vertical force ( $F_z$ ) which is expected for stranding. A maximum structural resistance of about 7.9 MN was attained during the complete breaching of the outer shell plating. As stranding continued, the rock got it contact with the two surrounding transverse floors which acted as further resistance and therefore leading to the second peak. The third peak was attained during the complete breaching of the surrounding inner shell plating at about 1.6 seconds.

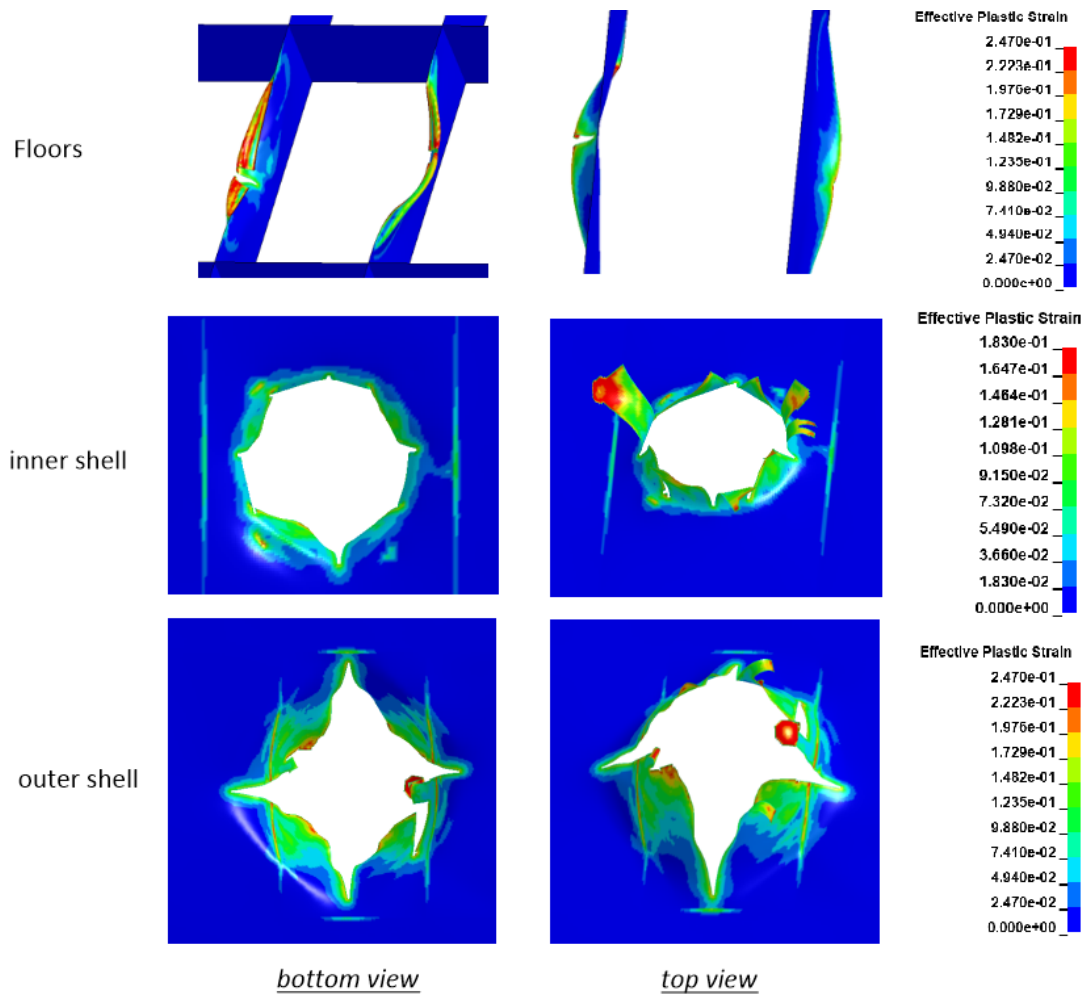


**Figure 56:** Deformation/Failure modes of structural members during full stranding

The failure modes of the structural members of the double bottom are represented in the figure 56. The contributing floors were the two surrounding transverse floors at the point of impact. From the first row of figure 56, the bottom view and the top view of the crushed floors were shown. It can be observed that there was folding, bending and tearing of the floors as the surface of the rock crushed through the double bottom and making contact with the floors. The inner shell plating was penetrated as shown in the second row, it can be observed that the inner shell experienced some straining before finally tearing due to excessive compression. Similarly, the outer shell plating failed with a dominating failure mode of tearing which was initiated at different points of propagation at the region of plate impact.

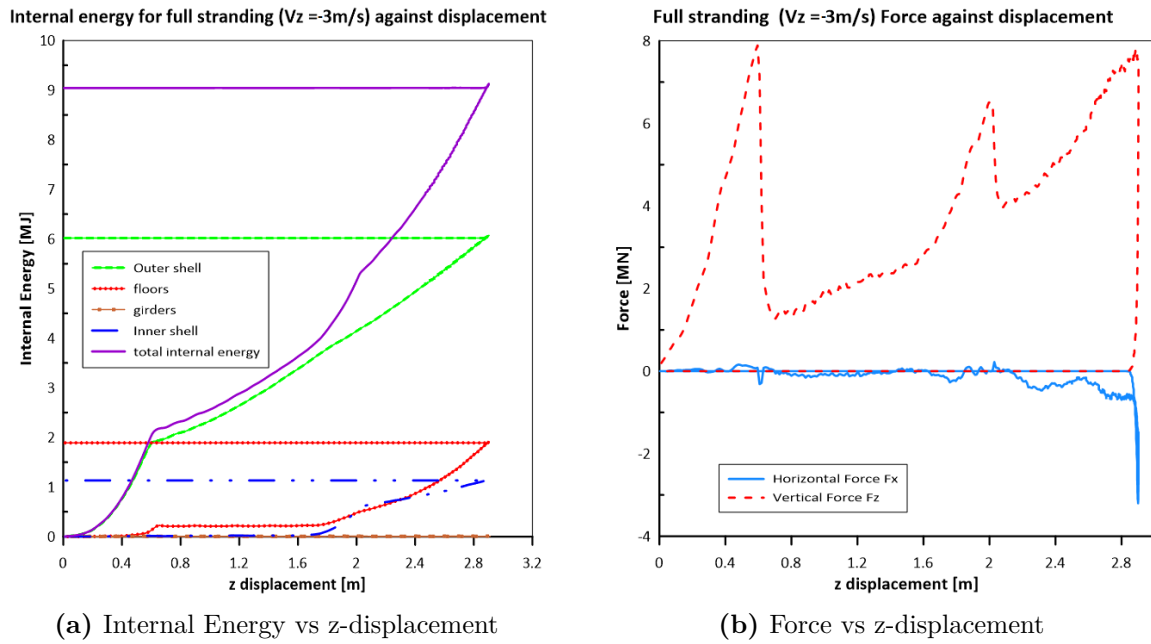


**Figure 57:** Internal Energy and force plots versus z displacement for full stranding (-3 m/s) grounding simulation

The major contributing structural members to the total internal energy were the outer shell plating, floors and inner shell as can also be seen in figure 57. The outer shell contributed about 67% of the total internal energy which was also due to the large area of the outer shell that was involved in the stranding event as compared to other structural members. The floors and the inner shell contributed about 21% and 13% respectively to the deformation energy.

The maximum penetration depth for this stranding event was about 2.9 metres, and at this point the initial kinetic energy of the ship was exhausted, and therefore the stranding ends. The force evolution of penetration is also represented in figure 57b and the maximum contact force was attained at about 0.7 metres penetration during the complete breaching of the outer shell.

### 3.5.2. Case 2: medium stranding on plate with $V_z = -1.5$ m/s

Similarly, in this case, the impact was on the outer shell plating in-between two transverse floors. The simulation time was 5 seconds and the stranding velocity was 1.5m/s downwards. The results for this stranding scenario are shown below.

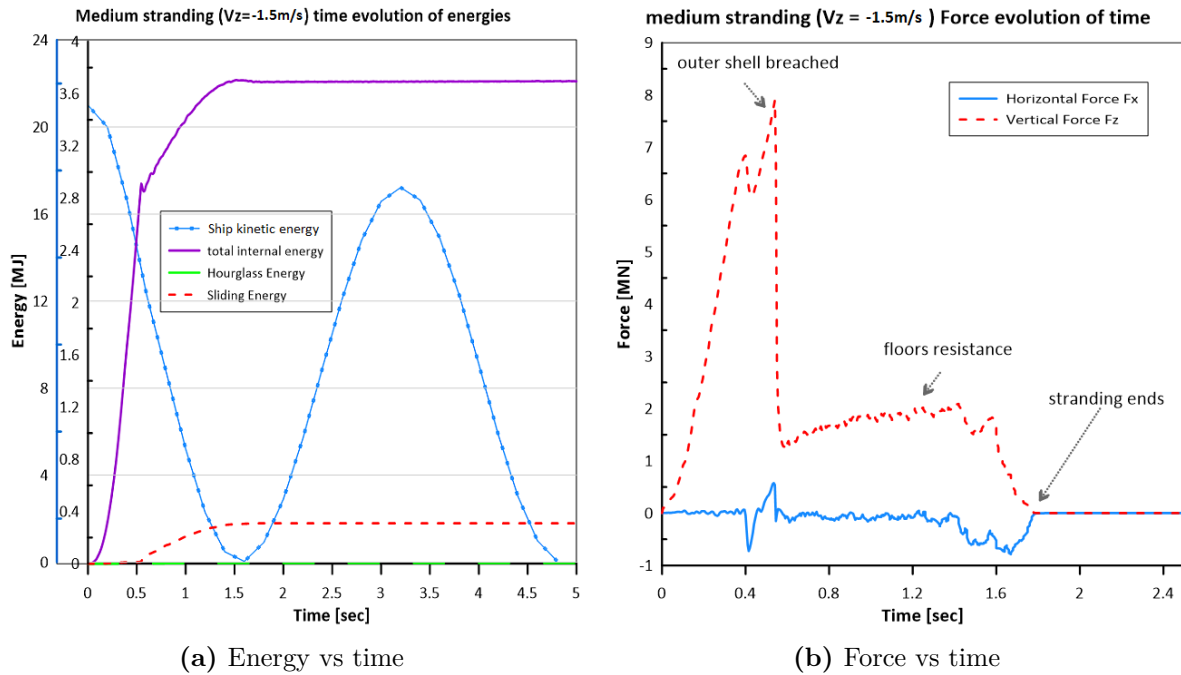


**Figure 58:** Energy and force plots versus time for medium stranding (-1.5 m/s) grounding simulation

Similarly, because of the differences in the magnitude of energies, the kinetic energy of the ship obtained from MCOL was plotted on a different y-axis coloured in blue, while other energies maintained the same y-axis which is in black.

The ship moved vertically downwards with an initial kinetic energy of about 21 MJ to impact the rock. As impact continued, the ship loses some of its kinetic energy to deformation energy. From figure 58a, at about 1.65 seconds into stranding, the ship exhausted almost all of its initial kinetic energy while the deformable parts of the ship attained a maximum internal energy of about 3.7 MJ. After this time period, the ship tends to regain its initial position as the force of buoyancy pushed it upward thereby giving the ship some additional kinetic energy as can be seen in the figure above.

The force-time plots also represented in the figure 58 above showed the distribution of the structural resistance to impact at a given point in time. The dominating forces as can be seen in the figure were still the vertical forces due to the vertical movement of the ship over the rock. The peak force of about 7.9 MN at 0.6 seconds was achieved during the complete crushing of the outer shell plating in the region of impact. Furthermore, due to the large area of the rock, the sides of the rock had contact with the floors, which further acted as resistance to penetration. The failure modes of the structural members are depicted in figure 59 below.

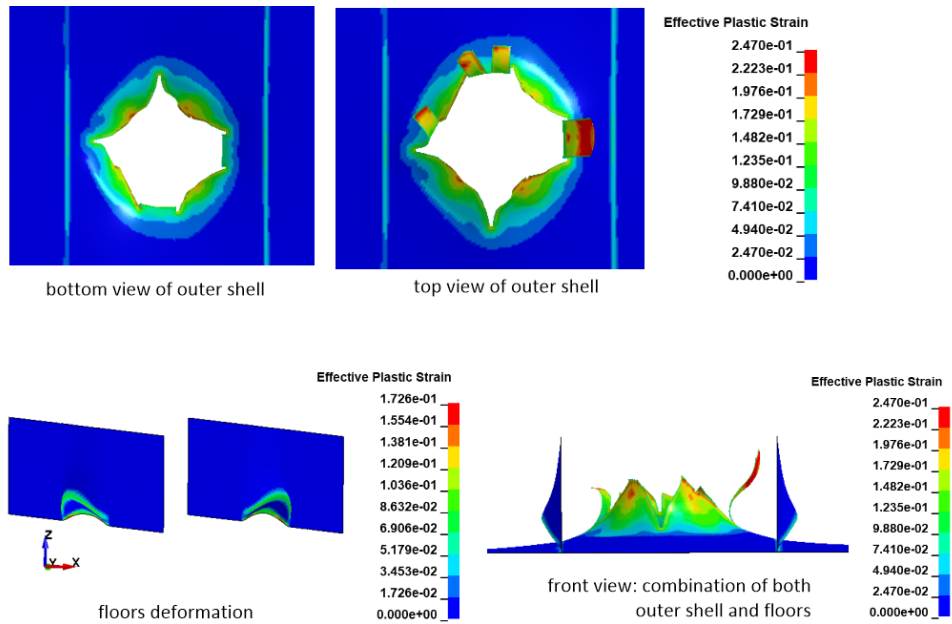


**Figure 59:** Deformation/Failure modes of structural members during medium stranding

From the figure above, due to the excessive compressive action of the outer shell on the rock, the plate experienced significant amounts of straining before fracture. The major failure mode of the bottom plate was tearing at various propagation points which was also resulting from the nature of the rock. The two transverse floors at close proximity to the point of impact experienced denting/folding and bending as can be seen on the second row of figure 59.

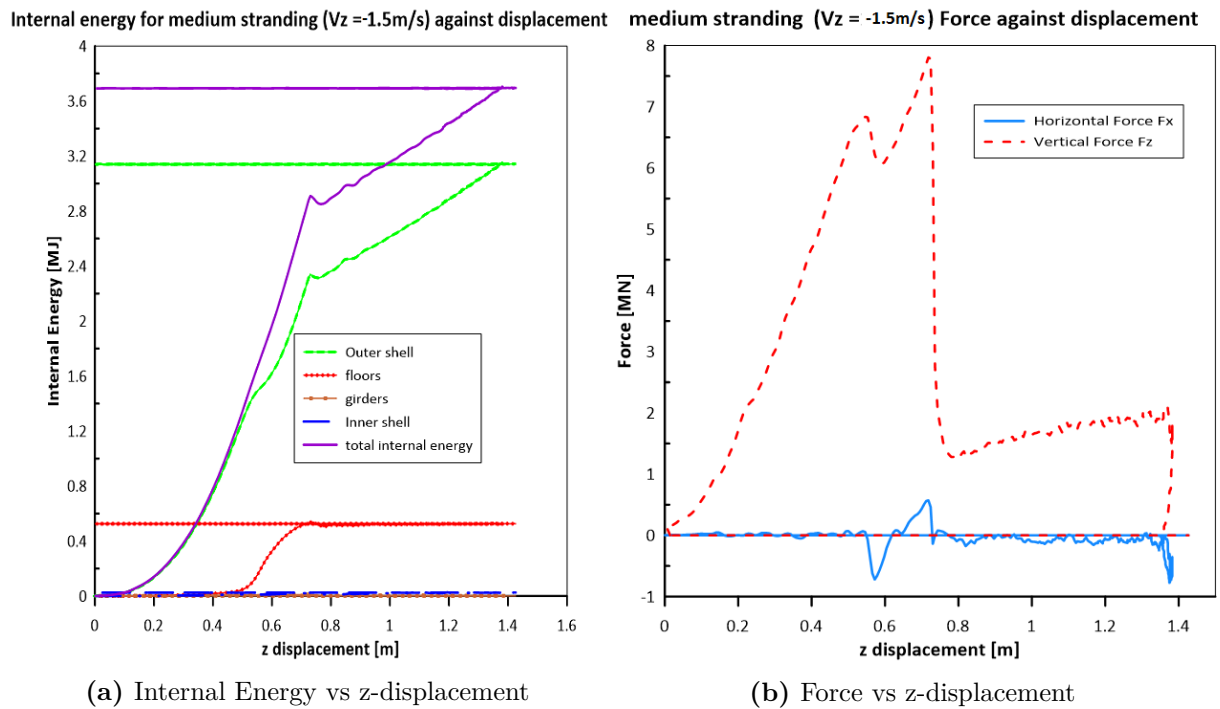


**Figure 60:** Internal Energy and force plots versus z-displacement for medium stranding grounding simulation

The contributions of various structural members to the total internal energy of this medium stranding scenario are shown in figure 60a. From the plot, the outer shell contributed about 85% of this internal energy. This means that almost all the deformation energy was obtained from the breaching of the outer shell. The least contributors were the girders and inner shell because there were no direct impact on them. Furthermore, the maximum penetration in this stranding event was about 1.3 metres with a breach length of about 3.5 metres.

### 3.5.3. Case 3: stranding on girder with $V_z = -2.0$ m/s

In this case, the targeted point of impact was the girder, therefore different mesh was generated. Fine mesh was imposed around the longitudinal region of possible impact and gradually increased while making sure that there was good mesh quality. The simulation time for this simulation was 3 seconds and the imposed initial vertical velocity was -2 m/s. The obtained results for stranding on girder scenario are shown below.

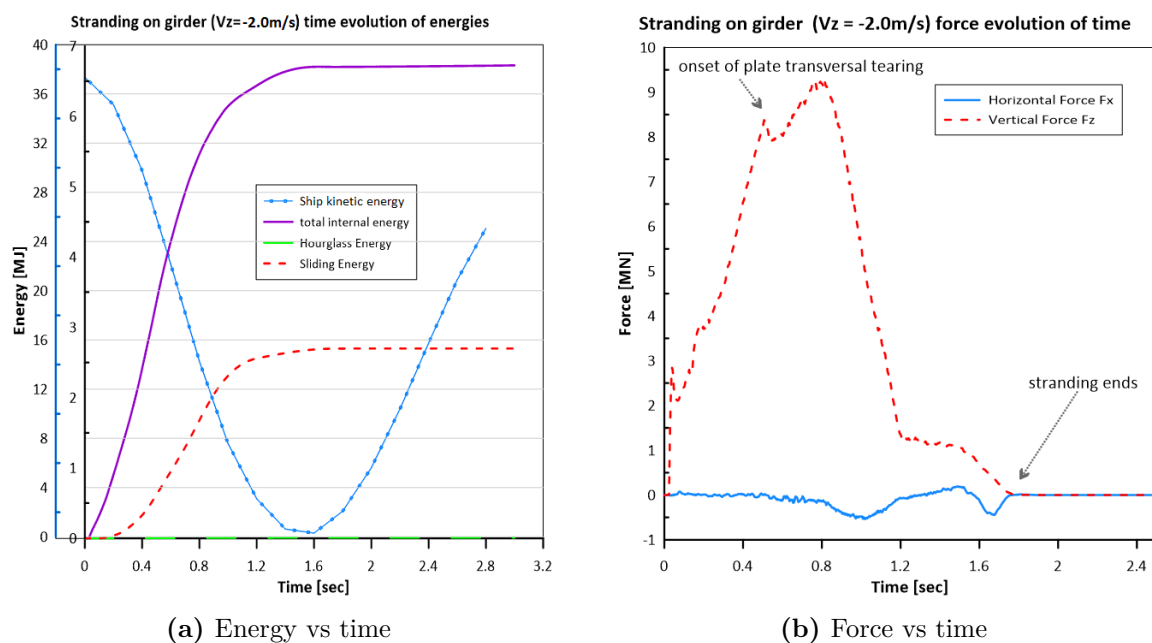


**Figure 61:** Energy and force plots vs. time for stranding on girder ( $V_z = -2$  m/s) simulation

In terms of time evolution of energies, the maximum total internal energy attained was about 6.7 MJ at about 1.62 seconds when the initial kinetic energy of the ship is almost exhausted, at this point the stranding event stopped and the ship gradually regains upward momentum due to the action of the restoring force of buoyancy. A maximum sliding energy of about 2.7 MJ was obtained due to the contact between the rock, the outer plating and the girder.

A maximum peak structural vertical resistance of 9.23 MN was attained at about 0.91 seconds during the stranding event. The deformation and failure modes of the structural members are shown below.

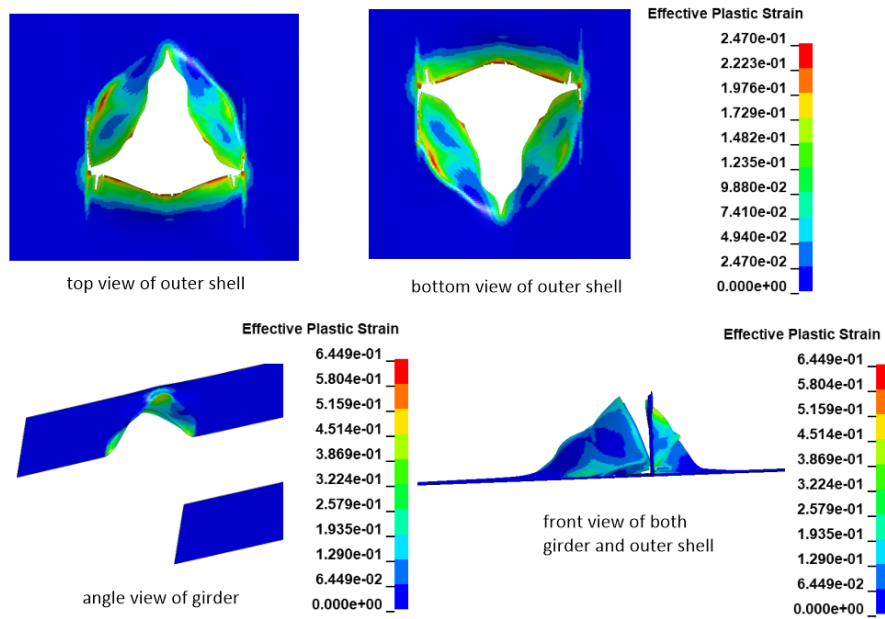


**Figure 62:** Deformation/Failure modes of structural members during stranding on girder

From the figure 62 above, the tearing of the outer shell is presented on the first row. It can be observed that the tearing pattern was due to the presence of the girder which gave the longitudinal tear along the bottom of the girder at the intersection between the girder and the outer shell. Furthermore, from the front view figure, we can observe a form of rolling effect that occurred due to the hydrodynamic effect, position of impact and the presence of only the girder on top of the rock, as a consequence, there was a sliding which led to the evolution of the second transverse tearing as can be seen in the figure.

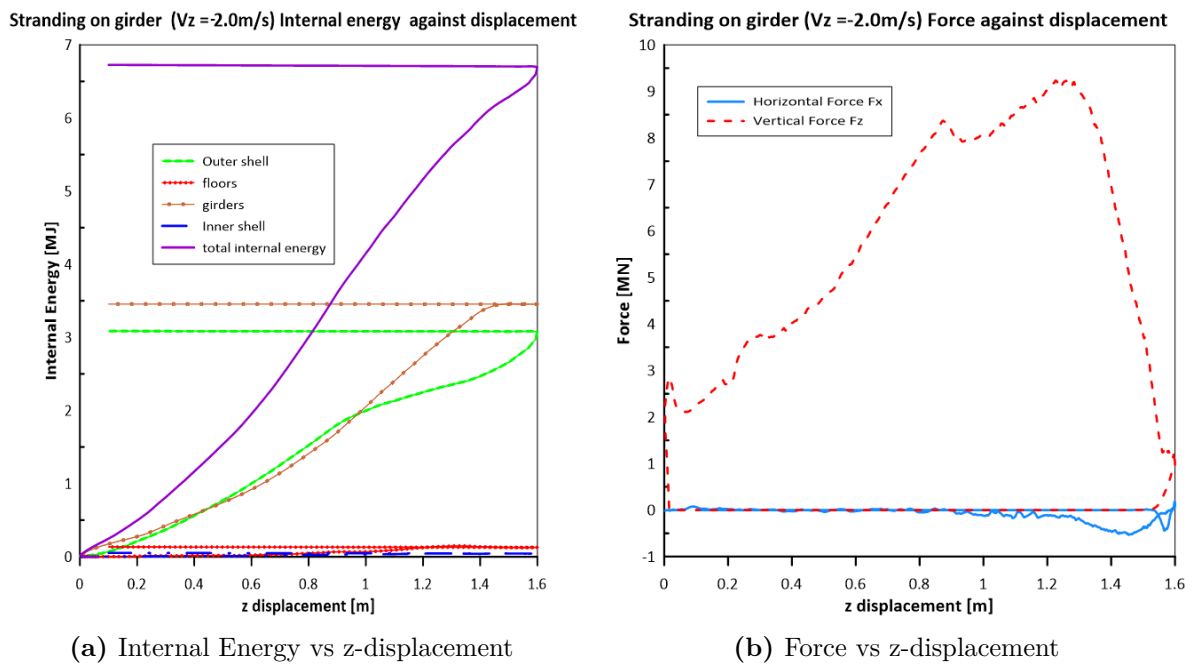


**Figure 63:** Internal Energy and force plots versus z-displacement for stranding on girder simulation

Additionally, the girder major deformation mode was denting and folding due to excessive compression and also due to our assumption that the girder is strong enough to resist and will not fail as can be seen in figure 62.

It is evident that the major contributors to the total internal energy were the girder and the outer shell with 51% and 46% contributions respectively as shown in figure 63. The inner shell and the floors had the least contribution as there were no direct impact action on them. The maximum penetration depth for this stranding case was about 1.6 meters. The force displacement plot which area accounts for internal energy had a maximum structural resistance of 9.23 MN at about 1.3 metres

### 3.5.4. Case 4: stranding on floor-girder intersection with $V_z = -1.5$ m/s

This scenario targeted first impact on the intersection between a transverse floor and a longitudinal girder as illustrated in figure 54. Same model geometry of the double bottom for the previous girder impact was used for this simulation. The simulation time was 5 seconds and an initial prescribed vertical velocity was -1.5 m/s.

The results obtained for this case are illustrated below.

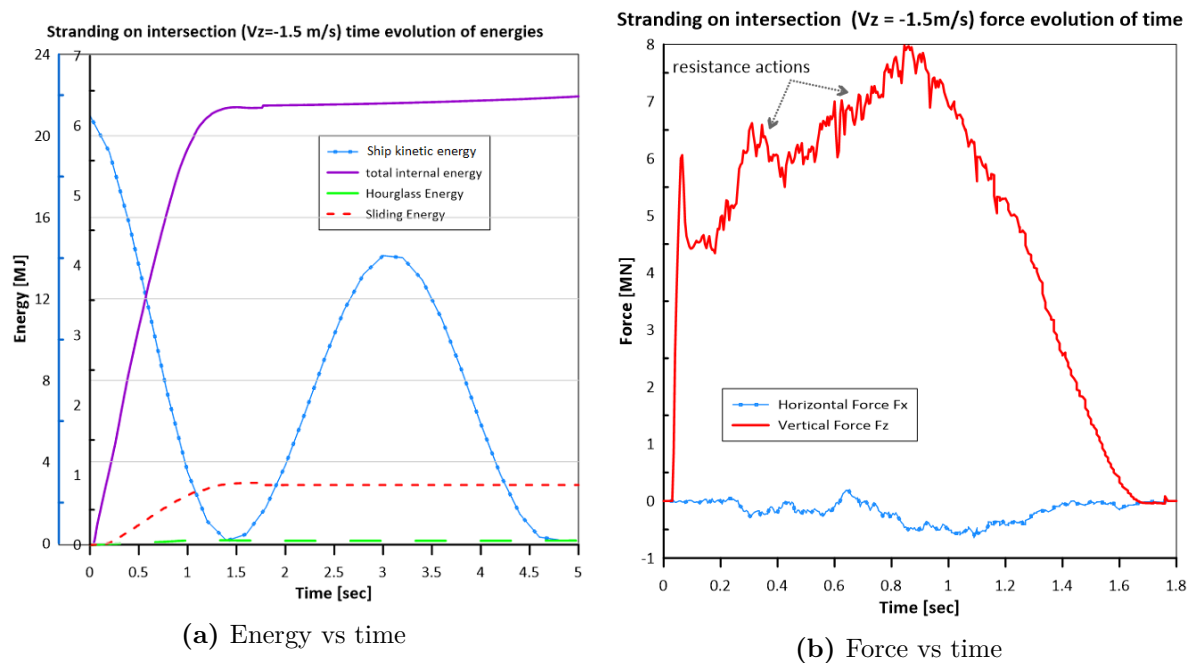


**Figure 64:** Energy and force plots versus time for stranding on girder ( $V_z = -1.5$  m/s) simulation

From the figure 64a, the initial kinetic energy obtained from MCOL was about 21 MJ of which was consumed during the stranding at about 1.5 seconds. Thereafter, there was a rebound which was due to the restoring force of buoyancy. The attained maximum total internal energy by the deformable parts of the ship was about 6.4 MJ.

There was build up of structural resistance as can be observed in figure 64b, this was due to the point of impact which is composed of several structural members. The maximum resistance of 7.98 MN was attained at 0.87 seconds and gradually as the ship loses its kinetic energy, the resistance plunged down.

The failure and deformation modes for this stranding case are depicted in figures below.

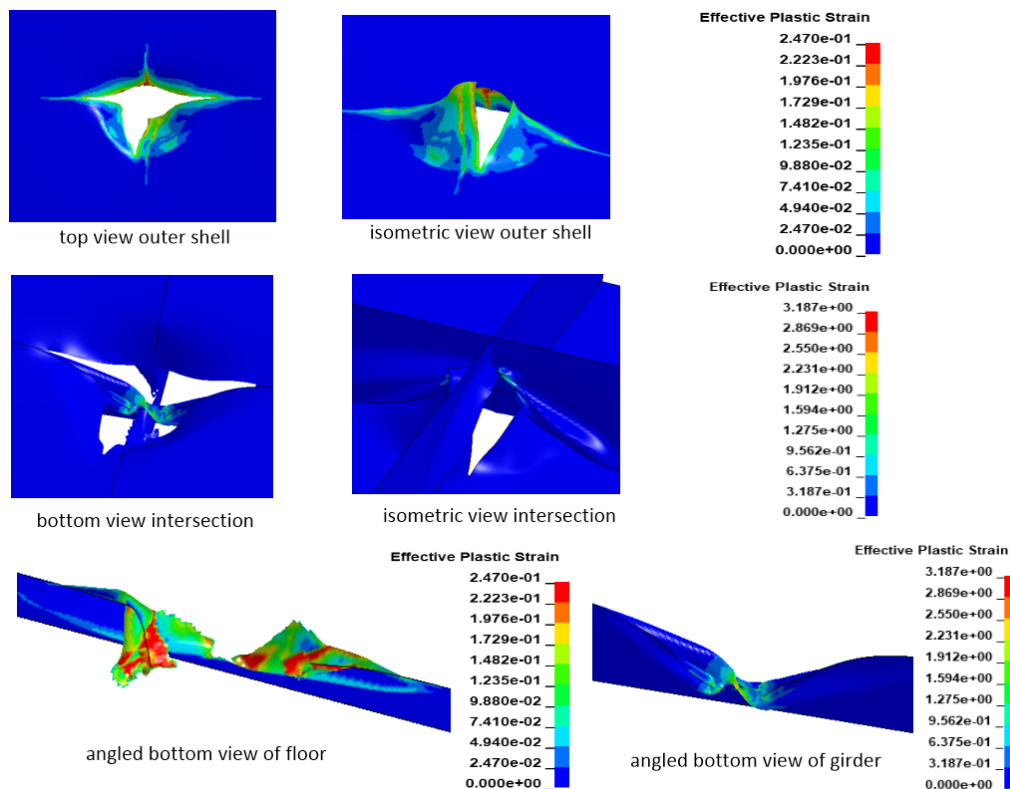


**Figure 65:** Deformation/Failure modes of structural members during intersection stranding

The affected members in this stranding event were the outer shell plating, the floor and the girder. From figure 65 we can observe the outer shell plating from the first row have undergone tearing along the paths of the girder and floor. This junction between the outer plating and the floor, and between the outer shell and the girder served as a propagation path for the plate tearing which was the dominating failure mode.

From the third row, the floor and the girder were illustrated. The floor failed by the crushing action of the rock due to excessive compression. The girder was assumed to be without failure, therefore it only experienced folding.

The second row from the figure illustrated the final position of the affected structural members after the stranding event.

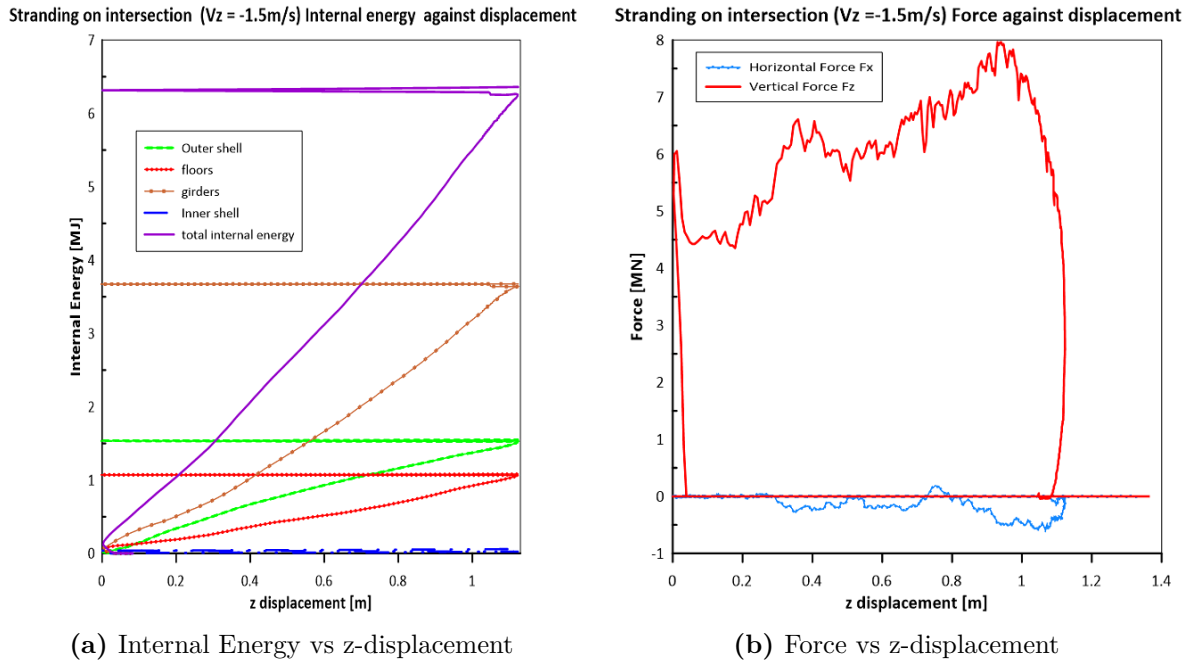


**Figure 66:** Internal Energy and force plots versus z-displacement for stranding on intersection simulation

The major contributors to the total internal energy were the girder with about 57% of the total internal energy, the outer shell, and the floor. The maximum penetration attained for this case was 1.12 metres and this was about the point the maximum structural resistance was attained.

A summary of the pure stranding grounding simulations are tabulated below:

**Table 13:** Pure stranding comparison

Stranding case:	full	medium	girder	intersection
Initial Ship K.E [MJ]	84.01	21	37.34	21
Max. Contact force Fz [MN]	7.92	7.9	9.23	7.98
Approx. Breach length [m]	5.28	3.5	3.3	5.2
Max. Penetration [m]	2.9	1.38	1.6	1.12

**Table 14:** Pure stranding Internal energy comparison

Raking case:	full		medium		girder		intersection	
Max. Energy [MJ]	9.13	%I.E	3.70	%I.E	6.73	%I.E	6.42	%I.E
Outer shell [MJ]	6.07	66.5	3.15	85.0	3.09	45.9	1.56	24.2
Floors [MJ]	1.90	20.9	0.54	14.6	0.15	2.19	1.10	17.2
Girders [MJ]	0.01	0.13	0.01	0.35	3.46	51.4	3.67	57.3
Inner shell [MJ]	1.15	12.6	0.03	0.73	0.05	0.78	0.08	1.3

From the tables above it can be observed that for the considered stranding cases, the outer shell plating contributed mostly to the deformation energy, and when the girder was involved in an impact, the girder contributed a lot in absorbing energy. Furthermore, the maximum breach length was observed by the full stranding case, and the maximum structural resistance was attained by the stranding on girder scenario as the girder was assumed to have no failure, this is also a contributing factor to the high structural resistance obtained.

### 3.6. Simulations Combining Raking and Stranding – Multiple Breaches Analyses

In this section we are considering a combination of both vertical and horizontal actions of the ship. This implies that the ship will be imposed with both surge and heave velocities. Normally, a ship via the action of waves acquires some heave motions, therefore it is important to consider this in grounding analyses.

For this subsection we are considering a horizontal velocity  $V_x$  of **1.5 m/s** and a vertical velocity  $V_z$  of **-0.75 m/s**. The two ships will be considered in this case; Floodstand and Ship\_1. Furthermore, the first impact of the rock was assumed to occur on the outer shell plating in-between two longitudinal girders.

For the Floodstand, because of the large mass leading to a high initial kinetic energy, the model was extended up to 72 metres to take into consideration the absorption of the whole kinetic energy and if possible the halt of the ship.

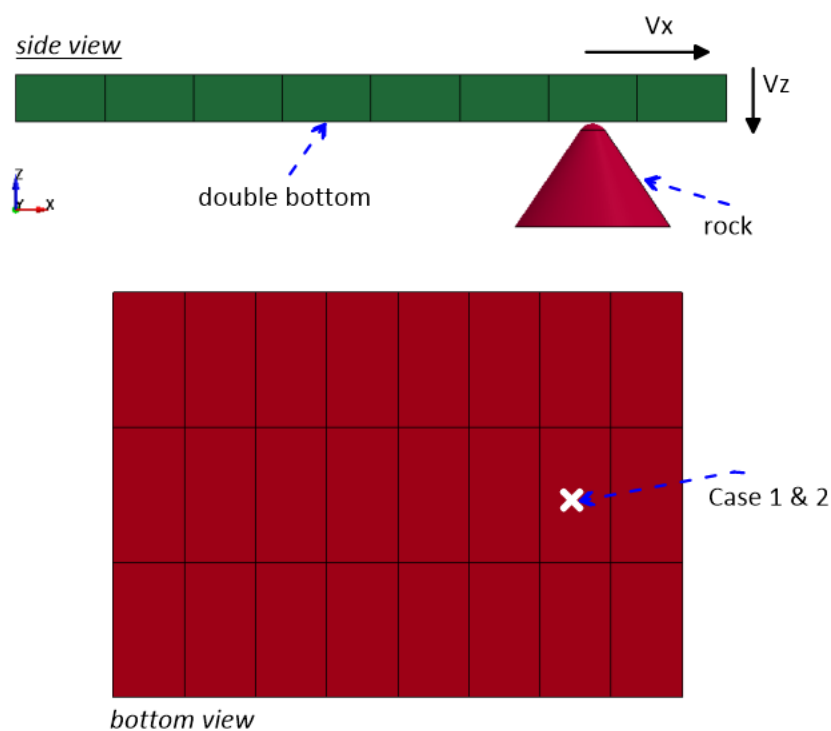


**Figure 67:** Set-up for multiple breaches simulation with impact points

### 3.6.1. Case 1: Ship\_1 multiple breaches simulation

The results for this grounding scenario with a simulation time of 25 seconds are given below. It is important to note that the length of the Ship\_1 model was still 24 metres because of the small mass of the ship. The two extreme floors in this case were taken as the rigid part of the ship to account for the remain ship parts.

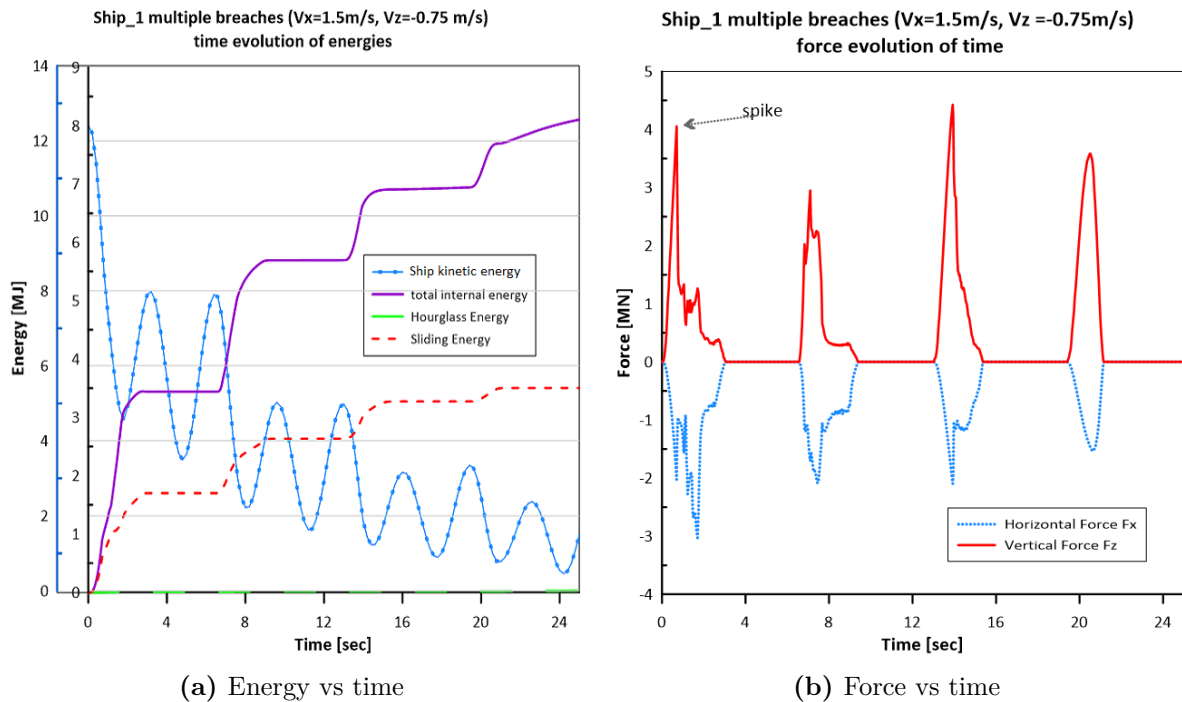


**Figure 68:** Energy and force plots versus time for Ship\_1 breaching simulation

From the figure 68a, the kinetic energy was plotted on a different y-axis coloured in blue for better representation. The wave-like distribution of the kinetic energy depicts the influence of the combination of the vertical velocity ( $V_z$ ), the horizontal velocity ( $V_x$ ) and also because of the external hydrodynamic forces. It is evident that because of the mass of the ship combined with the vertical velocity, the ship will move in the downward  $z$  direction. Also, because of the effects of the restoring force of buoyancy, the ship will be pushed upwards. Because of these continuous actions, the surrounding water, and the impact which occurred consecutively, the ship loses kinetic energy as it moves forward with the horizontal velocity which can be seen from the figure above.

Furthermore, the hourglass effect on the system can also be ignored as can be seen from the figure. The sliding energy was present due to contact at each breaching locations. In figure 68b the effects of the horizontal and vertical forces at each point in time was depicted. It is obvious that because of the combination of the horizontal and vertical velocities, both forces play vital role in the system. Although, the maximum contributing forces in this case was the vertical forces. The spikes shown in the figure for both the horizontal and vertical forces represent a kind of shock observed by the system at each

breach points with a maximum of about  $-3.0$  MN and  $4.4$  MN for horizontal and vertical forces respectively. Also, from figure 68b we can see that the duration for each impact decreases as the impact progresses, this is due to the loss of kinetic energy.

The deformation and failure modes of the structural members are shown below.

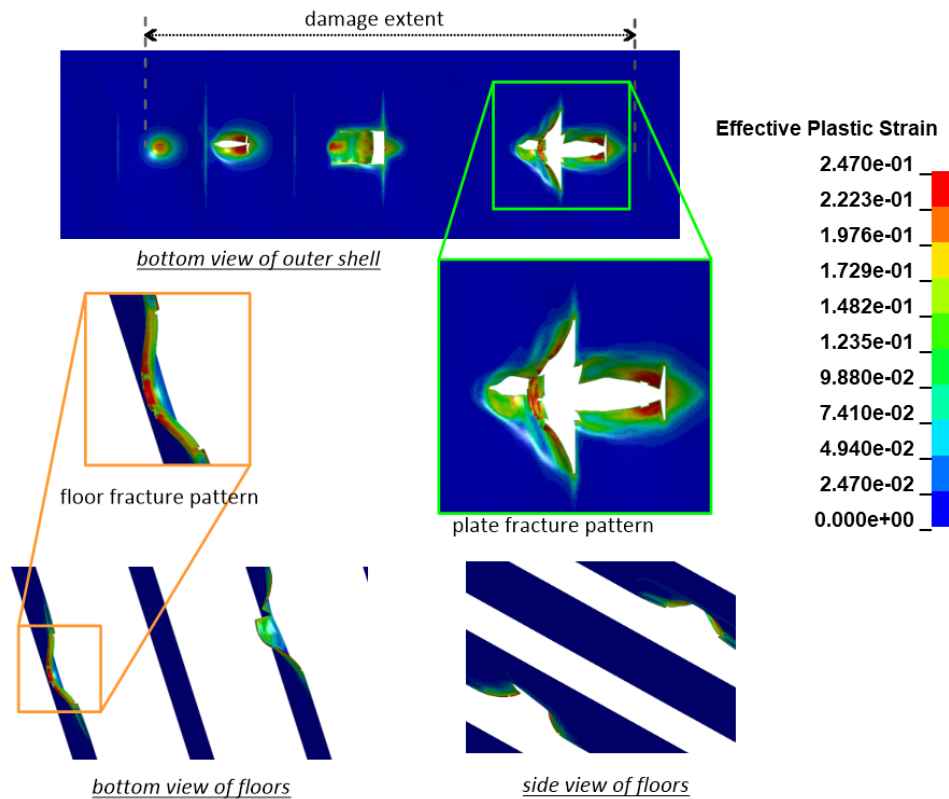


**Figure 69:** Deformation/failure modes for Ship\_1 multiple breaches simulation

From the figure 69 above, the multiple breaches are illustrated on the bottom view of the outer shell plating. It can be observed that there exist three complete multiple breaches and one denting on the outer shell. The last impact led to denting alone because of the loss in kinetic energy. It is also important to note that because of the termination time, the ship did not come to complete halt, therefore only four impacts were attained. Taking damage as a phenomenon which incurs loss of structural integrity, the damage extent was taken as the length of the multiple breaches event as shown in the figure above.

Since the impact affected only the outer shell plating and the floors, the figure highlighted these two structural members. The major failure mode for the outer shell was tearing along the direction of the motion. Also, tearing paths were contributed by the intersection between the floor and the outer shell plating. That is, if an impact occurred at an intersection between the outer shell and the floor, tearing would be propagated also along the transverse path of the floor as can be seen in the green zoomed image.

Only two floors were impacted in the breaching simulation and the major deformation and failure modes were folding, bending and tearing. The failure mode of the floors also

depends on the kinetic energy at the point of impact, as can be seen in the zoomed yellow image which was the last impact on the floor. The differences in failure modes between the last impact and the first one were evident that the first was major as a result of more kinetic energy of the ship which crushed the floor and led to evident tearing, while the second impact showed more of compression and bending because of the diminishing kinetic energy.

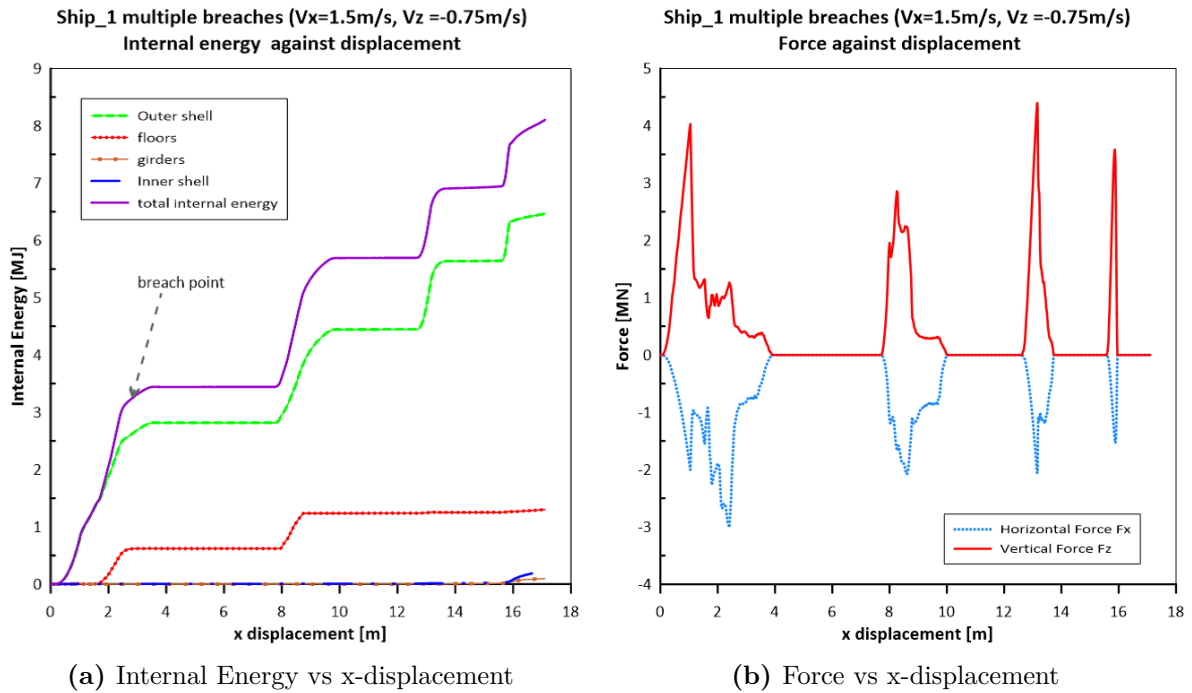


**Figure 70:** Internal Energy and force plots vs. x-displacement for Ship\_1 breaching simulation

The contribution of each structural member during the breaching event to the total energy absorption is shown on figure 70a. The arrow in the figure signifies the point of breach event. From the figure it can be observed that there were four points of breaching in the total internal energy and outer shell internal energy curves. For the floors there were just two breach points which signifies that only two impacts occurred on the floors. The total internal energy maintains a current energy value until another impact occurs then the deformation energy increases. The girders and the inner shell did not contribute a lot to the total internal energy because there were no direct impact on them.

The damage extent for this Ship\_1 multiple breaches simulation was about 16.39 metres which is approximately 67% of the length of the model. From figure 70b, the distance between consecutive breaches and the length of each breach tend to decrease as impact continued. It is evident also because of the loss of velocity which in turn leads to loss of kinetic energy.

### 3.6.2. Case 2: Floodstand multiple breaches simulation

The simulation time for this scenario was 65 seconds, and because of the large mass of the Floodstand vessel (and consequently the high initial K.E.), the model was extended up to 72 metres to take into account the gradual loss of the ship kinetic energy. Although, explicit analyses are normally investigated at shorter time period, this simulation of more than a minute showed good behaviour despite the gradual accumulation of numerical deviation errors with time. For this case, the two extreme girders were taken as the rigid part of the ship to account for the remaining ship parts. The results for this scenario are given below.

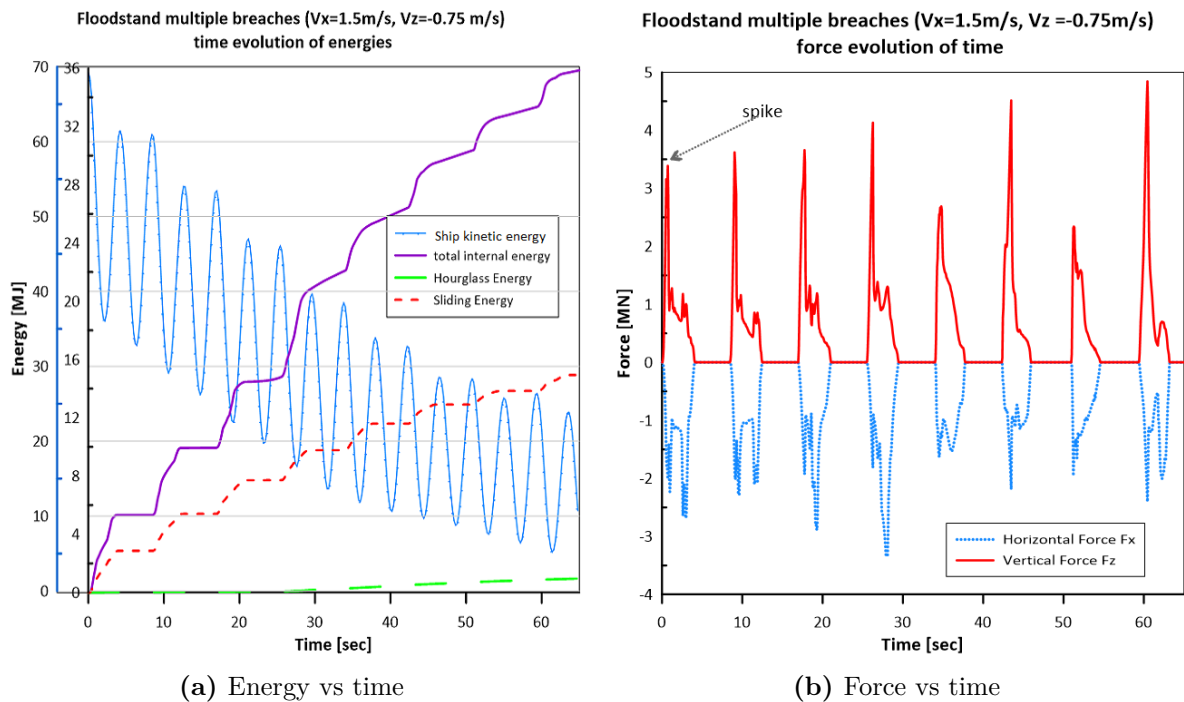


**Figure 71:** Energy and force plots versus time for Floodstand breaching simulation

This case was investigated to account for the influence of ship displacement to damage. As already mentioned, the mass of the Floodstand vessel is very high when compared to the Ship\_1. Similarly, the kinetic energy obtained from MCOL was plotted on a separate y-axis coloured in blue and other energies maintained same y-axis in black. As can be observed from the figure 71a, the ship did not come to stop after several breaches, but the reduction in the kinetic energy with time was obvious.

During the simulation at about 31 seconds, gradual numerical errors started accumulating and were visible on the post-processor as strains. These strains were found at the surrounding locations of impact along the ship. This can also be a consequence for the hourglass energy to start increasing gradually at about 30 seconds as can be seen on the plots. Although this hourglass energy did not affect the results because its peak value was way less than 5% of the maximum total internal energy, but it is advisable to keep the

simulation time reasonable low when numerical simulations using explicit time integration solver are performed. The sliding energy is as a result of contact at the points of breaching between the rock and the ship structural members.

The time evolution of the contact force is presented in figure 71b. The role played by both the vertical and the horizontal contact forces were evident as at each impact, there was a rise in structural resistance to penetration with a maximum of  $-3.3$  MN and  $4.8$  MN for horizontal and vertical forces respectively. Furthermore, it can be observed that the duration of impact and the time for next impact was almost uniform, this is also a consequence of the large mass of the vessel.

The failure modes for this scenario are shown in the figure below:

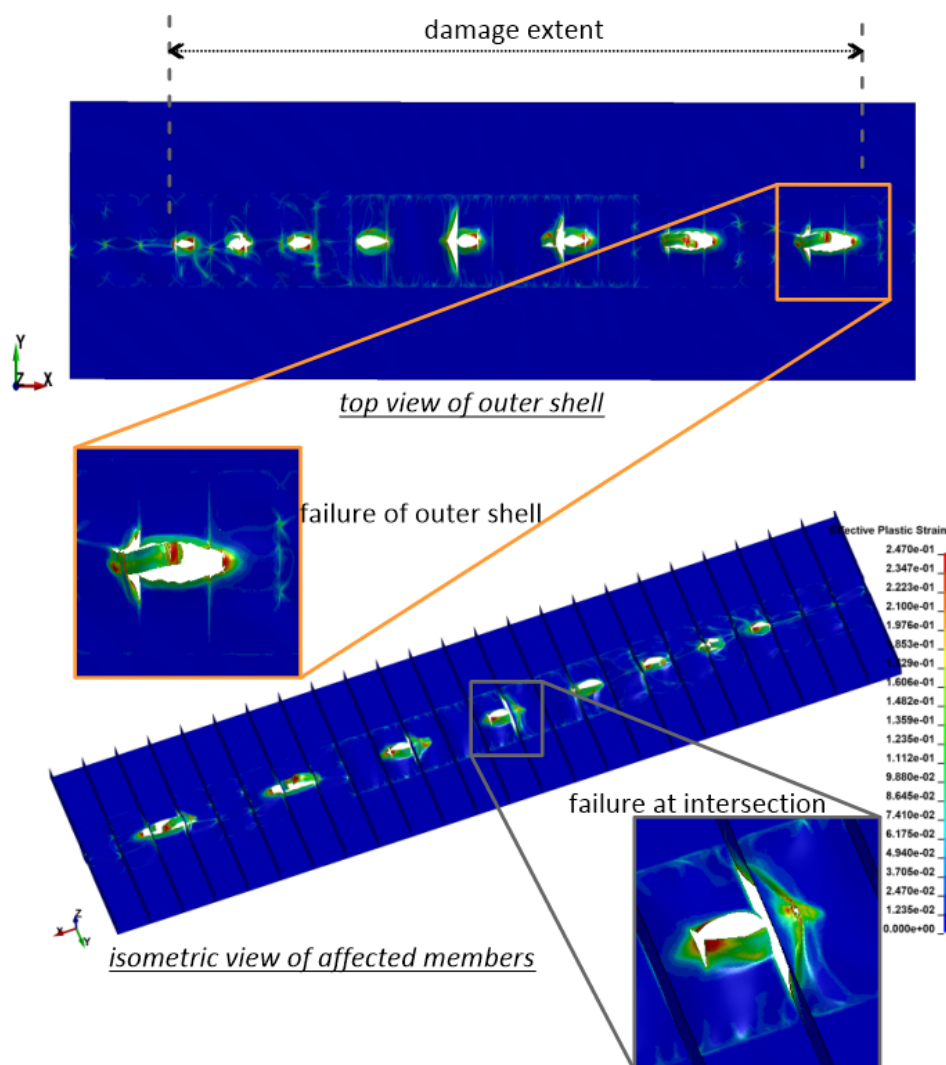


**Figure 72:** Deformation/failure modes for Floodstand multiple breaches simulation

The damage extent observed by this scenario was about 59.3 metres which is about 82% of the entire model. This also shows that with this considered velocities, it is possible to have multiple breaches at different compartments of a vessel which becomes more dangerous

than having just one or two compartments flooded due to the consideration of a continuous breach as a result of pure raking.

The major failure modes of the outer shell plating for this scenario followed the previous Ship\_1 pattern as it can be seen clearly from the zoomed orange portion of the outer shell. Tearing was dominating as a result of the crushing effect of the shape of the rock. Furthermore, as explained earlier, the point of intersection between the floors and the outer shell gives rise to propagation of fracture as can be visualised in the zoomed grey section in the same figure 72. The floors were basically crushed through horizontally by the rock in the case of horizontal action (raking stage), and was folded, bent, dented or torn due to excessive compression in the case of direct contact during the stranding stage.

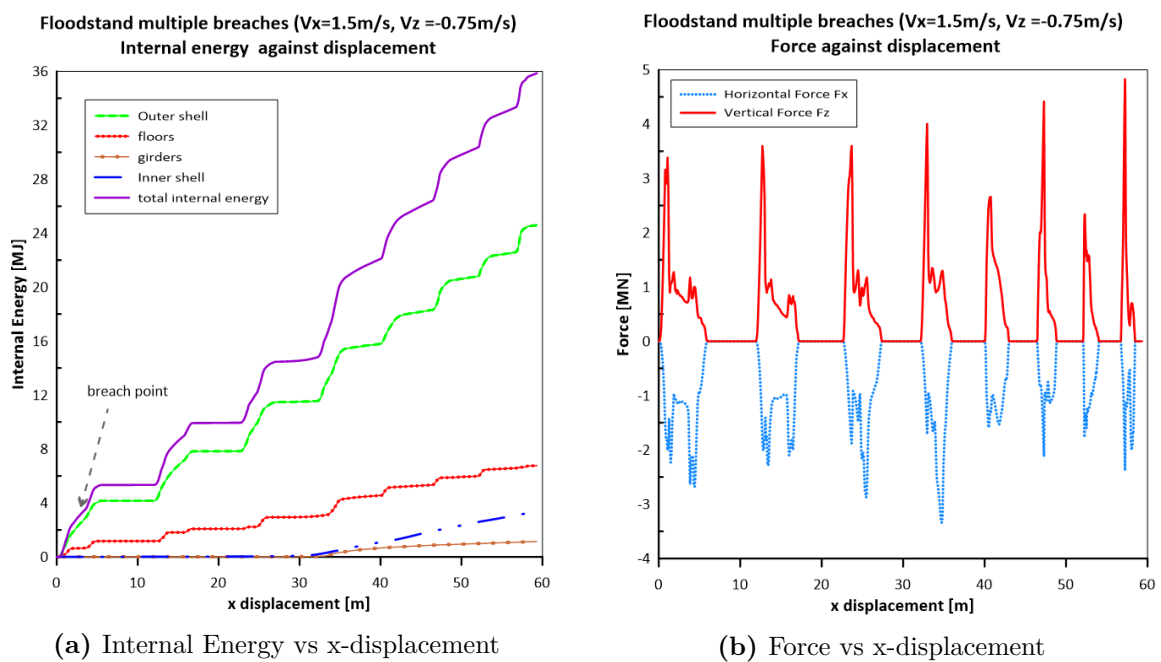


**Figure 73:** Internal Energy and force plots for Floodstand breaching simulation

The major contributor to the total internal energy was the outer shell which contributed about 69% of the total internal energy. The breach point as shown in figure 73a denotes the impact point, this implies that there were eight successive breaches. Furthermore, the floors had about seven breach points which means that seven floors were breached during this scenario. As explained earlier, because of numerical instabilities after about 30 seconds, the girder and the inner shell also started showing strain localisation at some regions of the model. This can be the reason for the gradual uptrend of the internal energy for the girders and the inner shell plating as can be seen in the figure above.

Furthermore, the spikes on the force displacement plots (figure 73b) denote the points of complete breach at each impact. Also, because of the reduction in the kinetic energy over time, the extent of a breach and the distance between successive breaches gradually reduces as impact progresses.

### 3.6.3. Damage comparisons

In this section, the importance of taking into consideration the external hydrodynamic forces together with considering the influence of the heave velocity on damage will be highlighted.

Recall that most researchers normally take into consideration either the pure stranding or pure raking scenario without considering the combination of both which is physical because, normally in sea, ships are exposed to waves which in turn yield to the heave motions of the ship. Also, most literature assumed a ship as fixed in a position and therefore letting the rock ram through the double bottom without considering the effects of external hydrodynamic forces on damage.

In this damage comparison study, the pure raking simulation for both Ship\_1 and Floodstand will be compared with the multiple breaches simulation with the same horizontal velocity. The analyses will be based on damage only.

Another simulation was ran for the Floodstand in pure raking scenario with a surge velocity of 1.5 m/s. For the Ship\_1 since simulations of pure raking with 2 m/s, 3 m/s and 4 m/s were already available, the damage extent was obtained by extrapolation.

The table below shows the comparison for this damage study using both ships with pure raking ( $V_x = 1.5$  m/s) and multiple breaches ( $V_x = 1.5$  m/s,  $V_z = -0.75$  m/s).

**Table 15:** Damage Comparison between pure raking and multiple breaches simulation

Simulation case:	Ship_1			Floodstand		
	raking	mult.	desc.(%)	raking	mult.	desc.(%)
Damage Extent [m]	<4	16.39	309.75	15	59.3	295.33
Max.Damage width [m]	5.7	3.78	33.68	5.75	4.68	18.61

From table 15, **mult** represents multiple breaches, and **desc.** represents percentage discrepancy. The importance of considering the vertical velocity of the ship together with the horizontal velocity. It can be observed that for pure raking simulation, the damage although continuous, led to smaller damage extents as compared with the multiple breaches scenario which combines the vertical velocity with the horizontal one. The damage extent was about four times larger. Although, for the pure raking scenarios the maximum damage width seemed larger, this was also due to the nature of impact, but this does not change the situation of water ingress into the compartments in the events of grounding.

This becomes very critical as several compartments can become flooded and can lead to total ship loss, loss of lives and properties and even environmental disaster in the case of tankers.

### 3.7. Parametric Sensitivity Analyses

#### 3.7.1. Damage sensitivity analysis to pitch movements

The bottom grounded section is now considered to be located at the fore part of the ship to check the corresponding influence of pitch motions to the damage extent in the case of breaching. In course of this pitch sensitivity analysis, the focus will be on the small ship; Ship\_1.

The axial location of the considered bottom section is changed by just shifting the axial position of the ship centre of gravity with respect to it.

A comparison will be made between a breaching where the double bottom model is located at the fore part of the ship and another breaching where the double bottom model is located just below the centre of gravity of the ship. The location of first impact will be on an intersection between a longitudinal girder and a transverse floor.

For this analysis, a study was carried out by Bureau Veritas using the Hydrostar software to estimate the order of magnitude of the vertical velocity of such kind of ship. It was concluded that for swells of periods of around 8 seconds, the heaving and pitching contributions are roughly equivalent and of the order of 2 m/s, and for weaker periods the speed component linked to heaving can become quite significant. This analysis allowed to give us the order of magnitude of the heave velocity of a ship at a particular cruising speed and wave height of about 4 metres.

A horizontal velocity of 7 m/s and vertical velocity of -1.5 m/s was used for this study. The length of the model was extended up to 72 metres to account for multiple breaches, and the two extreme girders were assigned to the rigid part of the ship to account for the remaining parts of the ship.

#### **fore-ship grounding**

With the double bottom model at the fore part of the ship, only two breaches occurred for this model length because of the prescribed velocity of 7 m/s (14 knots approximately). The role played by the pitch movement of the ship is evident in the second breaching. Since the ship pitched forward, the impact of the second breach was not as severe as that of the first breach as can be seen in figure 74.

The first breach with a length of about 21 metres was dominated by crushing and tearing of the outer shell plating and the transverse floors. The longitudinal girder was assumed not to fail therefore, it experienced folding due to excessive compression. The second breach with a length of about 12 metres experienced more of sliding and denting for the first 4 metres before tearing the structural members at impact points. Also, the breaching terminated with a second sliding and denting for another 4 metres after the tearing event.

---

This was due to the effects of the external hydrodynamic forces which aided the pitching movement of the ship.

The distance between the two breaches was about 30 metres. The total damage length is taken as the sum of the first breach length and the second breach length which amounted to about 33 metres. This implies that for a cruising speed with this vessel of about 15 knots and a model extent of 72 metres, 46% of the length of the ships double bottom will be damaged when exposed to grounding if pitching were to be present.

### mid-ship grounding

With the double bottom model just below the centre of gravity of the ship. It was observed that the breach size and the damage pattern was different when compared with the former case as there exist full crushing of the structural members during impact with the rock.

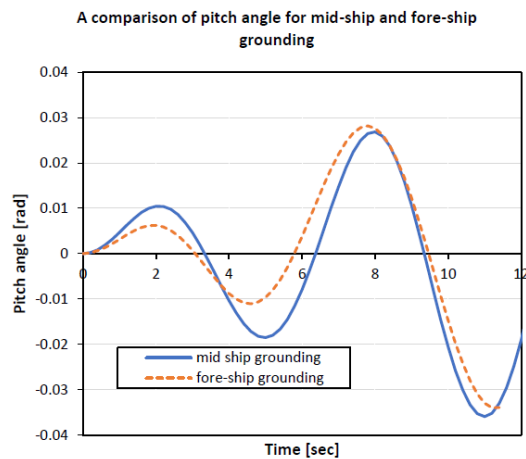
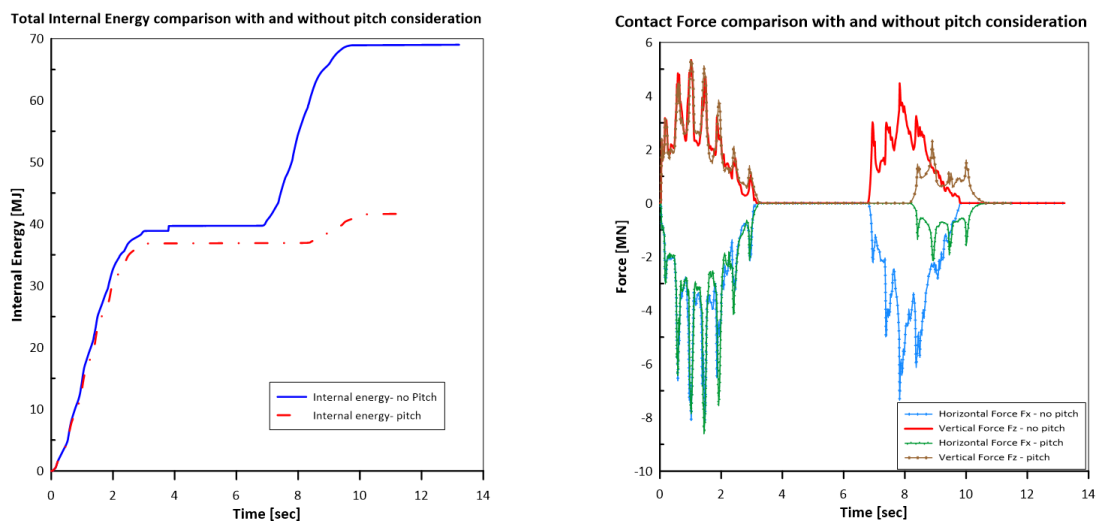


**Figure 74:** Comparison of pitch angles vs. time for fore-ship and mid-ship grounding



(a) Internal energy evolution with time

(b) Force evolution with time

**Figure 75:** Internal Energy and force plots for sensitivity of pitch consideration to damage

A comparison between the internal energy and the force over time for the cases of fore-ship grounding and mid-ship grounding are shown in figure 75.

It can be observed that the energy absorption capacity varied as can be seen in figure 75a. In the case of mid-ship grounding, the amount of structural members that were crushed were more, thereby increasing the internal energy. In the case when pitch was considered in the model set-up, the internal energy at first breach was almost in the same magnitude as the former case, but due to the pitch motions of the ship via the influence of the external hydrodynamic forces, the second breach was less severe as the ship pitched forward. This is also depicted in the force-time plot in figure 75b.

In this figure, the contact forces in both cases for the first breach were alike, but as the event continued, the second breach was different due to the influence of pitch motions. The case of fore-ship grounding had lower resistance in both the vertical and horizontal directions for the second breach due to less contact with the structural members at this point in time.

Comparing the damage sensitivity, the table 16 below summarises the damage extent obtained for both cases; fore-ship and mid-ship grounding.

**Table 16:** Damage comparison between fore-ship and mid-ship grounding: multiple breaches simulation

Simulation consideration:	fore-ship	mid-ship	discrepancy(%)
1 <sup>st</sup> breach length [m]	20.78	20.56	1.07
2 <sup>nd</sup> breach length [m]	12.35	16.19	23.72
breach separation [m]	30	21.88	37.11
damage length [m]	33.13	36.75	9.85
max. breach width [m]	2.64	4.55	41.98

In conclusion, we can observe the influence of pitch motions to the damage extent during grounding. In this pitch sensitivity analyses, we have considered the Ship\_1 and extended the model up to 72 metres to show that it is possible to have more than one breach during a grounding event. We have also considered a realistic surge and heave velocities of 7 m/s and -1.5 m/s respectively to also show the contribution of velocities and the external hydrodynamic forces to damage.

From table 16, we can observe that when the ship grounds under its centre of gravity, the resulting pitch movement is almost inexistent and there is more damage to the ship double bottom with about 50% of the considered double bottom length damaged during the grounding event. Furthermore, due to the contribution of the external hydrodynamic forces to pitch motions, the case when pitch movement is significant experiences less damage as the ship pitched forward giving rise to less structural impact with the rock.

### 3.7.2. Damage sensitivity to roll movements

In order to check for damage sensitivity to asymmetric points of impact, a multiple breaching simulation was carried out using the Ship\_1. The first impact was on a longitudinal girder as shown below. The simulation time was 25 seconds and the imposed velocities of the ship were  $V_x = 1.5$  m/s and  $V_z = -1.5$  m/s.

In this case, to account for the rigid part of the ship, the two extreme transverse floors were selected as rigid parts.

The final damage of the model is illustrated below.

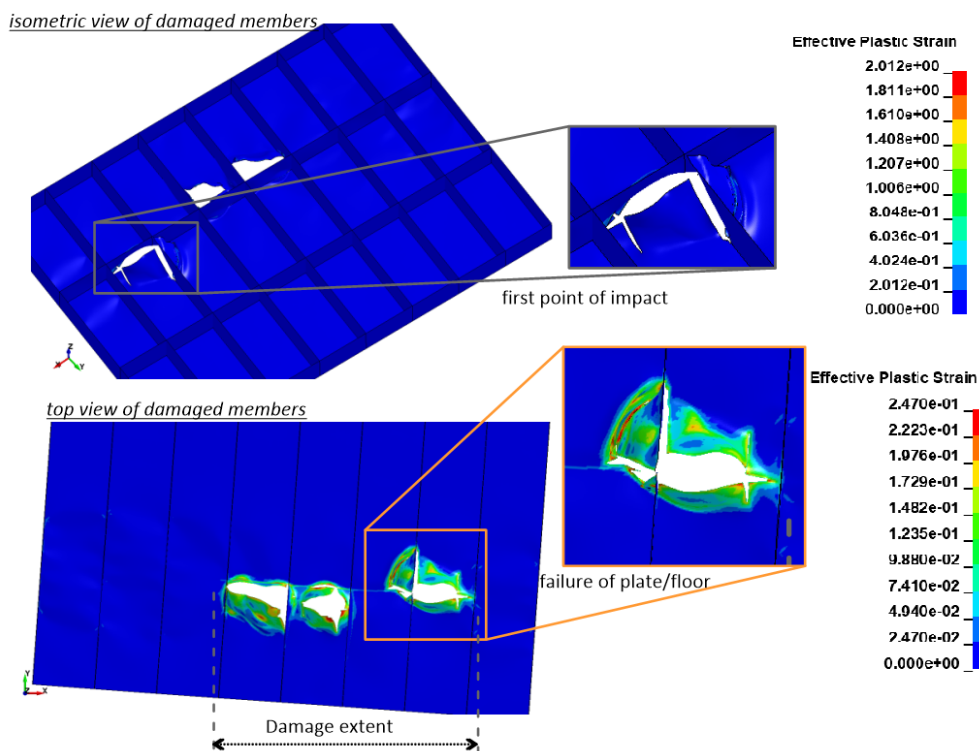


**Figure 76:** Failure of structural members during multiple breaching - roll sensitivity

From the figure 76, we can see the effect of the rolling movement of the ship to damage as compared to figure 69 where the first impact point was not asymmetric (in-between two longitudinal girders). This was also demonstrated in the roll angle versus time comparison plots in figure 77. It can be observed that accompanied by the external hydrodynamic forces, during the first impact, the ship rolled to the starboard side thereby enabling the next impact to occur on the outer shell plating. This can also be an additional consequence of the no-fail girder in resisting penetration.

Furthermore, due to the restoring force of buoyancy to balance the ship, the next impact was on the outer shell plating. The major failure mode of outer shell plating and the floor was tearing as can be seen in the figure 76.

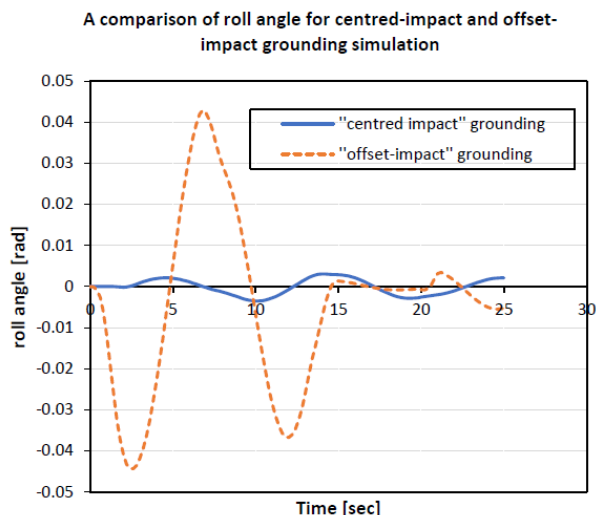


**Figure 77:** Comparison of roll angles vs. time for “centred-impact” and “offset-impact” grounding

A comparison of the damage extent between “offset impact” scenario and the previous Ship\_1 “centred impact” scenario which occurred in-between two longitudinal girders are shown in table 17.

**Table 17:** Damage Comparison between “centred impact” and “offset impact” multiple breaches simulation for Ship\_1

Simulation case:	“centred impact”	“offset impact”	discrepancy(%)
Damage Extent [m]	16.39	12.10	26.17
Max. Damage width [m]	3.78	3.38	10.58

From the table above, it can be observed that without roll motions of the ship, the damage extent and maximum width of damage at each breach point was higher than the case with roll motions. This can also be visualised in figure 69. Also, the distance between successive breaches is higher in the case without roll influence than with roll consideration. This was due to the external hydrodynamic force which tries to balance the ship at consecutive rolling phases.

## 4. CONCLUSION

In this chapter, several ship grounding scenarios have been scrutinised using two passenger ships; Ship\_1 (around 6000 tons) and Floodstand (around 34000 tons). The influence of the prescribed velocities, the displacement of the ship, the location of impact, and the external hydrodynamic forces on the damage extent during grounding incident have been investigated.

In order to obtain some numerical results to serve as reference for the validation of FLARE super-element solver, the pure raking and pure stranding scenarios which considered only surge and heave velocities of the ship respectively were explored. It was ascertained that the higher the speed of the ship, the more the damage extent. The structural resistance to crushing and the deformation energy were also studied, and in the considered cases, it was observed that the outer shell plating contributed to a great extent to the energy absorption capacity of the double bottom.

Multiple breaches scenarios were also explored in order to demonstrate the significance of considering the external hydrodynamic forces and the combination of both the ships horizontal and vertical velocities in ship grounding analyses. It was evident that the damage extend is much more important when several breaches occur than in continuous breach scenario. This becomes of pivotal importance during quantitative risk analysis to account for chances of evacuating passengers before total ship loss, because more compartments are liable to get flooded during multiple breaching situation.

The sensitivity of damage extent to pitch and roll motions were further investigated, and it was demonstrated that the total damage length lessened when pitch and roll movements are triggered by the grounding event. This additionally indicated the importance of considering the external hydrodynamic forces calculated by the MCOL program.

Overall, it is beyond doubt that for accurate numerical modelling and result attainment in dynamic impact analyses, several yardsticks must be adequately considered. These include but not limited to good modelling practice, good contact modelling and the right failure criteria to employ. In this grounding study, care was taken to ensure that these standards were adhered to. With regards to the failure criteria utilised in this study, the Peschmann and Lehmann criteria was implemented. However, it has been perceived that a little variation in this effective plastic strain value say  $\pm 5\%$  led to different failure modes of the double bottom, but this criteria was enacted because it had been demonstrated to yield good results during impact studies.

Lastly, with these results from various grounding scenarios, a validation basis will be provided for the FLARE solver which will be a complementary tool used at the pre-design stage to perform risk analyses in order to define the most damaging scenarios before carrying out FEA.

## 5. FURTHER WORK(S)

Possible future developments on this current study include but no limited to;

- The probe into the influence of different shapes and kinds of rock on damage. This can further be extended to exploring the ship structural behaviour to denting and sliding actions on the rock.
  - Several locations of impact can further be investigated as well as different realistic cruising velocities for the purpose of estimating the effects on breach size generation. With this, a rational prediction can be made to quantify the number of breaches expected in a particular model length or entire ship length.
  - Damage modelling can still be thoroughly perused in order to develop a better failure criteria to be inserted into the material card.
  - More sensitivity analyses can still be explored such as other degrees of freedom. Moreover, in terms of contact modelling, the values of the static and dynamic friction coefficients can still be rigorously analysed.
  - Finally, the results from these grounding scenarios will need cross-checking while providing a validation basis for the FLARE solver in order to check for discrepancies.
-

## 6. ACKNOWLEDGEMENTS

I would love to express my appreciation to professor Hervé Le Sourne, of ICAM. I could not ask for any better supervisor, it was a great honour to be under his supervision. His guidance, knowledge, kindness and experience is something worth commending. I have learnt a lot during this short period of time under his supervision. I am also grateful to Geneviève BAINES of ICAM who assisted me in various aspects to have a calm stay during my thesis.

Furthermore, I appreciate Jean-Philippe, Icaro, and Yeye, Ph.D. students at ICAM who were always ready to assist me in whatever problems I confronted during the course of my work and had the patience to help me with solving them.

Secondly, I can not forget to thank enough the coordinators of this prestigious EMSHIP program and all professors who have been part of this academic track. Specially, my gratitude goes to professor Rigo, Christine Reynders, Professor Kaeding and Thomas Lindemann, I thank you all for your selfless assistance in helping me directly or indirectly in achieving my current academic pursuit.

A very special appreciation goes to all my course mates. You guys are awesome and I honestly express my admiration for you all. You have become my family and I thank you all for being there for me. I wish us all the best in life and in the future ahead.

I also want to thank my dear friends who have been there for me when I run to them for help. You all hold a special place in my heart.

I am also very grateful to my family and relatives for believing and me, giving me the fire to push through. You have shown me what selfless love is all about, and if I begin to write long epistles about you all, this page will not be enough. To my father, you are a fighter and I admire you. To my late mother, you were an angel and I adore you. To my sisters, you all are rare gems and I cherish you all. To my brothers, you all are warriors and I respect you all.

The last but not the least, my profound gratitude goes to God almighty, the giver of life who has kept me, my friends and family alive to witness this great success. Without Him none of this would be possible.

Umunnakwe Chisom Bernard

---

## Dedication

I would dedicate this report to my dearly beloved mother - Late Mrs. Angela Umunnakwe. I can see your charming smile in every joy and happiness I feel. I have never been stronger as you have been my greatest source of motivation. You are the sun that shines at day, the moon that brightens our night sky, the star that shines at night. I wish you were here to experience my happiness. Forever you still remain in our hearts.

---

## References

- [1] LIVERMORE SOFTWARE TECHNOLOGY CORPORATION (LSTC). *LS-DYNA KEYWORD USER'S MANUAL VOLUME II Material Models*. 2018.
  - [2] A. AbuBakar and R.S. Dow. "Simulation of ship grounding damage using the finite element method". In: *International Journal of Solid Structures* 50 (2013), pp. 623–636.
  - [3] Allianz. *Safety and Shipping Review 2019 - An annual review of trends and developments in shipping losses and safety*. 2019. URL: <https://www.agcs.allianz.com/news-and-insights/reports/shipping-safety.html> (visited on 06/20/2020).
  - [4] H.S. Alsos and J. Amdahl. "On the resistance of tanker bottom structures during stranding". In: *Journal of Marine Structures* 20 (2007), pp. 218–237.
  - [5] J. Amdahl and D. Kavlie. "Experimental and numerical simulation of double hull stranding". In: (1992).
  - [6] M.J. Barba. "Mémoires de la Société des Ingénieurs Civils. Memoirs of the Society of Civil Engineers". In: 1 (1880), p. 682.
  - [7] Sun Bin, Hu Zhiqiang, Wang Jin, and Yu Zhaolong. "An analytical method to assess the damage and predict the residual strength of a ship in a shoal grounding accident scenario". In: *Journal of Ocean Engineering and Science* 1 (2016), pp. 167–179.
  - [8] J.D. Bressan and J.A. Williams. "The use of a shear instability criterion to predict local necking in sheet metal deformation." In: *International Journal of Mech. Sci* 25 (1983), pp. 155–168.
  - [9] Lars Brubak, Zhiqiang Hu, Mihkel Kõrgesaar, Ingrid Schipperen, and Kristjan Tabri. "Numerical Simulations of Grounding Scenarios – Benchmark study on key parameters in FEM modellings". In: (2019).
  - [10] Paik JK, Park JH, Samuelides E. "Collision accidental limit states performance of double hull oil tanker structures: Pre-CSR versus CSR designs." In: *Journal of Marine Technology* 46 (2009), pp. 183–191.
  - [11] Sören Ehlers., Joep Broekhuijsen., and et al. "Simulating the collision response of ship side structures: A failure criteria benchmark study". In: *International Shipbuilding Progress* 1 (2008), pp. 127–144.
  - [12] European Maritime Safety Agency EMSA. *Annual Overview of Marine Casualties and Incidents 2018*. 2018. URL: <http://www.emsa.europa.eu/emsa-documents/latest/item/3406-annual-overview-of-marine-casualties-and-incidents-2018.html> (visited on 06/20/2020).
-

- 
- [13] Cowper GR and Symonds PS. *Strain-hardening and strain-rate effects in the impact loading of cantilever beams*. Tech. rep. Technical Report No. 28, Division of Applied Mathematics, Brown University, Providence, RI, USA., 1957.
- [14] Le Sourne H., Couty N., Besnier F., Kammerer C., and Legavre H. “LS-DYNA applications in shipbuilding”. In: *4th European LS-DYNA users conference*. 2003, pp. 1–16.
- [15] R. Hill. “On discontinuous plastic states, with special reference to localised necking in thin sheets”. In: *Journal of Mech. Phys. Solids* 1 (1952), pp. 19–30.
- [16] L. Hong and J. Amdahl. “Plastic mechanism analysis of the resistance of ship longitudinal girders in grounding and collision”. In: *Journal of Ships and Offshore Structures* DOI: 10.1080/17445300802263849 3 (2008), pp. 159–171.
- [17] Lin Hong and Jørgen Amdahl. “Rapid assessment of ship grounding over large contact surfaces”. In: *Ships and Offshore Structures* 7 (2012).
- [18] Paik JK, Kim SJ, Ko YG, and Youssef SAM. “Collision risk assessment of a VLCC class tanker”. In: *The SNAME Maritime Convention, Houston, 23-28 October*. 2017.
- [19] Liu K, Liu B, Guedes Soares C, and Wang Z. “Experimental and numerical analysis of a laterally impacted square steel plate.” In: *Proceedings of the International Conference on Maritime Technology and Engineering, Lisbon, Portugal, 4-6 July*. 2016.
- [20] Alan Klanac, Soren Ehlers, and Jasmin Jelovica. “Optimization of crashworthy marine structures”. In: *Journal of Marine Structures* (2009).
- [21] Yeong Gook Ko, Sang Jin Kim, Jung Min Sohn, and Jeom Kee Paik. “A practical method to determine the dynamic fracture strain for the nonlinear finite element analysis of structural crashworthiness in ship-ship collisions”. In: (2017).
- [22] H. Le Sourne. “Contribution à la modélisation de quelques problèmes de dynamique des structures et de couplages fluide structure. Mémoire d’Habilitation à diriger des Recherches. Université de Nantes, Ecole doctorale SPIGA”. In: (2015).
- [23] H. Le Sourne, N. Besnard, C. Cheylan, and N Buannic. “A ship collision analysis program based on upper bound solutions and coupled with a large rotational ship movement analysis tool”. In: *Journal of Applied Mathematics* (2012).
- [24] E. Lehmann and X. Yu. “On Ductile Rupture Criteria for Structural Tearing the Case of Ship Collision and Grounding.” In: *Practical Design of Ships and Mobile Units* (1998).
- [25] M.A.G.Calle. and M.Alves. “A review-analysis on material failure modelling in ship collision”. In: *Journal of Ocean Engineering* 106 (2015), pp. 20–38.
-

- 
- [26] M.A.G.Calle, R.E.Oshiro, and M.Alves. “Ship collision and grounding:Scaled experiments and numerical analysis”. In: *International Journal of Impact Engineering* 103 (2017), pp. 195–210.
- [27] A.E. Mansour and R.C. Ertekin. Tech. rep.
- [28] V.V. Minorsky. “An Analysis of Ship Collisions with Reference to Protection of Nuclear Power Plants”. In: *Journal of Ship Research* (1959).
- [29] Jones N. *Structural Impact*. Cambridge university press, 2012.
- [30] Tan-Hoi Nguyen, J. Amdahl, L. Garrè, and Bernt J. Leira. “A study on dynamic grounding of ships”. In: *Advances in marine structures* (2011).
- [31] Hughes OF and Paik JK. “Ship structural analysis and design”. In: *The Society of Naval Architectures and Marine Engineers, Alexandria, USA* (2013).
- [32] J. Peschmann and A. Kulzep. *Side collision of double skin ships*. Tech. rep. Final report for BMBF Life-cycle design.Technical University of Hamburg., 2000.
- [33] A. R. Prabowo, D. M. Bae, J. H. Cho, and J. M. Sohn. “Characteristic of double bottom responses under powered-hard grounding scenario with idealised rock indenter”. In: *International Journal of Structural Engineering* 9 (2018), p. 130.
- [34] Bruce W.T. Quinton. “ISSC2021 V.1 Accidental Limit States Committee Benchmark Study”. 2020.
- [35] Bruce W.T. Quinton, Claude G. Daley, Robert E. Gagnon, and D.Bruce Colbourne. “Guidelines for the nonlinear finite element analysis of hull response to moving loads on ships and offshore structures”. In: *Ships and Offshore Structures* (2016).
- [36] Copernicus Marine Service. “COSTA CONCORDIA ACCIDENT:MONITORING POTENTIAL OIL SPILLS”. In: (2013).
- [37] M. Servis D.P.and Samuelides. “Implementation of the T-failure criterion in finite element methodologies”. In: *Structures* 84 (2006), pp. 196–214.
- [38] International Ship and Offshore Structures Congress. 2018. URL: [http://www.issc2018.org/categories/cat\\_technical2](http://www.issc2018.org/categories/cat_technical2) (visited on 06/15/2020).
- [39] BC. Simonsen. “The Mechanics of Ship Grounding”. PhD thesis. Department of Naval Architecture and Offshore Engineering, Technical University of Denmark, Lyngby, 1997.
- [40] H. Le Sourne, E.R. Donner, F. Besnier, and M. Ferry. “External dynamics of ship-submarine collision”. In: *2nd International Conference on Collision and Grounding of Ships Copenhagen* (2001), pp. 137–144.
- [41] H.W Swift. “Plastic Instability under plane stress”. In: *Journal of Mech. Phys. Solids* 1 (1952), pp. 1–18.
-

- 
- [42] R Törnqvist. “Design of crashworthy ship structures”. PhD thesis. Technical University of Denmark, Lyngby, 2003, p. 243.
- [43] A. and Feenstra E. Vredeveldt. *Crashworthy side structures for improved collision damage survivability of coaster and medium sized Ro-Ro cargo ships*. Tech. rep. Report GRD1-1999-10566, TNO/UNI, 2001.
- [44] G Wang, H Ohtsubo, and D. Liu. “A simple method for predicting the grounding strength of ships”. In: (1997).
- [45] Jia Zeng, Zhiqiang Hu, and Gang Chen. “A steady-state plate tearing model for ship grounding over a cone-shaped rock”. In: *Journal of Ships and Offshore Structures* 11 (2016), pp. 245–257.
- [46] Shengming Zhang. “Plate tearing and bottom damage in ship grounding”. In: *Journal of marine structures* 15 (2001), pp. 101–117.
- [47] Hu Zhiqiang, Amdahl Jørgen, and Hong Lin. “Verification of a simplified analytical method for predictions of ship groundings over large contact surfaces by numerical simulations”. In: *Journal of marine structures* 24 (2011), pp. 436–458.
-

# Appendices

## A. Floodstand with $V_x=4\text{m/s}$ , $V_z=-1.0\text{ m/s}$

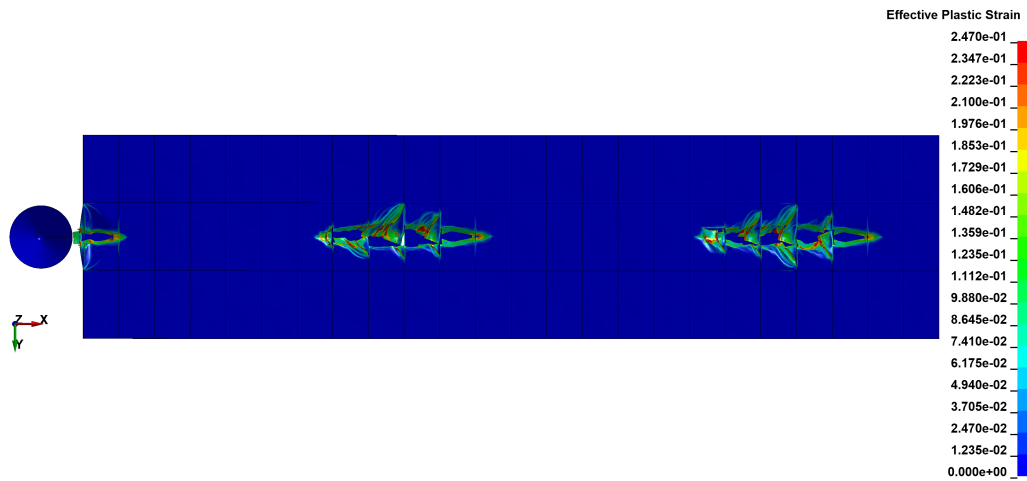
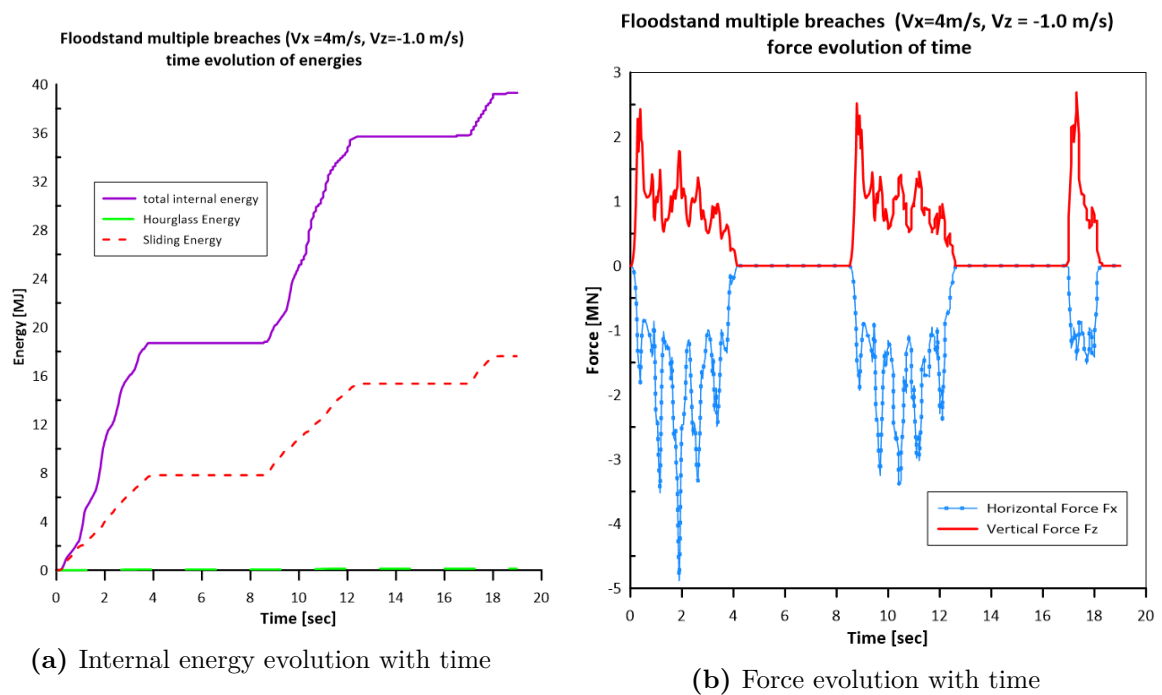


Figure 78: Distribution of breaches



(a) Internal energy evolution with time

(b) Force evolution with time

Figure 79: Internal Energy and force plots for Floodstand;  $V_x =4\text{m/s}$ ,  $V_z=-1.0\text{m/s}$